SCOUR AT THE REAR SIDE OF RUBBLE MOUND REVETMENTS

A THESIS SUBMITTED TO
THE GRADUATE SCHOOL OF NATURAL AND APPLIED SCIENCES
OF
MIDDLE EAST TECHNICAL UNIVERSITY

BY

MEHMET EMRE YILDIRIM

IN PARTIAL FULFILLMENT OF THE REQUIREMENTS
FOR
THE DEGREE OF MASTER OF SCIENCE
IN
CIVIL ENGINEERING

AUGUST 2021

Approval of the thesis:

SCOUR AT THE REAR SIDE OF RUBBLE MOUND REVETMENTS

submitted by **MEHMET EMRE YILDIRIM** in partial fulfillment of the requirements for the degree of **Master of Science** i**n Civil Engineering, Middle East Technical University** by,

Prof. Dr. Halil Kalıpçılar
Dean, Graduate School of **Natural and Applied Sciences** _____

Prof. Dr. Ahmet Türer
Head of the Department, **Civil Engineering** _____

Assist. Prof. Dr. Cüneyt Baykal
Supervisor, **Civil Engineering, METU** _____

Examining Committee Members:

Prof. Dr. Ahmet Cevdet Yalçıner
Civil Engineering, METU _____

Assist. Prof. Dr. Cüneyt Baykal
Civil Engineering, METU _____

Assoc. Prof. Dr. Mustafa Tuğrul Yılmaz
Civil Engineering, METU _____

Assoc. Prof. Dr. Kubilay Cihan
Civil Engineering, Kırıkkale Üniversitesi _____

Assist. Prof. Dr. Gülizar Özyurt Tarakcıoğlu
Civil Engineering, METU _____

Date: 17.08.2021

I hereby declare that all information in this document has been obtained and presented in accordance with academic rules and ethical conduct. I also declare that, as required by these rules and conduct, I have fully cited and referenced all material and results that are not original to this work.

Name Last name : Mehmet Emre Yıldırım

Signature :

ABSTRACT

SCOUR AT THE REAR SIDE OF RUBBLE MOUND REVETMENTS

Yıldırım, Mehmet Emre
Master of Science, Civil Engineering
Supervisor : Assist. Prof. Dr. Cüneyt Baykal

August 2021, 96 pages

In this study, an examination of the scour at the rear side of rubble mound revetments resulting from wave overtopping was performed. The effects of backfill materials, backfill height, and wave properties on the process were investigated through physical model experiments. One of the main findings of the study is that as the storm duration increases, the maximum scour depth eventually reaches an equilibrium state. Also, as the overtopping discharge increases, the scour depth occurs deeper. Estimation of geometrical features of the scour and accretion was acquired by taking overtopping discharge amount and backfill height as governing parameters. Normalized scour profiles were obtained and grouped into four. In addition, the mean normalized scour profile was presented. Prediction of time-related scour parameters, which are the time scale and the time needed to observe maximum scour depth, were presented. The time scale of the scour was found independent of overtopping discharge amount. It was seen that three different wave series with the same wave properties created different scour profiles due to different overtopping discharge amounts.

Keywords: Wave Overtopping, Rubble Mound Revetment, Scour

ÖZ

TAŞ DOLGU KIYI TAHKİMAT YAPILARININ GERİSİNDE OYULMA

Yıldırım, Mehmet Emre
Yüksek Lisans, İnşaat Mühendisliği
Tez Yöneticisi: Dr. Öğr. Üyesi Cüneyt Baykal

Ağustos 2021, 96 sayfa

Bu çalışmada taş dolgu kıyı tahkimat yapılarının arka tarafında dalga aşması kaynaklı gerçekleşen oyulmalar çalışılmıştır. Fiziksel model deneyleri gerçekleştirilerek, dolgu malzemesi, dolgu yüksekliği ve dalga özelliklerinin oyulma sürecine etkileri araştırılmıştır. Bu çalışmanın ana bulgularından biri, fırtına süresi arttıkça, maksimum oyulma derinliğinin belirli bir zamandan sonra denge durumuna ulaşmasıdır. Ayrıca, aşma debisinin artması, daha derin oyulma derinliği meydana getirmektedir. Aşma debisi miktarı ve dolgu yüksekliğine bağlı oyulma ve birikmenin geometrik özelliklerini veren ampirik denklemler verilmiştir. Boyutsuzlaştırılmış oyulma profilleri elde edilmiş ve dört ana gruba toplanmıştır. Buna ek olarak, ortalama boyutsuz oyulma profili sunulmuştur. Oyulmanın zamanla ilişkili parametreleri olan zaman ölçeği ve maksimum oyulma derinliğini gözlemlemek için gerekli olan süre aşma debisi ve dolgu yüksekliği ile ilişkilendirilerek sunulmuştur. Aynı dalga özelliklerine sahip üç farklı dalga serisinin farklı aşma miktarlarına sahip olmaları nedeniyle farklı oyulma profilleri oluşturduğu gözlemlenmiştir.

Anahtar Kelimeler: Dalga Aşması, Taş Dolgu Kıyı Tahkimatı, Oyulma

Dedicated to the ones true to their words

ACKNOWLEDGMENTS

First, I would like to express my appreciation to my supervisor Dr. Cüneyt Baykal. This study required a lot of hard works, and from the start, he committed to the study. Whenever I struggled with issues, he helped as fast as possible. I have learned a lot from his expertise.

I would like to thank Prof. Dr. Ayşen Ergin who is always giving positive energy to everyone. Her positivity always helped me to motivate. She created a coastal family, and I am happy to be part of this family.

I would like to express my appreciation to Prof. Dr. Ahmet Cevdet Yalçıner, Dr. Işıkhan Güler, Dr. Gülizar Özyurt Tarakçıoğlu, and Dr. Gökhan Güler for the education that I have learned form them.

I would like to express my appreciation to my brother Mert Yaman. What we shared in the wave flume while we were conducting the experiments was unique and indescribable. His commitment to this study was impressive. I am glad that we worked on this project together.

I would like to thank my friends Koray Göral and Kadir Karakaş for their help in learning how to use the tools in the flume. Also, I would like to thank my friends Arda Çiçek, Aslı Devran, Barış Ufuk Şentürk, Berkay Akyol, Can Özsoy, Cem Bingol, Ghazal Khodkar, Gözde Güney Doğan, İlker Çoban, Sedat Gözlet, and Utku Uzun for their sincere friendship.

I would like to thank my family for the support and respect that they showed to my decisions. Without them, life would be so complicated. I am so glad to have a family like this.

This work is funded by the Scientific and Technological Research Council of Turkey under grant number TUBİTAK 119M677.

I would like to thank Serhan Akin and Tencate Geosynthetics Altyapı Ürün ve Çözümleri Tic. Ltd. Şti for providing the geotextile fabric used in the experiments.

TABLE OF CONTENTS

ABSTRACT v

ÖZ vi

ACKNOWLEDGMENTS viii

TABLE OF CONTENTS x

LIST OF TABLES xii

LIST OF FIGURES xiii

LIST OF ABBREVIATIONS xvii

LIST OF SYMBOLS xviii

CHAPTERS

1 INTRODUCTION 1

2 LITERATURE REVIEW 5

2.1 Sluice Gate Studies 5

2.2 Spillway Studies 6

2.3 Coastal Dike Studies 8

2.4 Tsunami Overflow Studies 9

2.5 Weir Studies 11

3 METHODOLOGY 13

3.1 Dimensional Analysis 13

3.2 Scaling 16

3.3 Experimental Setup 17

3.4 Physical Model Experiments 22

3.4.1 Wave Calibration and Overtopping Tests 22

3.4.2 Scour Experiments 24
4 RESULTS 29
4.1 Overtopping Results 29
4.2 Scour Results 32
4.2.1 Evaluation of Scour Profiles 36
4.2.2 Multiple Regression Analysis 41
4.2.3 Time Scale 50
5 DISCUSSION 55
6 CONCLUSION 61
REFERENCES 63
APPENDICES
A. Scour Formations and Development Curves for Tests with $d50 = 0.21$ mm 69
B. Scour Formations and Development Curves for Tests with $d50 = 0.66$ mm 89
C. Scour Formations and Development Curves for Tests with $\mathrm{d}50 = 3.35$ mm 93
D. Regular Measurements and Scour Formations for S-Test-6 96

LIST OF TABLES

TABLES

Table 3.1. Features of the rubble mound revetment 17
Table 4.1. The results of the overtopping tests 30
Table 4.2. The results of the scour experiments 34
Table 4.3. Multiple regression results regarding the geometrical features 46
Table 4.4. Multiple regression results regarding the time related features 52

LIST OF FIGURES

FIGURES

Figure 2.1. Definitive Sketch for Sluice Gate Studies (adapted from Hassan and Narayanan (1985)) 6
Figure 2.2. Definitive sketch for spillway studies (adapted from Farhoudi and Smith (1995)) 7
Figure 2.3. Definitive sketch for coastal dike studies (adapted from Oumeraci et al. (2005)) 9
Figure 2.4. Definitive sketch for tsunami studies (adapted from Tsujimoto et al. (2014)) 11
Figure 2.5. Definitive sketch for weir studies (adapted from Guan et al. (2016)) .. 12
Figure 3.1. Scour rear side of a rubble mound revetment 13
Figure 3.2. Piston type wave generator 18
Figure 3.3. Drawing of the experimental setup (Unsclaed, dimensions are in meter) 19
Figure 3.4. Cross-section with a square hole perforated sheet 20
Figure 3.5. General view of the wave flume 21
Figure 3.6. Geotextile cover application before the cross-section placement 22
Figure 3.7. The group of wave gauges placed at the slope 23
Figure 3.8. The coastal revetment with the overtopping gutter 24
Figure 3.9. Experimental setup with the computer-controlled bottom profiler 25
Figure 3.10. The lazer lines measured to acquire rear side changes (not to scale) . 26
Figure 4.1. Comparison between the experimental data and EurOtop (2018) 31
Figure 4.2. Seaside view of the S-Test-6 32
Figure 4.3. Normalized scour profiles of GR1 36
Figure 4.4. Normalized Scour Profiles of GR2 37
Figure 4.5. Rear side movement due to the wave pressure 38
Figure 4.6. Normalized scour profiles of GR3 38
Figure 4.7. Normalized scour profiles of GR4 39

Figure 4.8. Seaside view of the S-Test-20 bed profile 40
Figure 4.9. Mean normalized scour profile 41
Figure 4.10. Relation between the maximum scour depth and the mean overtopping discharge in linear axes 42
Figure 4.11. Relation between the maximum scour depth and the mean overtopping discharge in logarithmic axes 42
Figure 4.12. Relation between the maximum scour depth and the backfill height in linear axes 43
Figure 4.13. Relation between the maximum scour depth and the backfill height in logarithmic axes 43
Figure 4.14. Relation between the maximum scour depth and the grain size distribution of the backfill material in linear axes 44
Figure 4.15. Relation between the maximum scour depth and the grain size distribution of the backfill material in logarithmic axes 44
Figure 4.16. Measured and predicted results of the maximum scour depth 47
Figure 4.17. Measured and predicted results of the maximum accretion height 48
Figure 4.18. Measured and predicted results of the maximum scour depth distances to the crown wall 48
Figure 4.19. Measured and predicted results of the maximum accretion height distances to the crown wall 49
Figure 4.20. Measured and predicted results of the scour hole width in wave direction 49
Figure 4.21. Measured and predicted results of the accretion width in wave direction 50
Figure 4.22. Scour development in time 51
Figure 4.23. Measured and predicted results of the time scale of the scour 53
Figure 4.24. Measured and predicted results of the time needed to observe maximum scour depth 54
Figure 0.1. Final morphological changes for S-Test-1 69
Figure 0.2. Scour development in time for S-Test-1 69

Figure 0.3. Final morphological changes for S-Test-2 70
Figure 0.4. Scour development in time for S-Test-2 70
Figure 0.5. Final morphological changes for S-Test-3 71
Figure 0.6. Scour development in time for S-Test-3 71
Figure 0.7. Final morphological changes for S-Test-4 72
Figure 0.8. Scour development in time for S-Test-4 72
Figure 0.9. Final morphological changes for S-Test-5 73
Figure 0.10. Scour development in time for S-Test-5 73
Figure 0.11. Final morphological changes for S-Test-6 74
Figure 0.12. Scour development in time for S-Test-6 74
Figure 0.13. Final morphological changes for S-Test-7 75
Figure 0.14. Scour development in time for S-Test-7 75
Figure 0.15. Final morphological changes for S-Test-8 76
Figure 0.16. Scour development in time for S-Test-8 76
Figure 0.17. Final morphological changes for S-Test-9 77
Figure 0.18. Scour development in time for S-Test-9 77
Figure 0.19. Final morphological changes for S-Test-10 78
Figure 0.20. Scour development in time for S-Test-10 78
Figure 0.21. Final morphological changes for S-Test-11 79
Figure 0.22. Scour development in time for S-Test-11 79
Figure 0.23. Final morphological changes for S-Test-12 80
Figure 0.24. Scour development in time for S-Test-12 80
Figure 0.25. Final morphological changes for S-Test-13 81
Figure 0.26. Scour development in time for S-Test-13 81
Figure 0.27. Final morphological changes for S-Test-14 82
Figure 0.28. Scour development in time for S-Test-14 82
Figure 0.29. Final morphological changes for S-Test-15 83
Figure 0.30. Scour development in time for S-Test-15 83
Figure 0.31. Final morphological changes for S-Test-16 84
Figure 0.32. Scour development in time for S-Test-16 84

Figure 0.33. Final morphological changes for S-Test-17 85
Figure 0.34. Scour development in time for S-Test-17 85
Figure 0.35. Final morphological changes for S-Test-18 86
Figure 0.36. Scour development in time for S-Test-18 86
Figure 0.37. Final morphological changes for S-Test-19 87
Figure 0.38. Scour development in time for S-Test-19 87
Figure 0.39. Final morphological changes for S-Test-20 88
Figure 0.40. Scour development in time for S-Test-20 88
Figure 0.41. Final morphological changes for S-Test-21 89
Figure 0.42. Scour development in time for S-Test-21 89
Figure 0.43. Final morphological changes for S-Test-22 90
Figure 0.44. Scour development in time for S-Test-22 90
Figure 0.45. Final morphological changes for S-Test-23 91
Figure 0.46. Scour development in time for S-Test-23 91
Figure 0.47. Final morphological changes for S-Test-24 92
Figure 0.48. Scour development in time for S-Test-24 92
Figure 0.49. Final morphological changes for S-Test-25 93
Figure 0.50. Scour development in time for S-Test-25 93
Figure 0.51. Final morphological changes for S-Test-26 94
Figure 0.52. Scour development in time for S-Test-26 94
Figure 0.53. Final morphological changes for S-Test-27 95
Figure 0.54. Scour development in time for S-Test-27 95
Figure 0.55. Regular measurements for S-Test-27 96
Figure 0.56. Final morphological changes with seven individual lines for S-Test-27 96

LIST OF ABBREVIATIONS

ABBREVIATIONS

DHI	Danish Hydraulic Institute
JONSWAP	Joint North Sea Wave Project
MAE	Mean Absolute Error
NMB	Normalized Mean Bias
RMSE	Root Mean Square Error
TMA	Texal-Marsen Arsloe

LIST OF SYMBOLS

SYMBOLS

A	Maximum accretion height
a_m	Average wave amplitude
c	Wave Celerity
d_{16}	The diameter that 16 percent of the backfill materials are finer
d_{50}	The median diameter of the backfill material
d_{84}	The diameter that 84 percent of the backfill materials are finer
D_*	Dimensionless grain size
D_{n50}	Median stone size diameter
Δ	The ratio of submerged backfill material weight and water weight
F_r	Froude number
F_*	Densimetric Froude number
g	Gravitational acceleration
G_c	Crest width
γ_f	Influence factor for the permeability and roughness of the slope
γ_β	Influence factor for oblique wave attack
h_c	Backfill height
H_{m0i}	Incident spectral significant wave height in front of the structure
h_0	The thickness of the water jet
h_{toe}	Water depth at the toe

L_A	Width of the accretion height in wave direction
L_S	Width of the scour hole in wave direction
l_s	Relative length
λ_L	Model length scale
λ_T	Model time scale
λ_q	The scale of the mean overtopping discharge per unit
λ_w	Model weight scale
m	Bed slope
n	Porosity
q_{mean}	Mean overtopping discharge per unit width
N	Number of waves required to observe maximum scour depth
R_*	Grain size Reynolds number
Re_w	Wave Reynolds number
$Re_{w,cr}$	Critical wave Reynolds number
R_c	Crest height
ρ_s	The density of the sediment
ρ_w	The density of the water
S	Maximum scour depth
S_s	Relative density of the sediment
S_t	Scour depth
σ	Grain size distribution of the backfill material
t	Time

$\tan\alpha$	Front slope of the structure
T^*	The time scale of the scour
$T_{m-1,0i}$	Incident spectral wave period in front of the structure
T_{max}	The time needed to observe maximum scour depth
τ	Bed shear stress on the backfill surface
τ_c	Critical shear stress of the backfill material
V	Water jet velocity
v_*	Bed shear velocity
V_w	Relative fall velocity
w_s	Fall velocity of the backfill material
x	Coordinate in the wave approach direction
x_A	Maximum accretion height distance to the crown wall
x_s	Maximum scour depth distance to the crown wall
z	Coordinate perpendicular to the wave approach direction

CHAPTER 1

INTRODUCTION

Coastal areas are used for many purposes by governments and private corporations. Coastal protection structures are built to keep these areas safe from wave-induced damages. One of these protection structures is coastal revetments. Rubble mound types are generally constructed, and the rear side of these structures are filled with earth materials. Coarse gravel, grass, concrete, or asphalt type cover can be applied on top of the rear side. These structures are built to protect recreational areas and highways. In Turkey, it is commonly built to protect Black Sea coastal roads. The overtopping in these areas causes significant damage to the landward sites. In this study, the rear side morphological changes of rubble mound revetments resulting from overtopping discharges are investigated by means of physical model experiments. This study investigates the rubble mound revetments, whose backfill area is covered with noncohesive erodible backfill materials or the construction phase of the rear side has not yet been completed.

This study was performed to find answers to the following research questions:

i. Under the same structure and wave conditions (such as backfill height, mean overtopping discharge), when do we reach an equilibrium state for the backfill profile change as the number of waves increases?
ii. When an equilibrium state is observed for the backfill surface profile change, what are the relations between the dimensions of the change (such as the maximum scour depth and maximum accretion height) and the mean overtopping discharge and backfill material features?
iii. What are the dimensionless expressions to predict the physical properties of the morphological changes (the scour and accretion areas) and time-related scour properties (time scale of the scour and the time

needed to observe the maximum scour depth), which are developed by using the wave number, mean overtopping discharge, and similar variables?

iv. Under the same structure (such as the same crest width and height) and wave conditions (such as the same significant spectral wave height and period) obtained from different irregular wave series, how do the backfill profile changes occur?

Overtopping discharge measurements and scour measurements are the two main stages of this study. First, irregular wave series were produced, and their properties were determined. Then, their corresponding discharges overtopping over the coastal revetment constructed in the wave flume were measured. After this stage, the experimental setup was prepared for the scour experiments. After each experiment was performed, the scour features at the rear side of the structure were measured. In the scope of this study, backfill surface profile change was investigated. While wave properties and the structure remained the same, the number of waves that attack the revetment was increased until an equilibrium form of the backfill profile was observed for each test. Effects of the overtopping discharges and backfill material properties on the rear side changes were examined. The dimensionless form of the time-dependent features of the rear side changes and the time scale of the scour were developed by using the number of waves, the median grain size of the backfill materials, and similar variables. Different irregular wave series having the same wave properties were produced and tested under the same structure conditions. The backfill surface profile changes obtained from these tests were compared.

In Chapter 2, the studies related to the overtopping and scouring processes are presented. The studies about scour contain the scour downstream of hydraulic flow control structures, scour behind the coastal protection structures due to tsunami overflow, and the scour rear side of the coastal protection structures due to wave overtopping.

The methodology of the study is presented in Chapter 3. Dimensional analysis of the parameters, the scale of physical features, the experimental setup, and physical model experiments, both overtopping discharge measurements and scour experiments, are presented.

In Chapter 4, the results of the study are presented. Wave properties and the overtopping discharge measurements are given. The presented scour results contain dimensionless expressions of the rear side changes and time scale.

In Chapter 5, the results of the study are discussed. Scale effects on the rubble mound model and hydrodynamic similarity requirements regarding the flow and sediment transport were discussed.

The conclusions and future recommendations are presented in Chapter 6.

CHAPTER 2

LITERATURE REVIEW

Since the study is about an overflow (wave overtopping) and its impact on the rear side of a structure, similar physical problems and related literature are briefly given in the chapter. Then, morphological changes downstream of hydraulic flow control structures are presented. After that, the studies about the rear-side of coastal dikes-wave overtopping interactions are given. Finally, the tsunami overflow effects behind the coastal protection structures are given.

2.1 Sluice Gate Studies

The studies about the hydraulic flow control structures are grouped into two as spillway structures and sluice gates. Scour downstream of sluice gates were studied by Rajaratnam (1981), Hassan and Narayanan (1985), Chatterjee et al. (1994), and Sarkar and Rey (2005). The erosion of loose beds resulting from turbulent plane jets of air and submerged water jets was studied by Rajaratnam (1981). By taking different grain sizes, apron lengths, sluice openings, and outlet velocities as variables in the physical model tests, Hassan and Narayanan (1985) examined the scour profiles formed by submerged water jets. Chatterjee et al. (1994) studied the scouring process resulting from horizontal water jets. The transportation of the eroded materials and the scour profiles were examined. The equilibrium scour stage was analyzed, and a maximum scour depth expression at this stage was produced as a function of the jet efflux thickness. By taking the critical shear stress, transport stage values are defined and used to develop transport formulas. Sediment uniformity effects on the scour due to submerged horizontal jets were examined by Sarkar and Dey (2005). For non-uniform sediment, if the geometric standard deviation of sediment increases, all the defined geometric features belonging to the scour and

accretion decreases. Also, practical approaches to apron foundation design were provided for both uniform and non-uniform sediments. This study differs from the mentioned studies in terms of flow conditions and tailwater depth.

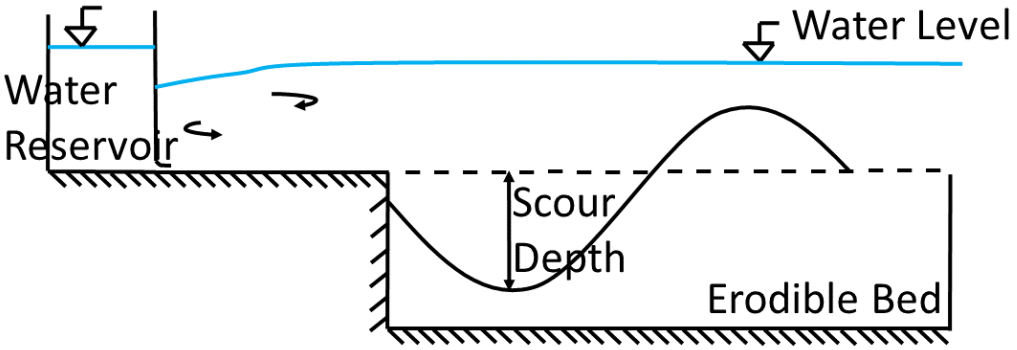

Figure 2.1. Definitive Sketch for Sluice Gate Studies (adapted from Hassan and Narayanan (1985))

Other researchers made changes to the experimental setup shown in Figure 2.1. Jayaratnam (1981) removed a part of the rigid apron and set the erodible bed starting from the gate outlet. Chatterjee et al. (1994) and Sarkar and Rey (2005) did not significantly change the presented figure and used a similar setup.

2.2 Spillway Studies

Scour downstream of spillway type structures were studied by Farhoudi and Smith (1985), Bornmann and Julien (1991), Stein et al. (1993), Dey and Raikar (2007), Dehghani et al. (2010), Emiroglu and Tuna (2011), and Ghodsian et al. (2012). Experimental tests about the scour hole development downstream hydraulic jump flows were performed by Farhoudi and Smith (1985). Bornmann and Julien (1991) conducted large-scale experiments to validate theoretical formulas regarding the scour downstream of grade control structures. The experimental results and the compared equilibrium scour formula were analyzed, and agreeable results were found. Stein et al. (1993) examined morphological changes in cohesive and noncohesive beds under jet diffusion influence. They analyzed the development of

scour holes and found that more than 90 percent of the scour forms rapidly. Dey and Raikar (2007) studied the scouring process due to a high vertical drop in noncohesive sediment beds through physical model tests. They used densimetric Froude number in the analysis and defined its relation with scour geometries. Physical model experiments regarding the scour downstream of weirs having tailwater were conducted by Dehghani et al. (2010). Emiroglu and Tuna (2011) studied the impact of tailwater depth on scour development downstream of chutes consisting of steps. Dimensional analysis and experimental work were conducted to clarify the effects of the variables on local scour. Morphological changes in noncohesive sediment beds due to sediment carrying free-overfall water jets were experimentally investigated by Ghodsian et al. (2012). They found that sediment in the jets shrinks the scour holes compared to the clear water jets. Flow conditions and tailwater depth are the main differences between the mentioned studies and this study.

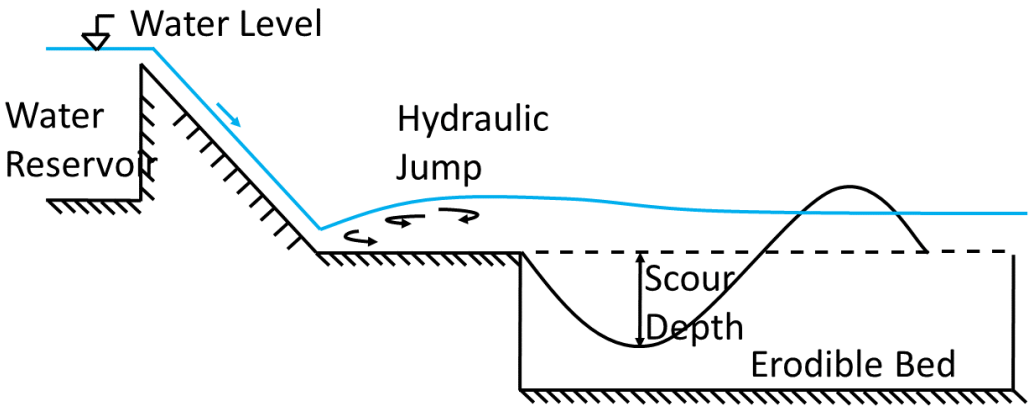

Figure 2.2. Definitive sketch for spillway studies (adapted from Farhoudi and Smith (1995))

Other researchers also used a similar setup shown in Figure 2.2., but they made a few changes. Bornmann and Julien (1991) used an inclined erodible bed. Instead of using an inclined ramp, Stein et al. (1993) used a horizontal ramp and studied scour downstream of a headcut. Dey and Raikar (2007) examined scour resulting from vertical drops. Dehghani et al. (2010) used rectangular sharp-crested weirs. Emiroglu and Tuna (2011) changed the inclined ramp with a stepped one. Finally, Ghodsian et al. (2012) fed the flow with sediment.

2.3 Coastal Dike Studies

Morphological changes behind coastal protection structures due to wave overtopping were studied for coastal dike structures. This structure type is mainly used in Northern European countries, and the studies are focused on the change in the crest of these structures and its rear side covers such as grass or asphalt. Examination of wave overtopping processes of coastal protection structures were gathered into EurOtop (2018). The physical features of wave overtopping, such as average discharge amount, overtopping velocities, were formulated for the related structures. These formulas were synthesized using laboratory and field measurements. Also, the safety assessments of coastal dike-type structures having 1:2.5 or milder slopes were performed. This study examines the structure having a steeper slope and uncovered rear side part open to expose scouring and deposition. Breaching of coastal dikes resulting from wave overtopping and overflow was studied by Oumeraci et al. (2005). Grass failure time and infiltration model were obtained from the developed numerical model. Sea dikes consisting of a sand core covered with clay protection layers with grass reinforcements were numerically studied by Stanczak (2008) for dike breaching due to wave overtopping. As a result of the model, grass erosion time, clay erosion time, core erosion time, total breaching time, peak outflow discharge, and final breach width are acquired. Breaching of coastal dikes due to wave overtopping was numerically modeled to investigate the dike erosion process and discharge coefficient by Schmocker and Hager (2010). In order to determine the discharge coefficient, four different sets of overflow depth, measured from the crest elevation, were applied to the model with two crest radiuses. They demonstrated that under the steady flow condition, when overtopping starts, breach discharge rises rapidly, leading to erosion. After that, breach discharge has decrease trend. This trend continues until the discharge is equal to the breach discharge. Steendam et al. (2014) studied dikes having landward grass-covered slope under wave overtopping effects. The relation between landward side slope and overflow causing the erosion was analyzed. It was found that if landward side steepness increases, erosion occurs

faster. Bomers et al. (2018) created a numerical model to simulate coastal dike erosion due to wave overtopping. In their model, coastal dikes with an asphalt road were used to acquire its impact on the erosion process. They found that the erosion occurred more at the transition zone because the asphalt has a lower roughness value than grass. Warmink et al. (2018) physically modeled six different seaside slopes to examine transition impacts on the coastal dike erosion process. They found that the erosion process changes dramatically with transitions because transitions create different wave overtopping discharges under the same wave conditions.

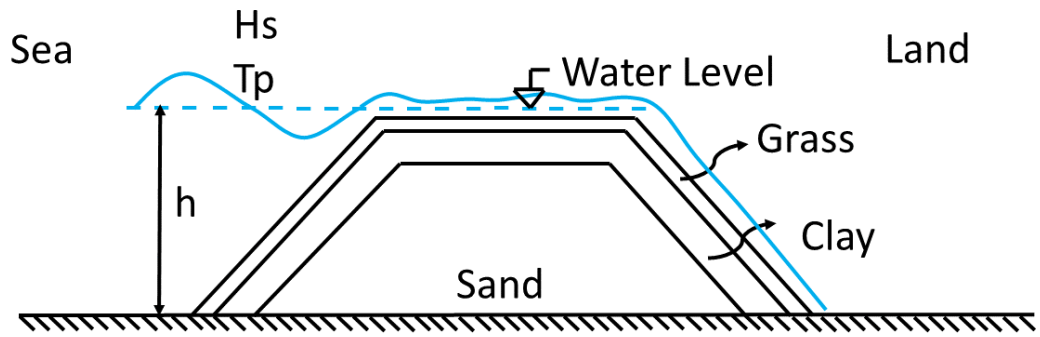

Figure 2.3. Definitive sketch for coastal dike studies (adapted from Oumeraci et al. (2005))

Instead of studying wave overtopping impact, Stanczak (2008) analyzed wave-breaking effects. Schmoker and Hager (2010) used a very similar setup illustrated in Figure 2.3. Steendam et al. (2014) added geometric transitions such as grass-road on the landward side of the slope. Also, Bomers et al. (2018) and Warmink et al. (2018) designed geometric transitions on the landward side.

2.4 Tsunami Overflow Studies

The morphological changes behind coastal structures resulting from tsunami overflow show similarities in terms of physical process. Comparisons between 2011 Tohuku Tsunami field measurements and the scour calculation formulas given by previously mentioned researchers such as Rajaratnam (1981) and Stein et al. (1993) were made by Bricker et al. (2012). They found that the approach of Rajaratnam (1981) is significantly higher than the measurements. Also, the approach of Stein et

al. (1993) to scour prediction shows good agreement with the field measurements. Scour around the coastal structures due to tsunami overflow was numerically modeled by Jayaratne et al. (2014). The predictive scour depth model results illustrate that the higher the wave pressure effect is, the higher the relative scour depth is. Also, scour minimization can be acquired with a higher structure under the same landward slope condition. Scour behind seawalls having an artificial trench behind it was numerically and physically studied by Tsujimoto et al. (2014) to clarify trench influences on the scour process. It was found that an artificial trench could be used behind coastal structures to decrease overflow velocity and tsunami energy. Using a trapezoid shape trench is more effective than a rectangular shape to reduce tsunami energy. The morphological changes behind coastal structures and the failure mechanism of these structures resulting from tsunami overflow were studied by Jayaratne et al. (2016). They defined six major failure types as scour at the leeward toe, crown armor slip, failure of leeward sloped armor, seaward toe and armor failure, overturning failure, and breaching of the parapet wall, considering the field surveys and observations. An approach to analyzing the forces created by a tsunami initiation and its overflow was presented by McGovern et al. (2019). They obtained a scour time series occurring at the front face of a rectangular cylinder using the defined approach to produce tsunami overflow.

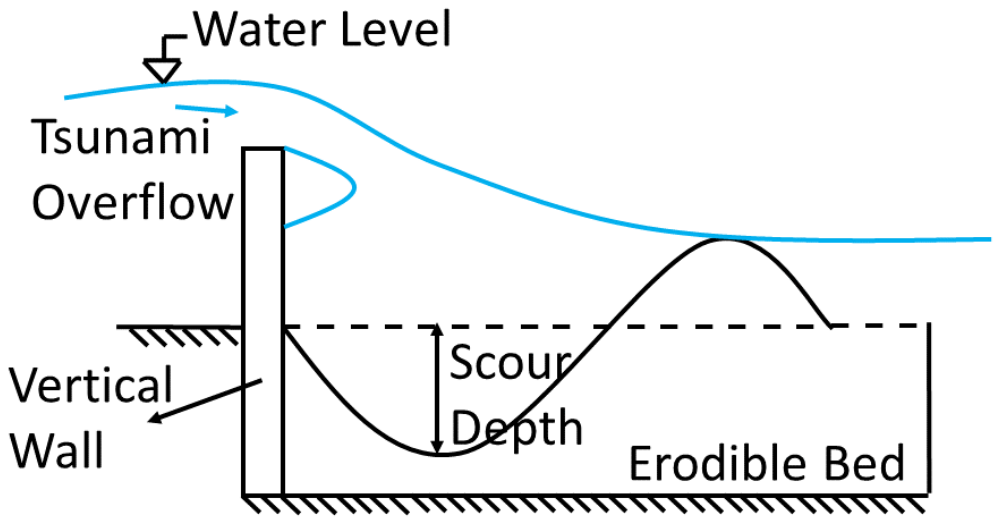

Figure 2.4. Definitive sketch for tsunami studies (adapted from Tsujimoto et al. (2014))

Instead of using experimental data, Bricker et al. (2012) studied with the field measurements. Jayaratne et al. (2014) analyzed seawalls instead of vertical walls. Jayaratne et al. (2016) investigated scour at the rear side of coastal dikes. Mcgovern et al. (2019) used onshore structures and analyzed the scour around these structures.

2.5 Weir Studies

Scour downstream of weirs shows similarities in terms of physical process. Chen et al. (2005) investigated a scour downstream of a submerged weir. They found that geometrical properties of the structure, sediment grain size, and critical flow velocity were the parameters affecting the morphological changes majorly. They also generated a formula to predict the size of the equilibrium scour hole. Guan et al. (2016) studied the scour upstream and downstream of a submerged weir by performing laboratory experiments. From the experiments, scour and fill process upstream of the weir was obtained and normalized with the tailwater depth. Wang et al. (2018a) examined the impact of upstream weir slope on the scouring process. They used both coarse and fine sediment in the conducted experiments. They found that the slope created a slight decrease in the scour depth downstream of the weir if

the sediment transport type was a bedload type. If the transport type was a suspended type, there was no impact of the weir slope on the scour. Si et al. (2018) investigated the scour downstream of a weir resulting from a plunging jet. They used a non-erodible bed upstream of the weir. In the experiments, they used particle image velocimetry. By obtaining the velocities, they analyzed energy scour relations. The effects of downstream slope on the scouring process were investigated by Wang et al. (2018b). By combining the available data from the studies (Wang et al. (2018a) and (2018b)) and new laboratory experiments, detailed analyses of the parameters such as weir height, sediment coarseness, and weir slope on the scouring process by presented by Wang et al. (2019).

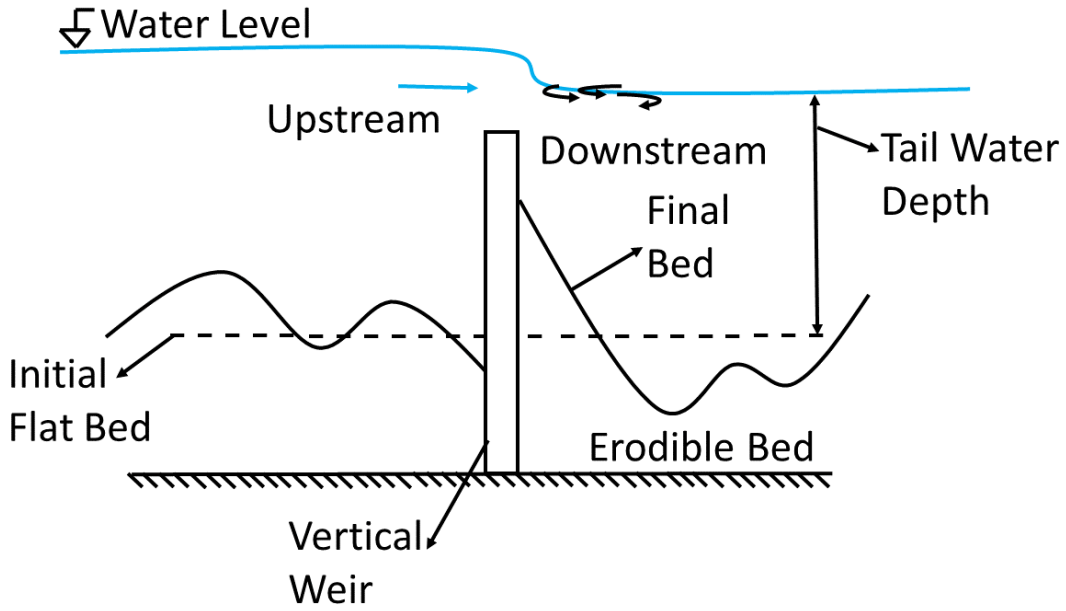

Figure 2.5. Definitive sketch for weir studies (adapted from Guan et al. (2016))

Other researchers used different experimental setups. Chen et al. (2005) used a dam shape submerged weir instead of a rectangular shape weir. Wang et al. (2018a) used an upstream weir slope. Si et al. (2018) used a non-erodible bed upstream of the weir. Wang et al. (2018b) used a downstream weir slope.

CHAPTER 3

METHODOLOGY

Changes rear side of the rubble mound revetments resulting from wave overtopping were investigated by physical model experiments. Before the experiments were conducted, dimensional analyses of the related parameters were performed. Then, scaling of the rubble mound revetment was done to determine the properties of the modeled revetment. After that, the experimental setup was prepared. Then, overtopping and scour experiments were carried out.

3.1 Dimensional Analysis

A rubble mound revetment structure consisting of core, filter, and armor layers was used in the experiments. Besides, a crown wall from the crest to the core layer was placed behind it. Features of the backfill materials, structures, and morphological changes are illustrated in Figure 3.1.

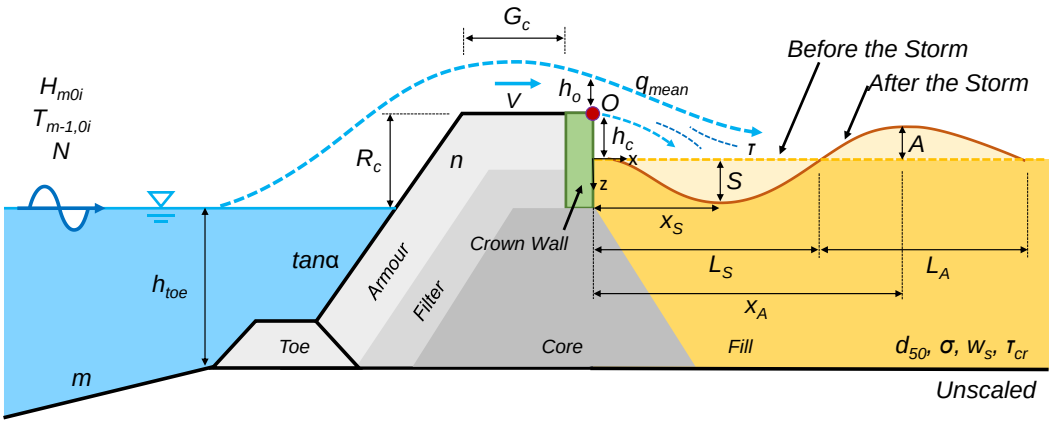

Figure 3.1. Scour rear side of a rubble mound revetment

In Figure 5, the overtopping process and its results as scour and accretion are shown. Structure related parameters are defined as h_{toe} water depth at the toe (kept constant

0.24 m), R_c crest height (m), G_c crest width (m), $\tan\alpha$ front slope of the structure (constant, 1 vertical/ 1.5 horizontal is selected), n porosity, h_c backfill height (m). Overflow related parameters are defined as H_{m0i} incident spectral significant wave height in front of the structure (m), $T_{m-1,0i}$ incident spectral significant wave period in front of the structure (s), N number of waves required to observe equilibrium scour profile, h_o thickness of the water jet (m), V water jet velocity (m/s), ρ_w the density of the water (kg/m^3), q_{mean} mean overtopping discharge per unit width ($m^3/s/m$). Backfill material related parameters are defined as d_{16} diameter of the backfill material that 16 percent (in volume) of the sediments are finer, d_{50} the median diameter of the backfill material (m), d_{84} diameter of the backfill material that 84 percent (in volume) of the sediments are finer, σ grain size distribution of the backfill materials (d_{84}/d_{16}), ρ_s the density of the sediment (kg/m^3), τ bed shear stress on the backfill surface (Pa), τ_{cr} critical shear stress of the backfill material (Pa), w_s fall velocity of the backfill material (m/s). The rest of the parameters, including morphological changes, are defined as S maximum scour depth (m), A maximum accretion height (m), T^* the time scale of the scour (s),T_{max} the time which maximum scour depth is observed, x_S maximum scour depth distance to the crown wall (m), x_A maximum accretion height distance to the crown wall (m), L_S width of the scour hole in wave direction (m), L_A width of the accretion in wave direction (m), m bed slope (1/20 is selected), g gravitational acceleration (9.81 m/s^2), x coordinate in the wave approach direction (m) (perpendicular to the crown wall), z coordinate perpendicular to the wave approach direction (m), t time (s).

The morphological changes resulting from wave overtopping can be expressed as equation (3.1) given below, considering the parameters above.

$$\varphi\left(\begin{array}{c} H_{m0i},\ T_{m-1,0i}, N,\ T_{max},\ T^*, \tan\alpha, m,\ h_{toe},\ n, \\ R_c,\ G_c,\ h_c,\ h_o,\ d_{50},\ \sigma,\ g,\ \rho_s,\ \rho_w,\ q_{mean},\ V, \\ \tau,\ \tau_{cr},\ w_s,\ S,\ A,\ x_S,\ x_A,\ L_S,\ L_A,\ x,\ z,\ t \end{array}\right) = 0 \quad (3.1)$$

h_o, V, and τ are the parameters that could not be measured, and these variables are excluded from equation (3.1). Also, the parameters τ_{cr} and w_s are dependent on d_{50}.

Therefore, these parameters are excluded. In addition, exclusion of the parameters H_{m0i}, $T_{m-1,0i}$, $\tan\alpha$, m, h_{toe}, n, R_c, and G_c is done because they indirectly affect the scouring process, controlling the overtopping discharge. Finally, equation (3.1) turns into:

$$\varphi\begin{pmatrix} q_{mean},\ h_c,\ d_{50},\ \sigma,\ g,\ \rho_s,\ \rho_w,\ S,\ A, \\ x_S,\ x_A,\ L_s,\ L_A,\ T^*,\ T_{max},\ x,\ z,\ t, \end{pmatrix} = 0 \tag{3.2}$$

In order to convert the parameters into dimensionless form, the π theorem of Vaschy and Buckingham was applied by taking g, ρ_s, and d_{50} as independent parameters. The dimensionless form of these parameters is presented in equation (3.3) given below.

$$\varphi\begin{pmatrix} h_c/d_{50},\ \sigma, \Delta\ or\ (\rho_s/\rho_w - 1),\ q_{mean}^2/[\Delta g d_{50}^3],\ \\ S/d_{50},\ A/d_{50},\ x_S/d_{50},\ x_A/d_{50},\ L_S/d_{50},\ L_A/d_{50}, \\ T_{max}^2 g/d_{50},\ {T^*}^2 g/d_{50},\ x/d_{50},\ z/d_{50},\ t^2 g/d_{50} \end{pmatrix} = 0 \tag{3.3}$$

In equation 3.4, S, A, x_S, x_A, L_S, L_A, T_{max}, and T^* are dependent parameters and h_c, σ, Δ, q_{mean}, x, z, and t are independent parameters. The above equation could also be written as equation 3.4.

$$\begin{bmatrix} S/d_{50}, A/d_{50}, \\ x_S/d_{50}, x_A/d_{50}, \\ L_S/d_{50}, L_A/d_{50}, \\ T_{max}^2 g/d_{50}, \\ {T^*}^2 g/d_{50} \end{bmatrix} = \varphi\begin{pmatrix} h_c/d_{50},\ \sigma, \Delta\ or\ (\rho_s/\rho_w - 1), \\ q_{mean}^2/[\Delta g d_{50}^3],\ x/d_{50}, \\ z/d_{50},\ t^2 g/d_{50} \end{pmatrix} \tag{3.4}$$

In equation (3.4), the parameters on the left side are dependent, and the parameters on the right side are independent.

After the physical model experiments are completed, the data acquired from them were used to determine the nondimensional parameters mentioned above.

Scour progression was acquired by taking regular measurements. The maximum scour depth occurrence and the time to observe this occurrence were obtained by using these measurements. Changes of scour depth around structures in time were defined by Sumer and Fredsøe (2002) as

$$S_t = S[1 - \exp(-t/T^*)] \quad (3.5)$$

in which S_t is the scour depth, S is the maximum scour depth, t represents time, and T^* is the time scale of the scour. In this study, rather than using the approach of Sumer and Fredsøe (2002), obtaining the tangent of the curve at $S_t = 0$, to find the time scale, the area method of Fuhrman et al. (2014), a more proper way to apply experimental data, was used.

3.2 Scaling

The Froude model criterion is mostly used in hydrodynamic models of coastal engineering (Hughes, 1993). The principle of this approach uses gravitational forces to balance inertial forces occurring at a free surface. $Fr = V^2/gh$ is the definition of Froude number. In the given expression, V is the water particle velocity, h is the water depth, and g is the gravitational acceleration. If this criterion is used in modeling, Froude numbers both model and prototype ($Fr_m = Fr_p$) must be equal. The subscripts m and p represent model and prototype, respectively. The model length scale (λ_L) is set to create geometric similarities by making ratios of $L_m/L_p = \lambda_L$ where L represents parameters in length dimension. Also, $\lambda_T = \lambda_L^{0.5}$ and $\lambda_q = \lambda_L^{1.5}$, where λ_T is the time scale and λ_q is the scale of mean overtopping discharge per unit, are obtained by using model length scale. Water density effect was also another issue with modeling the rubble mound revetment. In the prototype, saltwater was considered, while in the experiments, freshwater was used. Hudson et al. (1979) defines dynamic similarity conditions to determine weight scale (λ_w). Using the method given by Hudson et al. (1979), the model stones used in the armor and filter were determined. Thus, the water density impact in the rubble mound revetment was solved. When the rubble mound revetment was modeled, viscous scale effects were considered, and the approach given by Burcharth et al. (1999) was used. The approach considers the ratio of the pore velocities both model and prototype according to the Froude scaling laws. By adjusting the median diameter of the core materials, sufficient wave energy dissipation was created. Hughes (1993)

stated that although the friction forces between the armor units next to each other in the prototype were negligible, in the model, due to the rougher surface of the armor units, the frictional forces could not be similar. Therefore, the armor units used in the revetment model were painted, and a smoother surface was provided.

The parameters used to determine stone sizes will be given below:

- λ_L (length scale of the model) $= 1/36$
- $\rho_{s,m}$ (specific weight of the stones used in the model) $= 2700\ kg/m^3$
- $\rho_{w,m}$ (specific weight of the water used in the model) $= 1000\ kg/m^3$
- $\rho_{s,p}$ (specific weight of the stones used in the prototype) $= 2650\, kg/m^3$
- $\rho_{w,p}$ (specific weight of the water used in the prototype) $= 1025\ kg/m^3$

Features of the coastal revetment are given in Table 1, where D_{n50} is the median stone size diameter.

Table 3.1. Features of the rubble mound revetment

	$D_{n50,prototype}$ (m)	$D_{n50,model}$ (cm)	Stone Class (Prototype) (tons)	Stone Class (Model)(gr)	n_{model} (porosity)
Armor	1.72	4.46	12-15	210-265	0.38
Toe	1.72	4.46	12-15	210-265	0.38
Filter	0.77	1.99	0.4-2	7-35	0.41
Core	0.36	1.30	0.01-0.25	0.4-10	0.41

3.3 Experimental Setup

The experiments were performed in a wave flume having 1.0 m depth, 6.0 m width, and 26.9 m length in Middle East Technical University, Civil Engineering Department, Coastal and Ocean Engineering Laboratory. 6 m wide single block piston-type random wave generator, produced by Danish Hydraulic Institute (DHI), was used in the experiments.

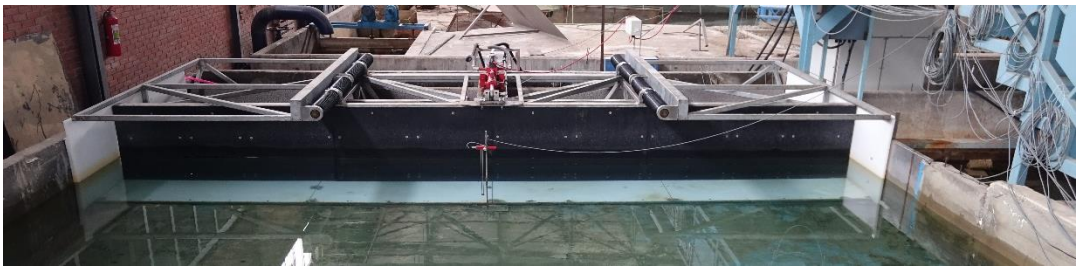

Figure 3.2. Piston type wave generator

The flume has a passive wave absorption system. Excluding the length of the wave generator and the absorption system, the net length of the wave flume is 20.6 m. It has an inner channel having 1.5 m in width. To minimize the time required for flattening the rear side taking measurements while providing enough workability in the flume and also to minimize the three-dimensional effects of small period waves, the inner channel was divided into two, 0.9 m and 0.6 m wide channels. The placement of the sea bed and the cross-section were performed in the 0.9 m wide channel. Although the 0.9 m wide channel was used in the experiments, preparing the rear side (flattening the erodible bed) and taking the regular measurements to determine to scour depth change in time are more than 70 percent of the time required to complete each experiment. First, a 4.7 m long flat bottom having 0.02 m thickness was constructed in the channel. Then, a 7.2 m long bottom having a slope of $1/20$ was constructed. The location of the wave gauges, the overtopping collection site, the cross-section, and the slope are shown in Figure 3.3.

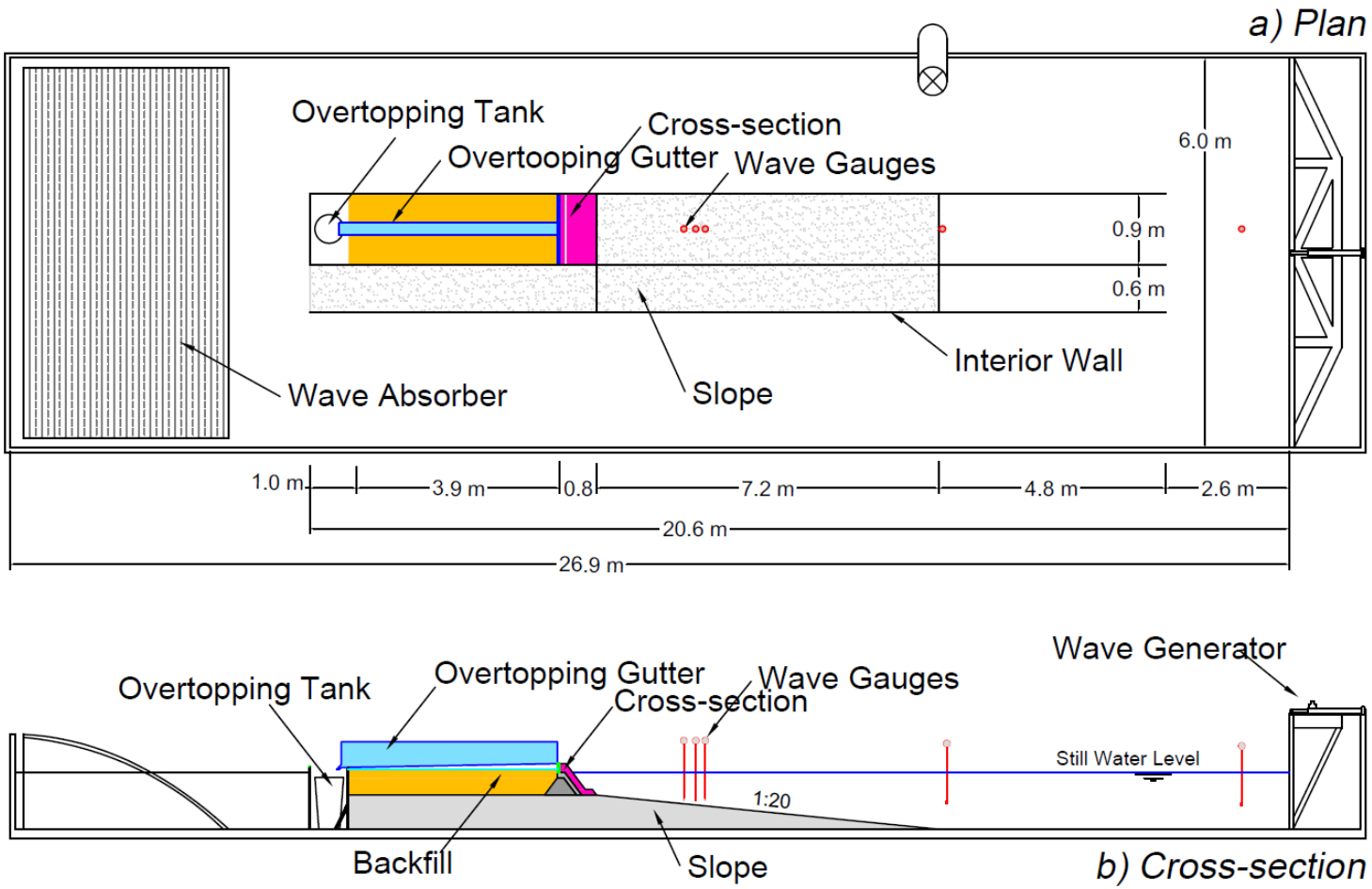

Figure 3.3. Drawing of the experimental setup (Unsclaed, dimensions are in meter)

A square hole perforated sheet (Figure 3.4) consisting of 2x2 cm holes was used to stabilize armor units, and 93 percent of it is an open area.

Figure 3.4. Cross-section with a square hole perforated sheet

Since the passive wave absorption system is used in the wave flume, multi-wave reflection occurs during the experiments. Therefore, three wave gauges were placed in front of the structure at a distance of 3 m to analyze the reflection impact. Mansard and Funke (1980) defines how to determine distances between the wave gauges. Using the method of Mansard and Funke (1980), reflection coefficients were determined. General view of the wave flume, including the backfill area, the revetment, the wave gauges, and the bottom slope, are shown in Figure 3.5.

Figure 3.5. General view of the wave flume

Water-permeable geotextile fabric (Figure 3.6) was used to cover the rear side from the crown wall to the overtopping discharge collection site to prevent the smallest backfill material escape through the revetment.

Figure 3.6. Geotextile cover application before the cross-section placement

3.4 Physical Model Experiments

First, wave calibration tests were performed. Then, overtopping discharge measurement tests were conducted. Finally, scour experiments were carried out.

3.4.1 Wave Calibration and Overtopping Tests

First, irregular wave series were determined according to the planned wave properties (incident spectral wave height, wave steepness). Each produced wave series are set to have approximately $N = 1000$ individual waves. The studies regarding the similar overtopping, scour, and stability in the literature were carried out with the wave series generated from the Texal-Marsen-Arsloe (TMA) spectrum. In this study, the same spectrum was used to generate wave series. The TMA spectrum can also be defined as a shallow-water type of the JONSWAP spectrum. The sampling frequency of 0.6 m long DHI-202 type wave gauges, used in the experiments to record generated wave series, was selected and kept as 40 Hz. The whole recording was in voltage values. Each day before the tests started, linear

calibration coefficients for the related wave gauges were acquired. Thus, using these coefficients, the recorded time series of water surface elevations were transformed into meter values.

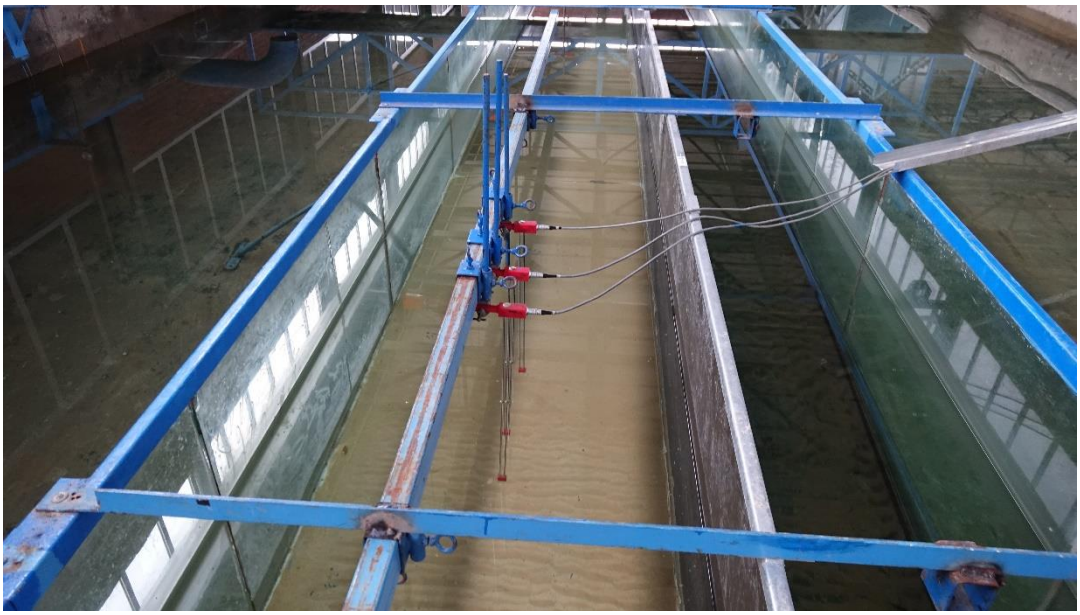

Figure 3.7. The group of wave gauges placed at the slope

Second, wave overtopping discharge measurement tests were conducted for the determined wave series. A galvanized steel sheet was used to build the overtopping gutter having 0.25 m width. The discharge was transferred to the overtopping tank through the gutter mounted at Point O (Figure 3.1). The tests were performed three times for each wave series. At the end of each test, the mean overtopping discharge ($m^3/s/m$) rates were determined. The coastal revetment with the overtopping gutter was shown in Figure 3.8.

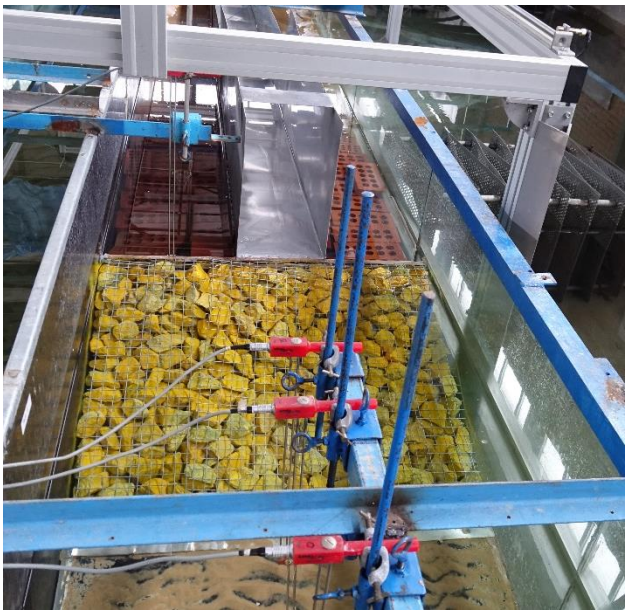

Figure 3.8. The coastal revetment with the overtopping gutter

3.4.2 Scour Experiments

The final step of the experiments is scour tests. For these tests, overtopping gutter is removed from the rear side of the structure. In these tests, wave series having different incident spectral wave heights and periods (H_{m0i}, $T_{m-1,0i}$) were used. Also, tests were repeated for different backfill materials (d_{50}) and backfill heights (h_c).

The morphological changes (scour and accretion) at rear side of the revetment were measured with a computer-controlled bottom profiler (Figure 3.9). The profiler has a performing range of 1.5 m x 3.0 m area. It has below 1.0 mm horizontal positioning accuracy. The laser sensor used in the system to take vertical measurements is the Banner® brand LTF24IC2LDQ model. Its accuracy is below 0.3 mm.

Figure 3.9. Experimental setup with the computer-controlled bottom profiler

The rear side surface measurements were taken on seven lines in the direction of wave propagation (Figure 3.10), starting from the crest and extending along the

backfill area. By taking the regular measurements of these seven lines, the evolution of the backfill area (scour and accretion) was acquired. The length of these lines was adjusted to contain both scour and accretion regions. The extension of the lines was ended when the changes in the backfill area become negligible. The interval between two lines was taken as $\Delta x = 0.1\ m$. While determining the change of the rear side geometries, the mean of these seven lines was taken. The final bed profiles in the appendices (Figure 0.1 to 0.27) for the whole experiments (S-Test-1 to 27) are the mean of these defined seven lines.

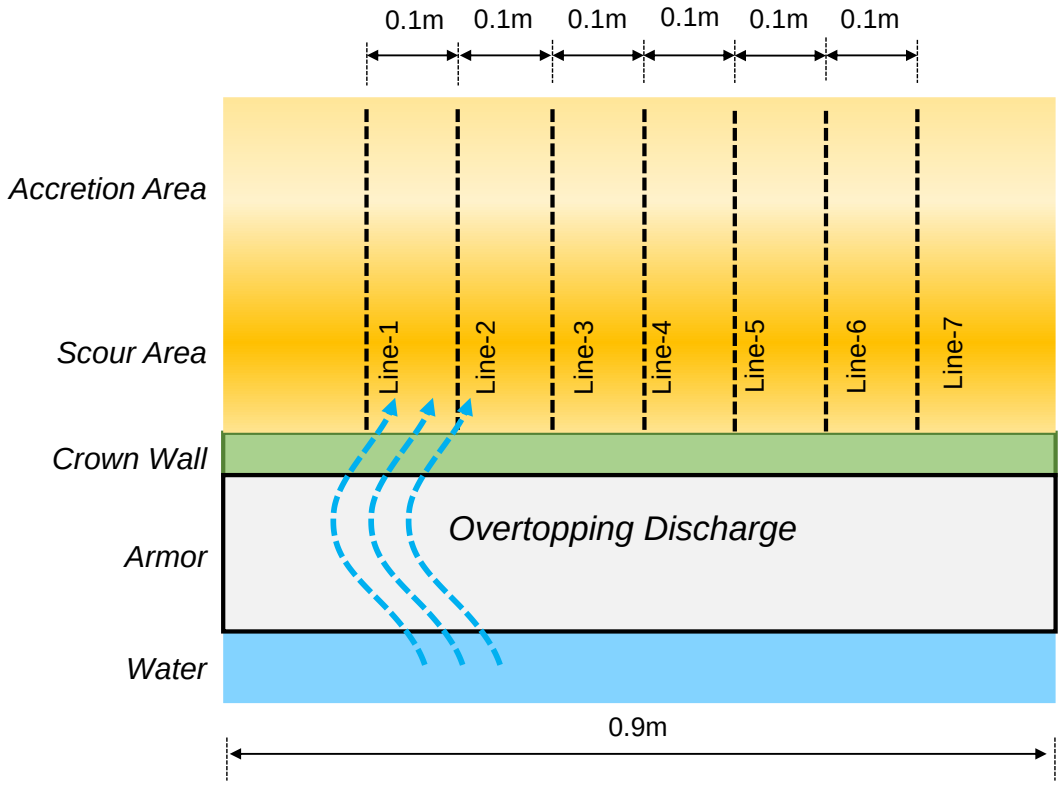

Figure 3.10. The lazer lines measured to acquire rear side changes (not to scale)

In the scour experiments, each test was ended when the equilibrium scour depth was observed. Completion of each test took two to four days. Observation of the equilibrium state took up to 60000 waves in some experiments. The original plan for each scour test was to take regular measurements after the completion of the generated wave series, which are approximately $N = 1000$ waves. However,

flooding condition (The scour hole was filled with water.) was observed in some experiments. Thus, to take accurate measurements, the water in the flooded area had to be evacuated. Since removing the floodwater could create changes at the rear side of the structure, the flood water was drained and refilled very slowly. This process was time-consuming. Therefore, if flooding is observed, a new procedure of measuring the rear side was followed. The first three profile measurements (up to $N = 3000$ waves) were acquired as in the original plan in case of flooding (after each 1000 waves). Then up to $N = 10000$ waves, after the completion of each 3000 waves, profile measurements were performed. After $N = 10000$ waves, after each 5000 waves, profile measurements were taken. This measurement interval was kept constant till the equilibrium state is observed. For each test, if the relative change in the maximum scour depth is below one percent for five consecutive measurements, the test was considered as complete, and the scour hole depth was considered as in an equilibrium state. In the experiments where flooding occurred, the acceptance of the equilibrium state was done when the relative change in the maximum scour depth is below one percent for two consecutive measurements.

While the regular measurements were taken to determine the relative change in the maximum scour depth, the area starting from the crown wall and extending to the maximum scour depth location was measured. Total relative backfill profile change was not obtained due to time issues. For S-Test-6, the obtained measurements corresponding to the completion of each 1000 waves were presented in the appendices. Also, the backfill profile changes for S-Test-6 were presented with the seven measured lines instead of the mean of these seven lines. When the individual lines were compared for the maximum scour depth for S-Test-6, 21 percent differences were found between the lowest and highest.

Before the experimental stage of the study was started, one of the main aims of this study was to determine the scour properties (such as equilibrium scour depth) when it reaches an equilibrium state. Unfortunately, in the scour tests, the initially planned interval to take regular measurements (after the completion of each 1000 waves) was

not followed in some tests due to the flooding of the rear side. Therefore, the time interval in some tests (such as Figure 0.36) was increased up to 5000 waves. Due to the increase in the time interval, the acquired maximum scour depth was considered as equilibrium scour depth. Instead of defining them individually, the maximum scour depth (S) was used in the analysis.

CHAPTER 4

RESULTS

4.1 Overtopping Results

Each generated wave series with around 1000 individual waves was tested thrice to obtain properties of the series and overtopping discharges. In addition, three different wave series (O-Test-07) sharing the same wave properties (incident spectral wave height, period) were generated and tested. The acquired wave properties and discharges were presented in Table 4.1. In Table 4.1, H_{m0i} is the incident spectral significant wave height, $T_{m-1,0i}$ is the incident spectral significant wave height, $H_{m0i}/\left[\left(gT_{m-1,0i}^{2}\right)/2\pi\right]$ is the wave steepness, q_{mean} is the measured overtopping discharge, and R_c is the crest height.

Table 4.1. The results of the overtopping tests

Overtopping Test No.	H_{m0i} (m)	$T_{m-1,0,i}$ (s)	$H_{m0i}/[g(T_{m-1,0i})^2/2\pi]$	Overtopping Discharge, model (lt/s/m)	$q_{mean}/sqrt(gH_{m0i}^3)$	R_c/H_{m0i}
O-Test-01a	0.148	1.858	0.028	1.7686	0.0099	0.6069
O-Test-01b	0.148	1.858	0.028	1.7725	0.0099	0.6061
O-Test-01c	0.148	1.859	0.027	1.8248	0.0103	0.6093
O-Test-02a	0.121	1.596	0.030	0.4117	0.0031	0.7436
O-Test-02b	0.120	1.595	0.030	0.4181	0.0032	0.7481
O-Test-02c	0.119	1.598	0.030	0.3990	0.0031	0.7569
O-Test-03a	0.105	1.505	0.030	0.1957	0.0018	0.8543
O-Test-03b	0.105	1.504	0.030	0.1940	0.0018	0.8546
O-Test-03c	0.105	1.505	0.030	0.1974	0.0019	0.8566
O-Test-04a	0.090	1.378	0.030	0.0458	0.0005	1.0052
O-Test-04b	0.090	1.378	0.030	0.0496	0.0006	1.0030
O-Test-04c	0.089	1.380	0.030	0.0439	0.0005	1.0134
O-Test-05a	0.097	2.275	0.012	0.5951	0.0063	0.9310
O-Test-05b	0.097	2.273	0.012	0.5925	0.0063	0.9305
O-Test-05c	0.096	2.273	0.012	0.6057	0.0065	0.9353
O-Test-06a	0.081	1.494	0.023	0.0258	0.0004	1.1068
O-Test-06b	0.081	1.492	0.023	0.0231	0.0003	1.1061
O-Test-06c	0.081	1.493	0.023	0.0195	0.0003	1.1062
O-Test-07-1a	0.080	1.287	0.031	0.0148	0.0002	1.1196
O-Test-07-1b	0.081	1.288	0.031	0.0144	0.0002	1.1169
O-Test-07-1c	0.080	1.288	0.031	0.0118	0.0002	1.1289
O-Test-07-2a	0.081	1.287	0.031	0.0143	0.0002	1.1091
O-Test-07-2b	0.081	1.286	0.031	0.0133	0.0002	1.1076
O-Test-07-2c	0.082	1.286	0.032	0.0131	0.0002	1.1034
O-Test-07-3a	0.081	1.287	0.031	0.0156	0.0002	1.1088
O-Test-07-3b	0.082	1.286	0.032	0.0205	0.0003	1.1039
O-Test-07-3c	0.081	1.287	0.031	0.0195	0.0003	1.1106
O-Test-08a	0.073	1.234	0.031	0.0036	0.0001	1.2315
O-Test-08b	0.073	1.237	0.031	0.0034	0.0001	1.2324
O-Test-08c	0.073	1.233	0.031	0.0031	0.0001	1.2339

The results of the overtopping experiments are compared with the EurOtop (2018) approach. In EurOtop (2018), the average overtopping discharge value for rubble mound breakwaters is given equation (4.1).

$$\frac{q_{mean}}{\sqrt{gH_{m0i}^3}} = 0.09exp\left[-\left(1.5\frac{R_c}{H_{m0i}\gamma_f\gamma_\beta}\right)^{1,3}\right] \tag{4.1}$$

In the equation (4.1) given above, γ_β is defined as an influence factor for oblique wave attack and given as 1 for the waves perpendicular to the structure. γ_f is defined as an influence factor for the permeability and roughness of the slope. It is given as 0.40 for the structures having permeable core and armor consisting of 2 layers. $\sigma(0.09) = 0.0135$ and $\sigma(1.5) = 0.15$ are given to define the reliability of the equation (4.1). In Figure 4.1, a comparison between the experimental data and EurOtop's (2018) approach with 90 % reliability limits is given.

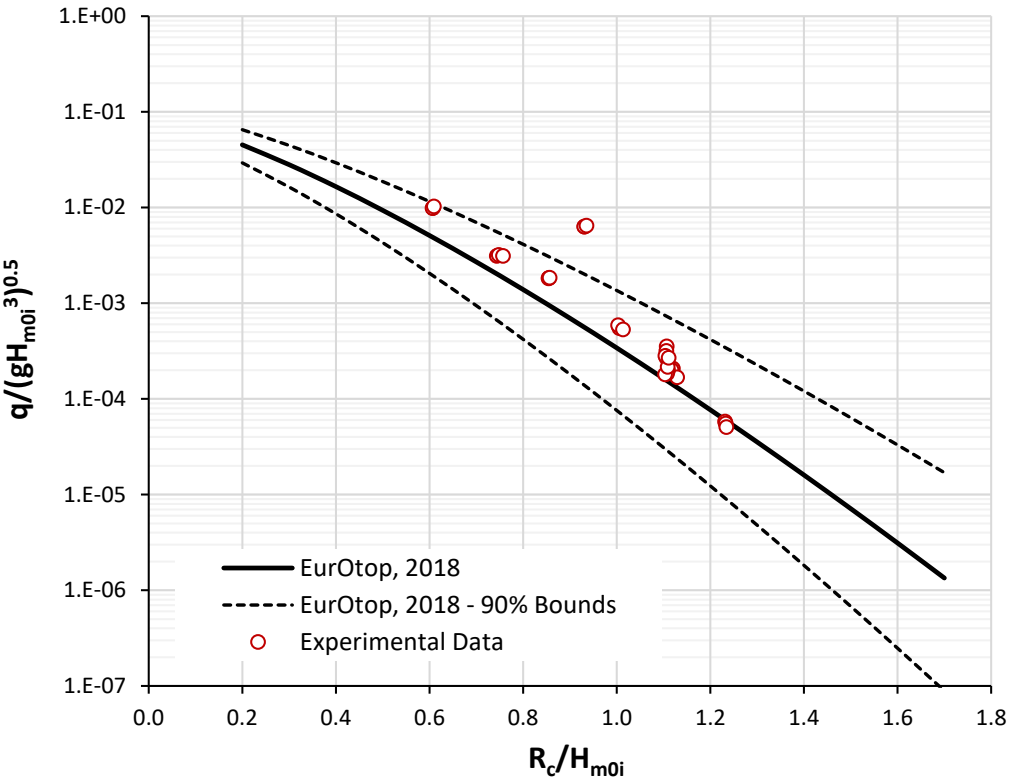

Figure 4.1. Comparison between the experimental data and EurOtop (2018)

From Figure 4.1, it can be seen that experimental results and EurOtop's (2018) approach with 90 % reliability limits are in good agreement. When the given approach in EurOtop (2018) and experimental data are statistically compared, correlation coefficient, $r = 0.992$, ($R^2 = 0.984$), mean absolute error, $MAE = 70.2$ %, root mean square error, $RMSE = 0.0021$, normalized mean bias, $NMB = 1.0028$ are found.

4.2 Scour Results

Characteristics of the wave series and the revetment geometry mainly affect the overtopping discharge amount. Therefore, the front side of the revetment was kept the same in the conducted experiments. The variable parameters are overtopping discharge amount, backfill height, and median grain size of the backfill materials. The impact of the overtopping waves, which can be considered as water flow, is strongly connected to the rear side geometry of the revetment because the water drop occurs differently when the geometry changes. The results of the scour tests are presented in Table 4.2.

Figure 4.2. Seaside view of the S-Test-6

By using the lazer bed profiler, regular measurements were performed during the experiments. The essential geometrical properties of the morphological changes (scour and accretion) were acquired by using the obtained regular measurements. The results are presented in Table 4.2. In Table 4.2, T_{max} is the time when the maximum scour depth is observed and T^* is the time scale of the scour. The overtopping discharge values given in Table 4.2 are the mean of the three conducted overtopping discharge measurement tests. When the time scale of the scour was calculated, the below-given approach by Fuhrman et al. (2014) was used.

$$T^* = \int_0^{T_{max}} \frac{S - S_t}{S} dt \tag{4.2}$$

In equation 4.2, T^* is the time scale, S is the maximum scour depth, and S_t is the scour depth.

Table 4.2. The results of the scour experiments

Scour Test No.	H_{m0i} (m)	$T_{m-1,0i}$ (s)	$H_{m0i}/[g(T_{m-1,0i})2/2\pi]$	q_{mean} (lt/s/m)	Dimensionless q_{mean}	h_c (m)	R_c (m)	d_{50} (m)	ρ_s (t/m3)	σ	S (m)	A (m)	x_S (m)	x_A (m)	L_S (m)	L_A (m)	T* (s)	T_{max} (s)
S-Test-1	0.073	1.235	0.031	0.003371	0.076	0	0.09	0.00021	2.65	1.719	0.012	0.006	0.025	0.145	0.095	0.170	5390	16986
S-Test-2	0.080	1.288	0.031	0.013672	1.247	0	0.09	0.00021	2.65	1.719	0.022	0.016	0.055	0.265	0.165	0.370	4516	18920
S-Test-3	0.089	1.379	0.030	0.046438	14.386	0	0.09	0.00021	2.65	1.719	0.051	0.020	0.095	0.465	0.355	1.280	5211	24104
S-Test-4	0.120	1.596	0.031	0.409607	1119.24	0	0.09	0.00021	2.65	1.719	0.070	0.039	0.155	1.285	1.110	1.385	5619	25260
S-Test-5	0.073	1.235	0.031	0.003371	0.076	0.03	0.09	0.00021	2.65	1.719	0.018	0.010	0.005	0.175	0.105	0.335	8021	22350
S-Test-6	0.080	1.288	0.031	0.013672	1.247	0.03	0.09	0.00021	2.65	1.719	0.022	0.017	0.075	0.265	0.195	0.290	5613	23650
S-Test-7	0.081	1.286	0.032	0.013593	1.233	0.03	0.09	0.00021	2.65	1.719	0.028	0.016	0.065	0.285	0.215	0.470	6790	28304
S-Test-8	0.081	1.287	0.031	0.018511	2.286	0.03	0.09	0.00021	2.65	1.719	0.045	0.023	0.115	0.415	0.315	0.875	8142	31232
S-Test-9	0.081	1.493	0.023	0.022795	3.466	0.03	0.09	0.00021	2.65	1.719	0.046	0.018	0.105	0.425	0.315	0.710	10950	39410
S-Test-10	0.097	2.274	0.012	0.597762	2383.67	0.03	0.09	0.00021	2.65	1.719	0.090	-	0.265	-	1.455	-	8402	59241
S-Test-11	0.089	1.379	0.030	0.046438	14.386	0.03	0.09	0.00021	2.65	1.719	0.046	0.022	0.150	0.625	0.385	1.210	6148	29344
S-Test-12	0.105	1.505	0.030	0.195745	255.605	0.03	0.09	0.00021	2.65	1.719	0.061	0.020	0.195	1.405	0.635	1.830	4212	36425
S-Test-13	0.120	1.596	0.030	0.409607	1119.24	0.03	0.09	0.00021	2.65	1.719	0.060	0.023	0.205	1.915	0.875	2.310	4669	41679
S-Test-14	0.148	1.858	0.028	1.788671	21342.7	0.03	0.09	0.00021	2.65	1.719	0.098	-	0.265	-	2.125	-	4330	33660
S-Test-15	0.073	1.235	0.031	0.003371	0.076	0.06	0.09	0.00021	2.65	1.719	0.018	0.009	0.005	0.215	0.155	0.175	8351	26820
S-Test-16	0.089	1.379	0.030	0.046438	14.386	0.06	0.09	0.00021	2.65	1.719	0.041	0.014	0.135	0.685	0.365	1.090	3984	30392
S-Test-17	0.120	1.596	0.030	0.409607	1119.24	0.06	0.09	0.00021	2.65	1.719	0.080	-	0.245	-	1.375	-	5828	42942

Table 4.2 (Continuted)

S-Test-18	0.073	1.235	0.031	0.003371	0.076	0.09	0.09	0.00021	2.65	1.719	0.018	0.012	0.005	0.285	0.175	0.240	15315	52746
S-Test-19	0.089	1.379	0.030	0.046438	14.386	0.09	0.09	0.00021	2.65	1.719	0.052	0.019	0.015	0.665	0.305	0.990	5718	35632
S-Test-20	0.120	1.596	0.030	0.409607	1119.24	0.09	0.09	0.00021	2.65	1.719	0.087	0.019	0.295	1.845	0.875	2.210	5970	49257
S-Test-21	0.073	1.235	0.031	0.003371	0.003	0.03	0.09	0.00066	2.66	2.438	0.010	0.012	0.015	0.145	0.095	0.210	4499	13410
S-Test-22	0.080	1.288	0.031	0.013672	0.042	0.03	0.09	0.00066	2.66	2.438	0.019	0.020	0.045	0.235	0.165	0.300	4490	17974
S-Test-23	0.089	1.379	0.030	0.046438	0.482	0.03	0.09	0.00066	2.66	2.438	0.043	0.024	0.085	0.385	0.285	0.500	5485	27248
S-Test-24	0.120	1.596	0.030	0.409607	37.516	0.03	0.09	0.00066	2.66	2.438	0.067	-	0.215	-	0.905	-	4284	44205
S-Test-25	0.089	1.379	0.030	0.046438	0.004	0.03	0.09	0.00335	2.55	2.056	0.017	0.015	0.075	0.185	0.135	0.170	8924	24104
S-Test-26	0.120	1.596	0.030	0.409607	0.337	0.03	0.09	0.00335	2.55	2.056	0.051	0.068	0.015	0.315	0.225	0.280	1877	15156
S-Test-27	0.148	1.858	0.028	1.788671	6.421	0.03	0.09	0.00335	255	2.056	0.102	0.117	0.205	0.705	0.495	0.630	1443	21420

4.2.1 Evaluation of Scour Profiles

When all the obtained scour profiles were analyzed, it was found that they can be categorized into four different groups named GR1, GR2, GR3, and GR4. These groups are related to the dimensionless overtopping discharge value, which also contains the median grain size of the backfill materials. In the normalized scour profiles figures, z is the vertical distance, and x is the horizontal distance. The first group of rear side bed profiles, GR1, is given in Figure 4.3.

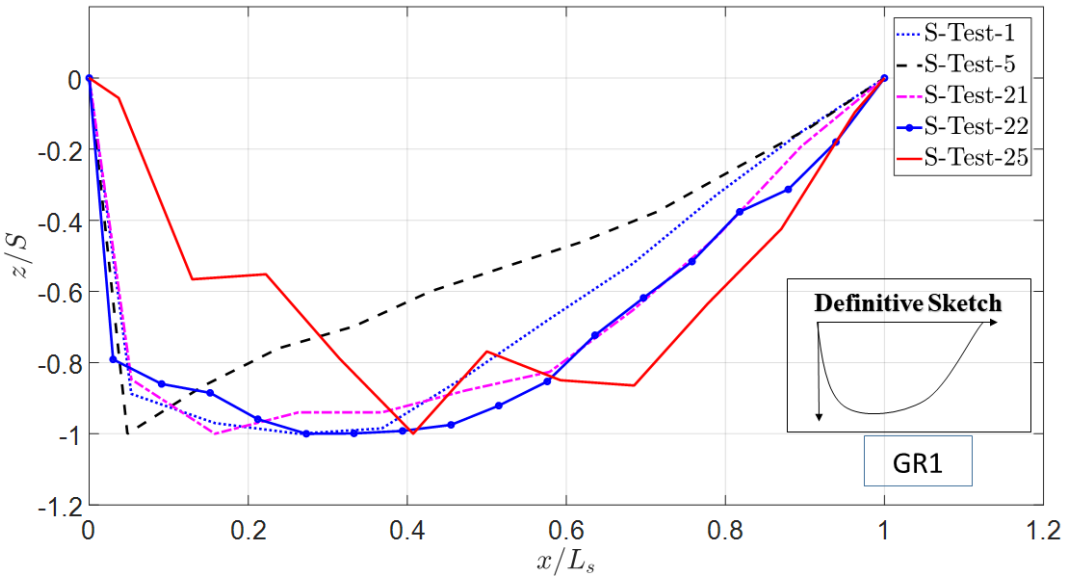

Figure 4.3. Normalized scour profiles of GR1

GR1 contains relatively weaker overtopping discharges, considering the flow-backfill material interactions. At the bottom right side of Figure 4.3, an illustrative sketch is given for the rear side bed profiles in Gr1. In this group, a single large scour hole was formed in the experiments. The conducted experiments are in the 0.00254-0.076 range of dimensionless overtopping discharge ($q_{mean}^2/[\Delta g d_{50}^3]$) value.

The second group of rear side bed profiles, GR2, is given in Figure 4.4.

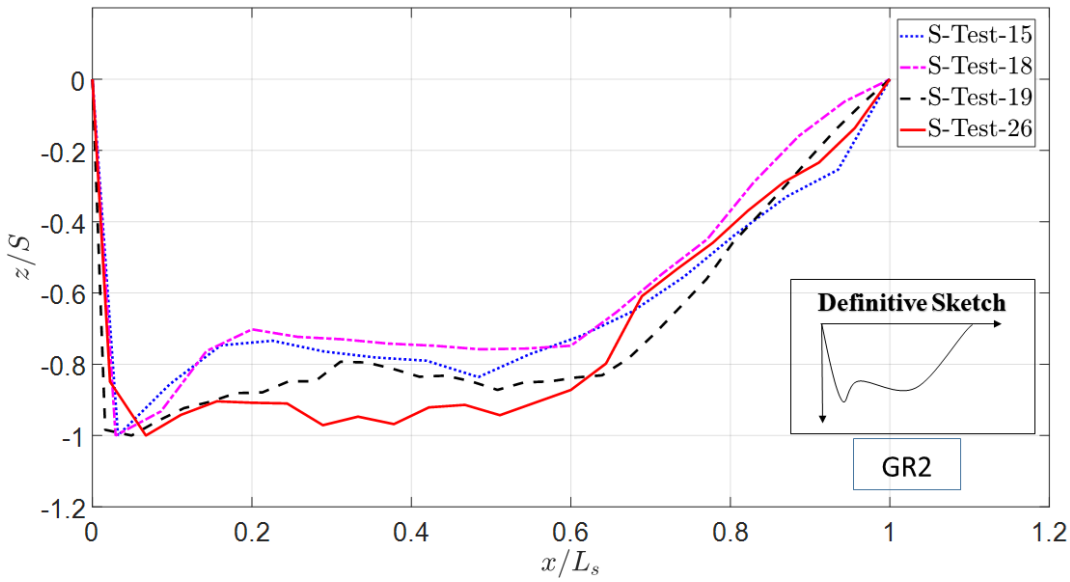

Figure 4.4. Normalized Scour Profiles of GR2

Double peak scour hole profiles, where the maximum scour depth occurred at the first peak, were grouped as GR2. The performed experiments in this group are in the 0.076-0.337 range of dimensionless overtopping discharge ($q_{mean}^2/[\Delta g d_{50}^3]$) value. Although S-Test-19 created the same scour profile defined in Figure 4.4, the dimensionless overtopping discharge value in this experiment is 14.386, which belongs to the GR3 having the range of 0.482-14.386. Considering the overtopping discharge value of S-Test-19, the scour profile defined in Gr3 was observed. However, in this test, wave pressure also caused sediment movement next to the crown wall because the backfill material thickness was limited next to the crown wall. Therefore, the sediments next to the crown wall were washed away due to observed trough pressure. In Figure 4.5, the rear side movement due to wave pressure was shown.

Figure 4.5. Rear side movement due to the wave pressure

In Figure 4.6, the third group of rear side bed profiles, GR3, is given.

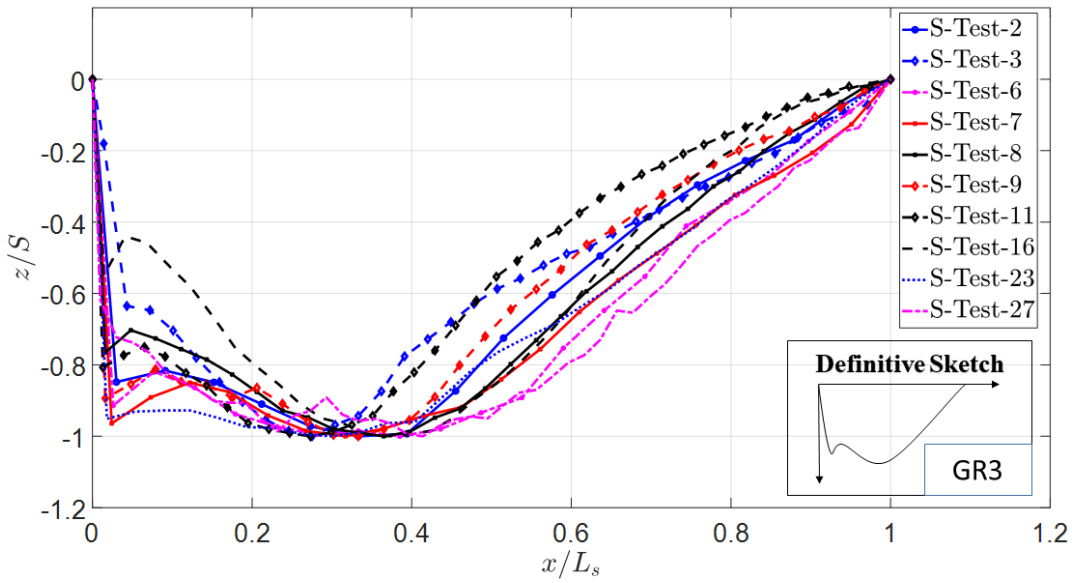

Figure 4.6. Normalized scour profiles of GR3

Double peak scour hole profiles, where the maximum scour depth occurred at the second peak, were grouped as GR3. The conducted tests are in the 0.482-14.386 range of dimensionless overtopping discharge ($q_{mean}^2/[\Delta g d_{50}^3]$) value. In S-Test-16, having $h_c/R_c = 0.66$, a scour profile that can be considered as a transition

profile from GR3 to GR4 was obtained. Although the dimensionless overtopping discharge value in this test is 14.386, scouring occurred more efficiently due to the drop height. S-Test-16 was included in GR3 because all the bed profiles in GR4 have ripple formations, and in this profile, there is no apparent ripple formations.

The fourth group of rear side bed profiles, GR4, is given in Figure 4.7.

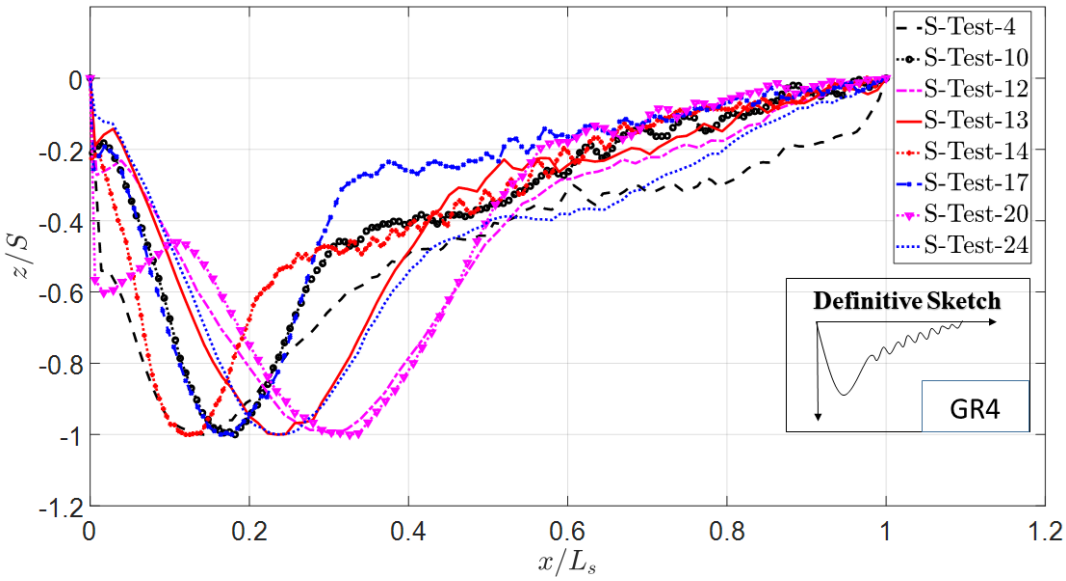

Figure 4.7. Normalized scour profiles of GR4

GR4 contains the tests that an immense amount of overtopping discharge took place. Therefore, due to insufficient water drainage through the backfill materials and the core, the rear side was flooded, and the experimental setup worked as a submerged system. In these tests, a single narrow scour hole was formed. The performed experiments are in the 37.516-21342.737 range of dimensionless overtopping discharge ($q_{mean}^2/[\Delta g d_{50}^3]$) value. Also, ripple formations (Figure 4.8) occurred between the maximum scour depth and the transition point from scour to accretion. In Figure 4.7, it can be seen that the scour hole part near the crown wall in S-Test-20 occurred relatively different than the other scour profiles. As the number of waves applied to the structure increased, the backfill area near the crown wall was approximately entirely washed away, which led to the maximum scour depth location further away from the crown wall. Like S-Test-19,

in S-Test-20, the backfill materials were carried away due to the limited amount of sediment adjacent to the crown wall, and a double peak was formed (Figure 4.5).

Figure 4.8. Seaside view of the S-Test-20 bed profile

By considering the scour hole shape as a single peak scour hole, the average of the obtained scour data was taken, and the mean normalized scour profile was shown in Figure 4.9. For each z/S values, divided into 0.05 intervals, unique z/L_S values were acquired.

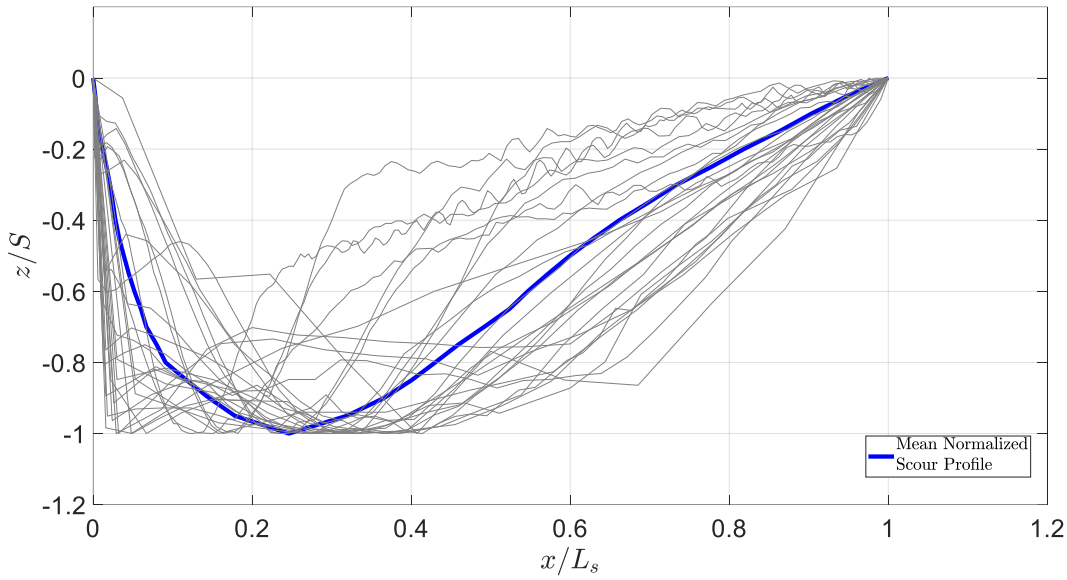

Figure 4.9. Mean normalized scour profile

4.2.2 Multiple Regression Analysis

First, relations between previously defined dependent and independent parameters were investigated by performing linear regression tests. It was found that they can not be correlated linearly. Then, the investigation was conducted logarithmically. The results of the logarithmic representation showed better agreements than linear. However, after analyzing the whole data, it was decided that the relations had to be investigated by executing multiple regression analysis. Linear and logarithmic analysis of the relation between the maximum scour depth and the independent parameters, mean overtopping discharge (q_{mean}), backfill height (h_c), and the grain size distribution of the backfill material (σ), are given in Figures 4.10 to 4.15.

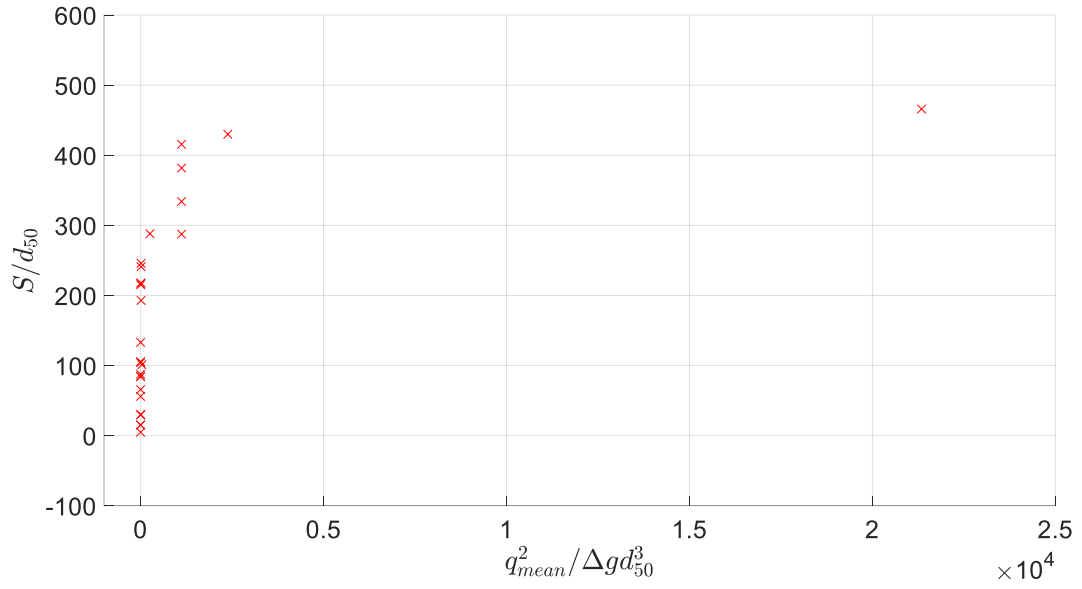

Figure 4.10. Relation between the maximum scour depth and the mean overtopping discharge in linear axes

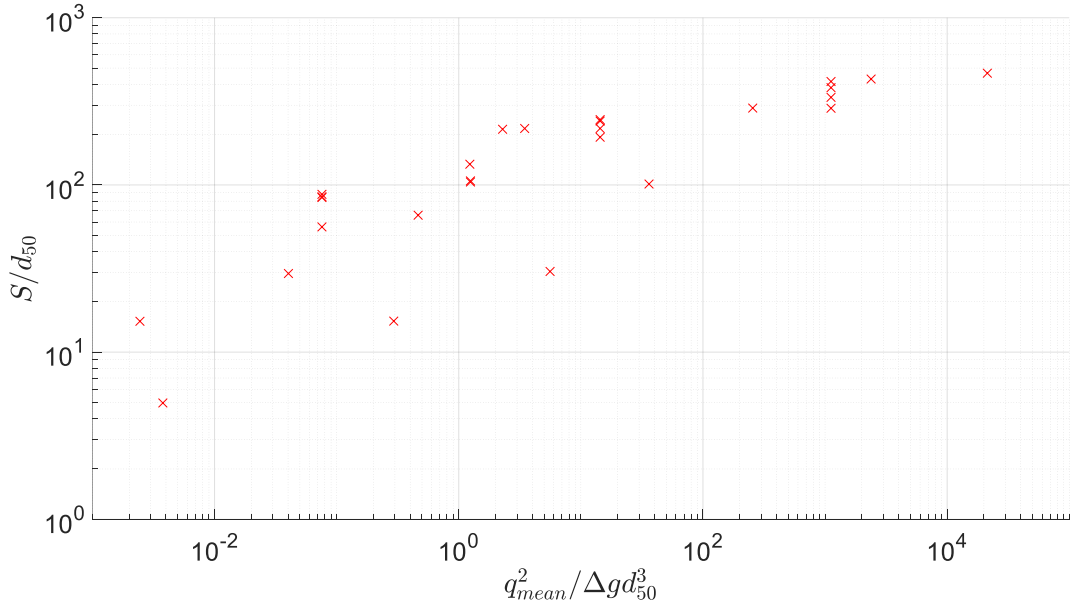

Figure 4.11. Relation between the maximum scour depth and the mean overtopping discharge in logarithmic axes

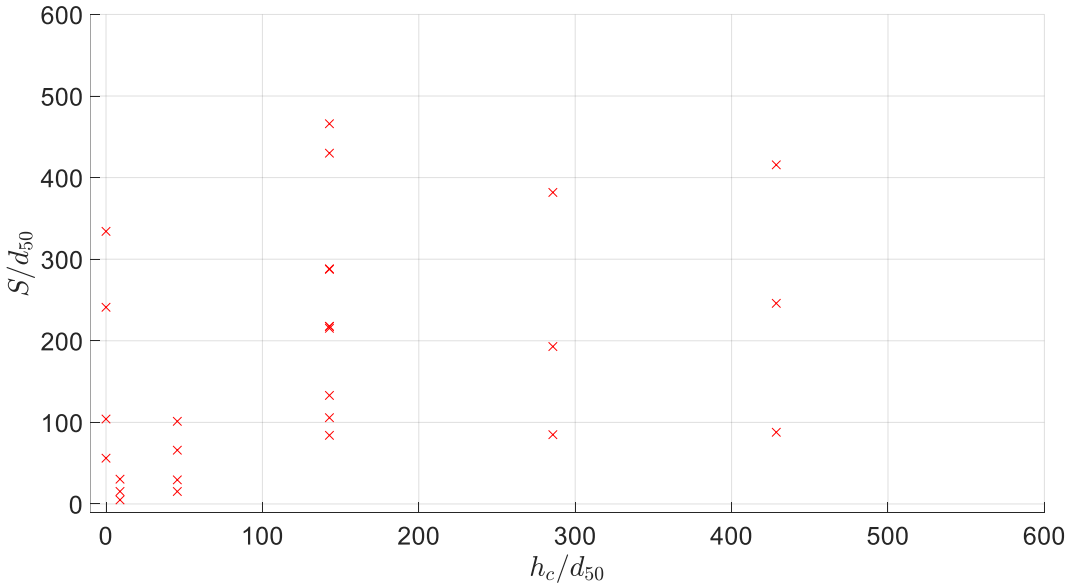

Figure 4.12. Relation between the maximum scour depth and the backfill height in linear axes

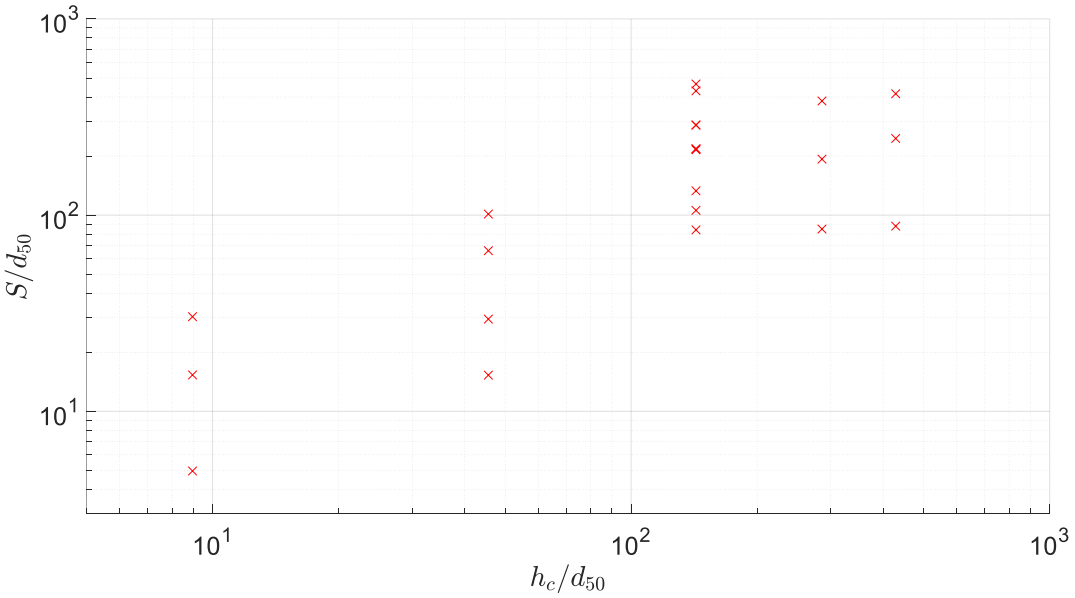

Figure 4.13. Relation between the maximum scour depth and the backfill height in logarithmic axes

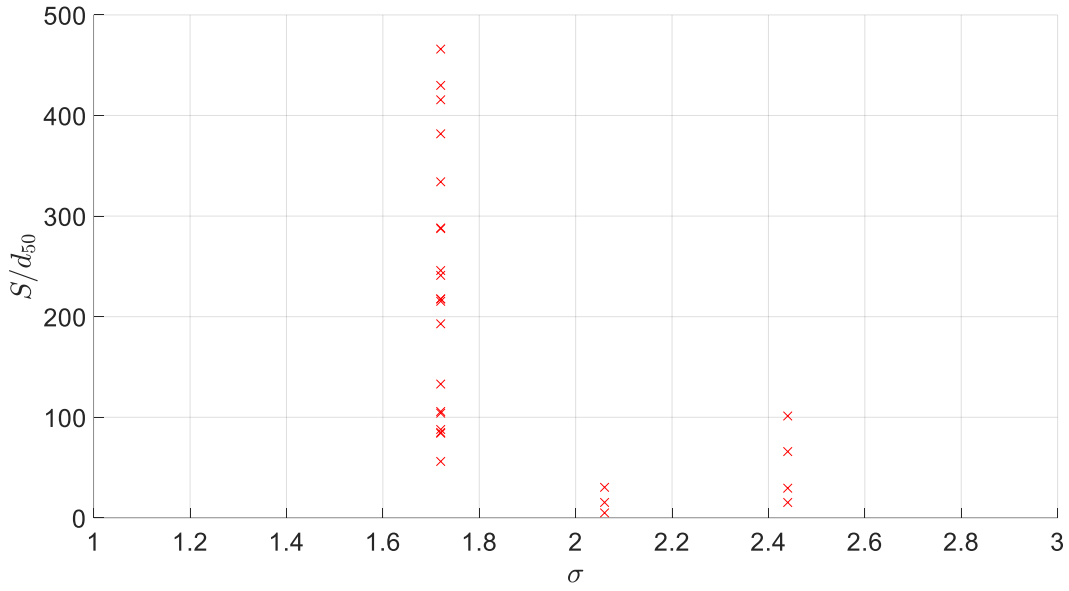

Figure 4.14. Relation between the maximum scour depth and the grain size distribution of the backfill material in linear axes

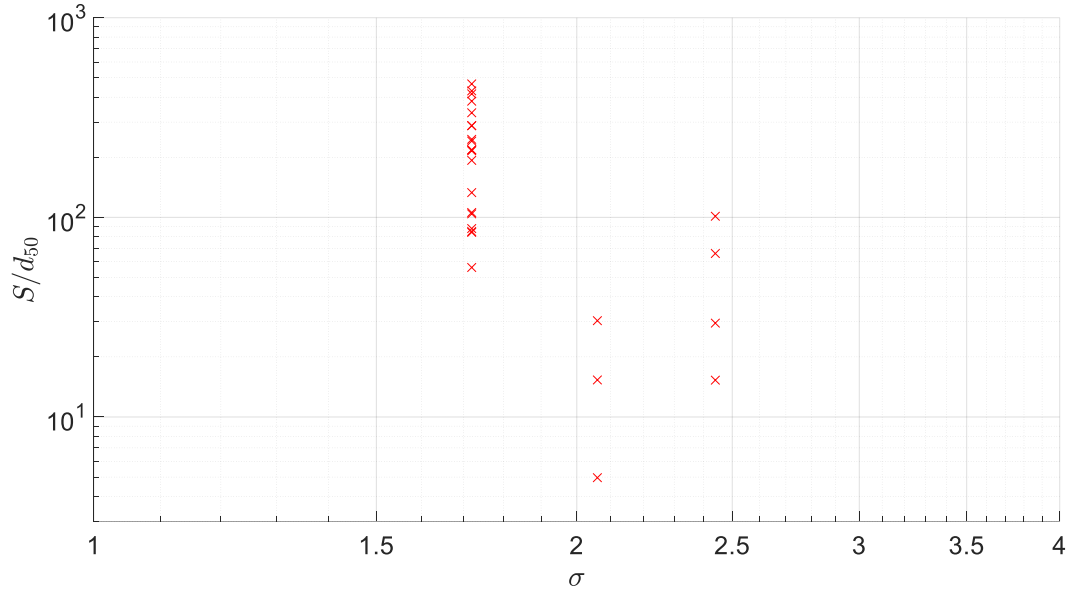

Figure 4.15. Relation between the maximum scour depth and the grain size distribution of the backfill material in logarithmic axes

When a linear fit was made between the mean overtopping discharge and maximum scour depth, the R^2 of the fit was found 0.257. Also, linear fits between the maximum

scour depth and the other two independent parameters, which are backfill height and the grain size distribution of the backfill material, resulted in with R^2 of 0.149 and 0.300, respectively. However, when logarithmic fits were performed between the maximum scour depth and the independent parameter, mean overtopping discharge, maximum scour depth, and the grain size distribution of the backfill material, the obtained values of the R^2 are 0.831, 0.357, and 0.311. Therefore, the logarithmic approach was used in the multiple regression analysis.

By taking wave series and backfill material features into account to perform multiple regression analysis, geometrical properties of the morphological changes (scour and accretion) were acquired. The overtopping discharge and backfill height, which were found the most significant parameters, were kept in the final analysis. IBM SPSS Statistics software was used to execute the analyses. In equation (4.3) given below, geometrical properties of the scour and accretion, depending on the backfill height and the mean overtopping discharge, were given. 4 out of 27 experiments have $h_c/d_{50} = 0$. Since the analysis was made logarithmically, these four experimental results were not used when the scour properties were obtained. Also, 18 out of 27 experimental results were used when the accretion properties were acquired. Because in the 4 out of 27 experiments, rear side length was not sufficient enough to obtain accretion properties. Therefore, these four experiments were excluded. The coefficients belonging to equation (4.3) were presented in Table 4.3. Table 4.3, β is the coefficient that if its value is high, the corresponding parameter impacts the dependent parameters most. In Figures 4.16 to 4.21, comparisons of the predicted and experimental results were presented. The equation (4.3) is only valid in the investigated dimensionless mean overtopping discharge range ($q_{mean}^2/[\Delta g d_{50}^3]$) of 0.00254 to 21342.737.

$$y = A\left(\frac{q_{mean}^2}{\Delta g d_{50}^3}\right)^B \left(\frac{h_c}{d_{50}}\right)^C \tag{4.3}$$

Table 4.3. Multiple regression results regarding the geometrical features

y	A		B			C		
	Unstandardized Coefficients		Unstandardized Coefficients		Standardizied Coefficients	Unstandardized Coefficients		Standardizied Coefficients
	Coefficient	Standard Error	Coefficient	Standard Error	β	Coefficient	Standard Error	β
S/d_{50}	6.184	0.275	0.171	0.016	0.614	0.563	0.06	0.546
A/d_{50}	10.125	0.378	0.113	0.027	0.523	0.341	0.081	0.532
x_s/d_{50}	31.785	0.877	0.294	0.051	0.748	0.281	0.19	0.193
x_A/d_{50}	41.804	0.282	0.218	0.020	0.560	0.695	0.060	0.604
L_s/d_{50}	40.005	0.312	0.222	0.018	0.663	0.616	0.068	0.497
L_A/d_{50}	38.745	0.488	0.224	0.035	0.524	0.767	0.104	0.606

From Table 4.3, it can be seen that if the mean overtopping discharge (q_{mean}) increases, the geometrical properties of the scour, which are maximum scour depth (S), maximum accretion height (A), maximum scour depth distance to the crown wall (x_S), maximum accretion height distance to the crown wall (x_A), scour hole width in wave direction (L_S), and accretion width in wave direction (L_A), increase. Similarly, if the backfill height (h_c) increases, the geometrical properties of the scour increase.

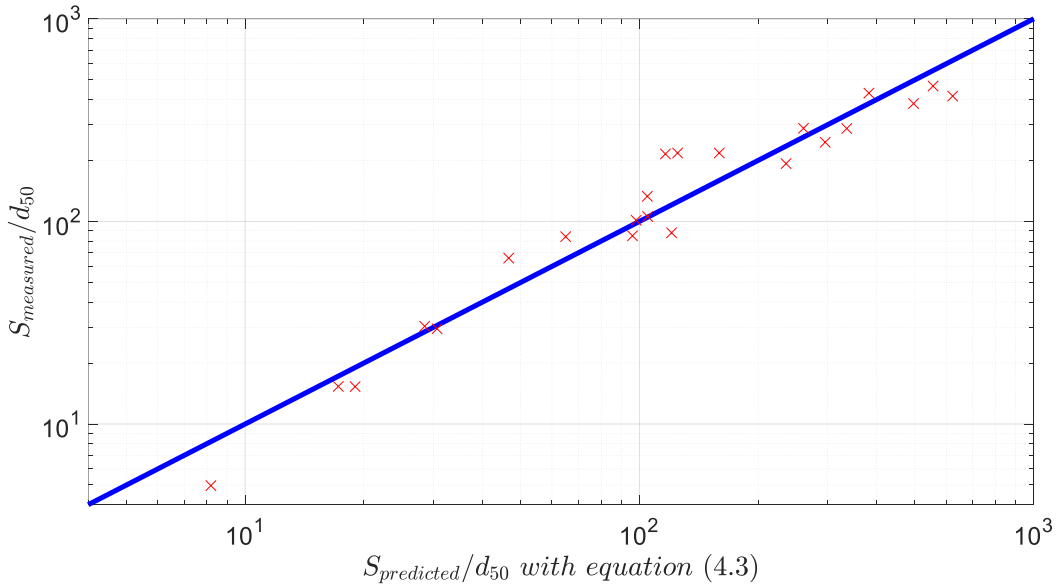

Figure 4.16. Measured and predicted results of the maximum scour depth

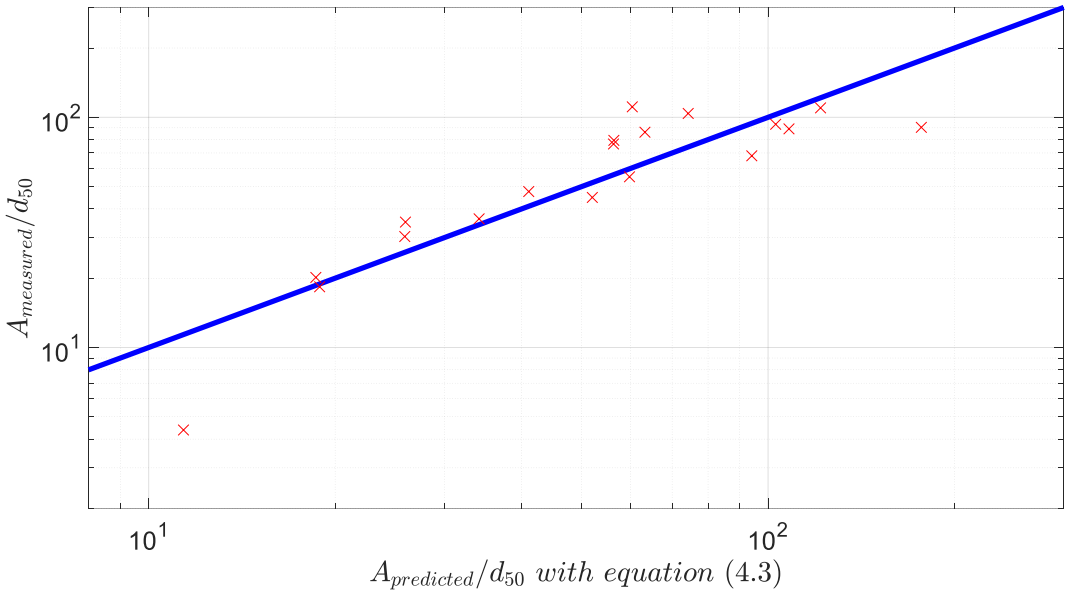

Figure 4.17. Measured and predicted results of the maximum accretion height

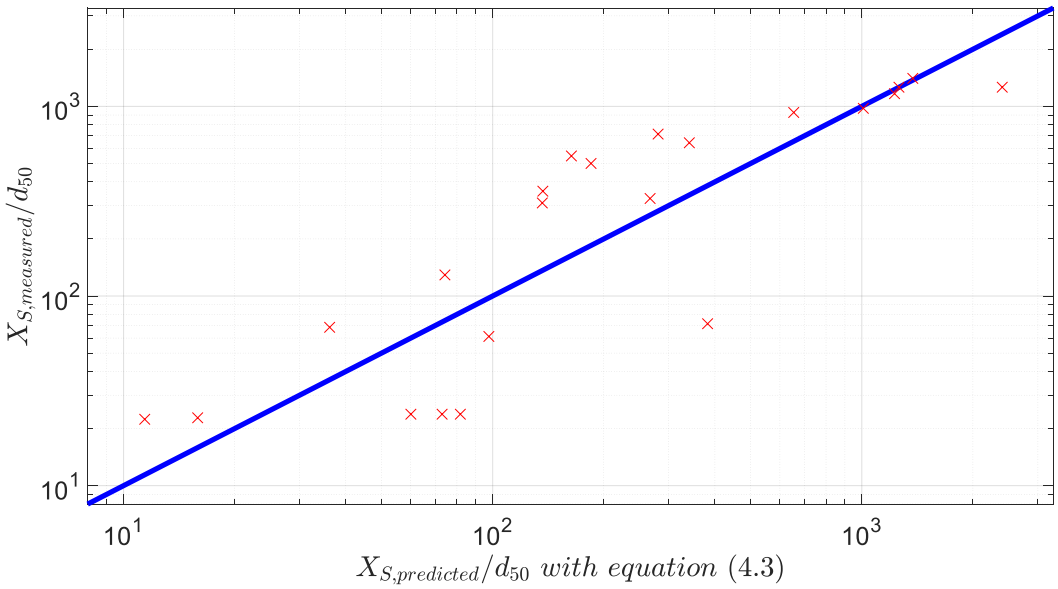

Figure 4.18. Measured and predicted results of the maximum scour depth distances to the crown wall

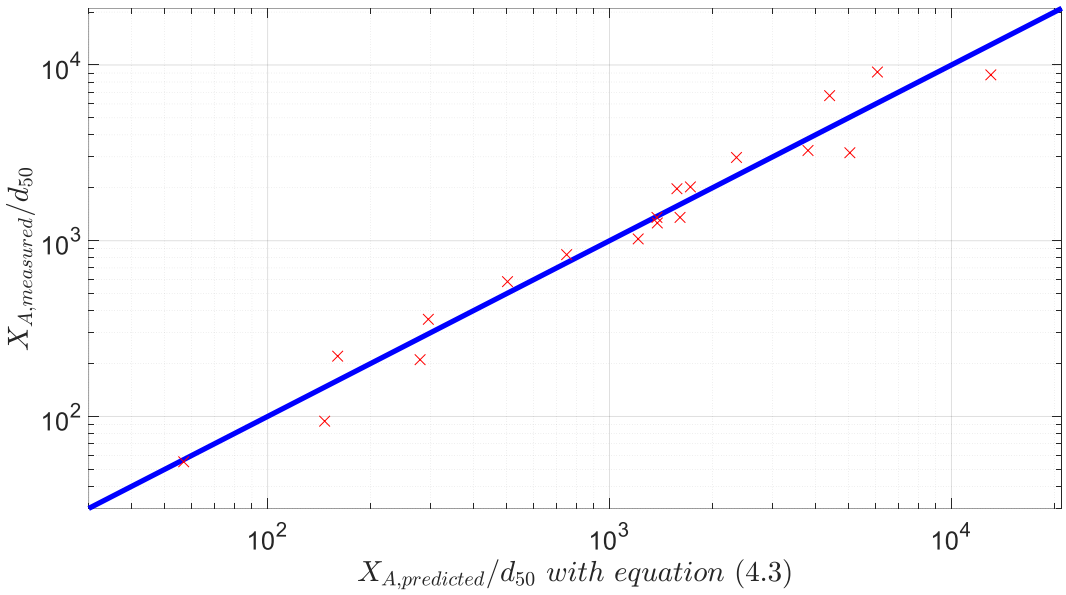

Figure 4.19. Measured and predicted results of the maximum accretion height distances to the crown wall

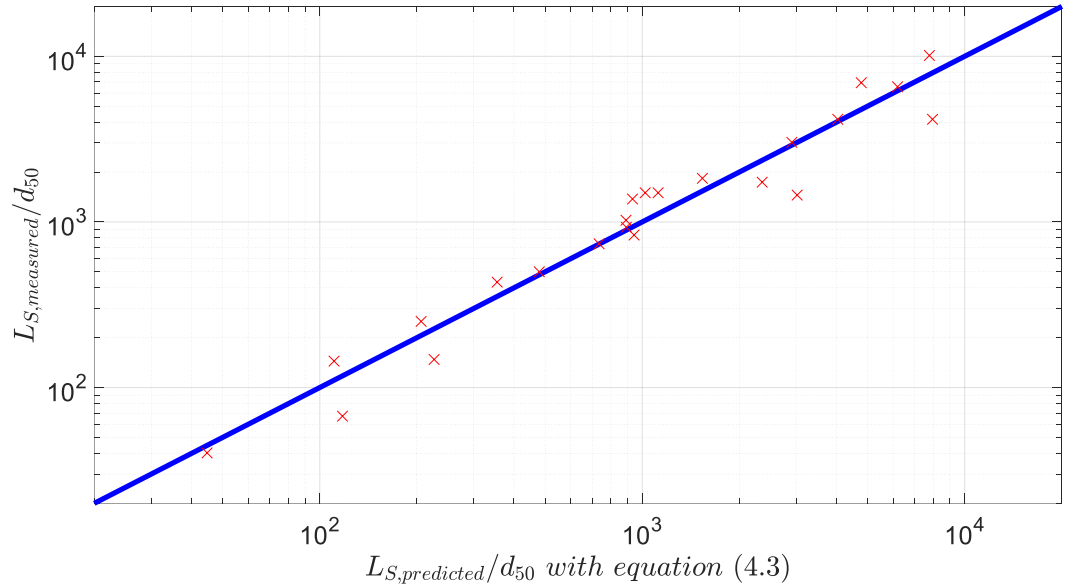

Figure 4.20. Measured and predicted results of the scour hole width in wave direction

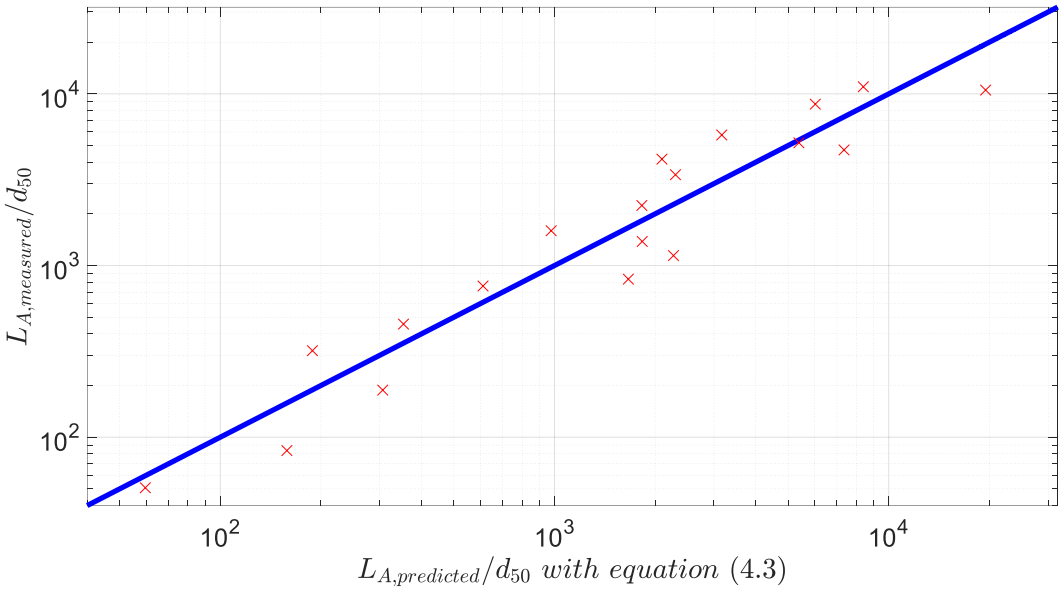

Figure 4.21. Measured and predicted results of the accretion width in wave direction

4.2.3 Time Scale

In the previously given equation (3.5), scour depth development in time was given. The experimental results and the formula was compared, and they were found in good agreement (correlation coefficient, $r = 0.944$, ($R^2 = 0.891$)). In addition, a new equation (using the same format with equation (3.5)) was generated, covering the same issues which are $S_t/S = 0$ at $t/T^* = 0$ and S_t/S is not higher than one.

$$S_t = S[1 - \exp(-0.9364 * t/T^*)] \quad (4.4)$$

The experimental results and the equation (4.4) was compared, and they were found in good agreement (correlation coefficient, $r = 0.948$, ($R^2 = 0.899$)). In Figure 4.22, the experimental data, equation (3.5), and equation (4.4) were plotted.

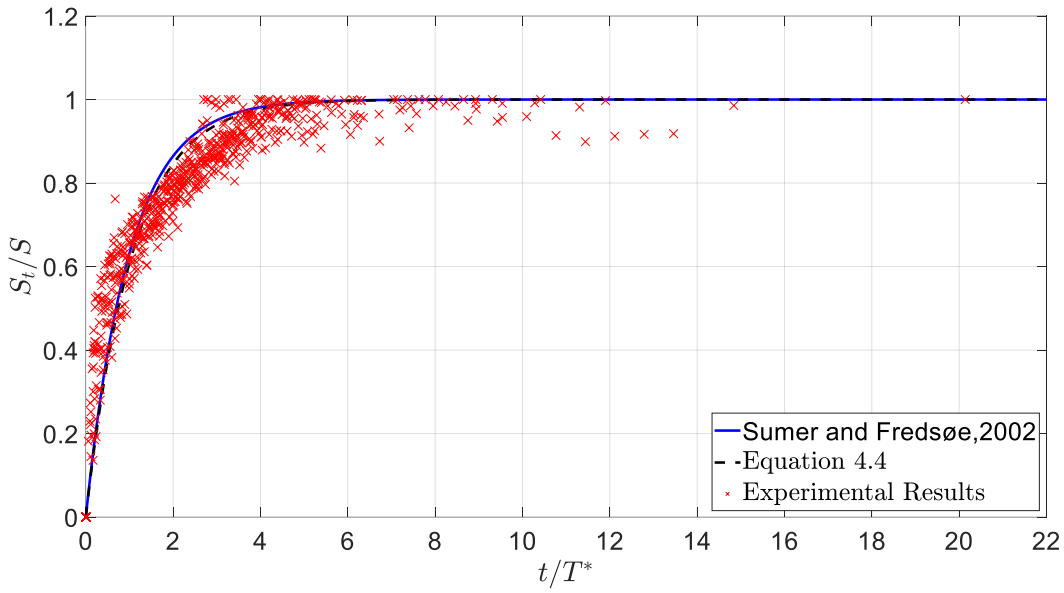

Figure 4.22. Scour development in time

Multiple regression analyses also were performed to acquire the time scale of the scour and the time required to observe maximum scour depth. Equation (4.3) was used to obtain coefficients, and the results were presented in Table 4.4. In the analyses, the obtained β coefficient corresponding to the overtopping discharge for the time scale was significantly lower than the β coefficient corresponding to the backfill height. Therefore, the overtopping discharge parameter was excluded from the equation to predict the time scale. In Figures 4.23 and 4.24, comparisons of the predicted and measured results were given.

Table 4.4. Multiple regression results regarding the time related features

y	A		B			C		
	Unstandardized Coefficients		Unstandardized Coefficients		Standardizied Coefficients	Unstandardized Coefficients		Standardizied Coefficients
	Coefficient	Standard Error	Coefficient	Standard Error	β	Coefficient	Standard Error	β
$T^*\sqrt{g/d_{50}}$	48098.198	0.416	0.000	0.000	-	0.634	0.087	0.846
$T_{max}\sqrt{g/d_{50}}$	469770.708	0.248	0.053	0.015	0.305	0.502	0.054	0.775

Table 4.4 shows the time scale of the scour (T^*) is only dependent on backfill height (h_c). Also, if the backfill height (h_c) rises, the time scale of the scour (T^*) rises. Unlike the time scale of the scour (T^*), the time required to observe maximum scour depth (T_{max}) are dependent on both mean overtopping discharge (q_{mean}) and backfill height (h_c). If mean overtopping discharge (q_{mean}) and backfill height (h_c) increase, the time required to observe maximum scour depth (T_{max}) increases.

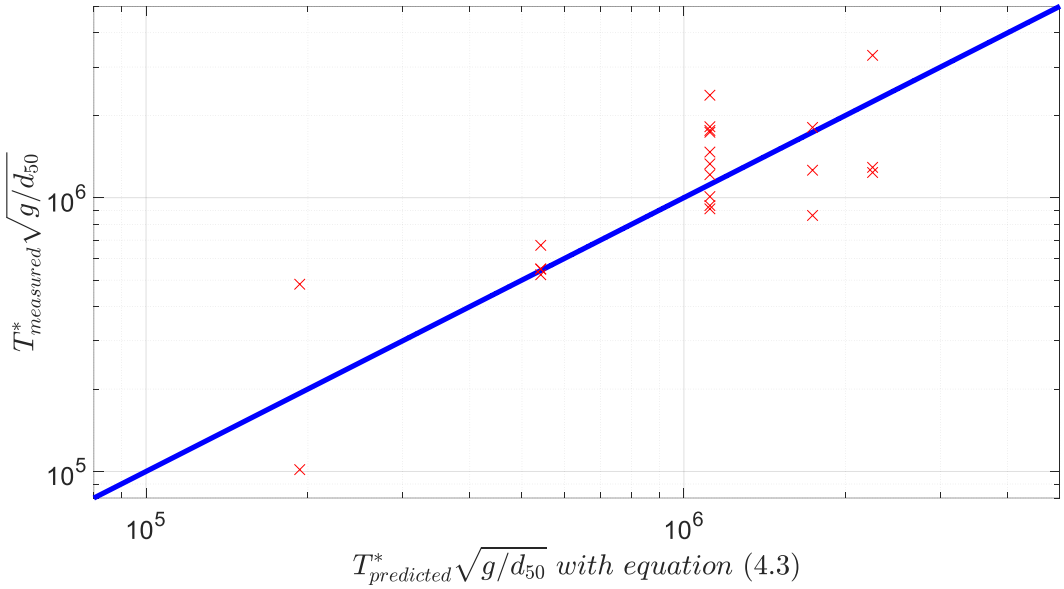

Figure 4.23. Measured and predicted results of the time scale of the scour

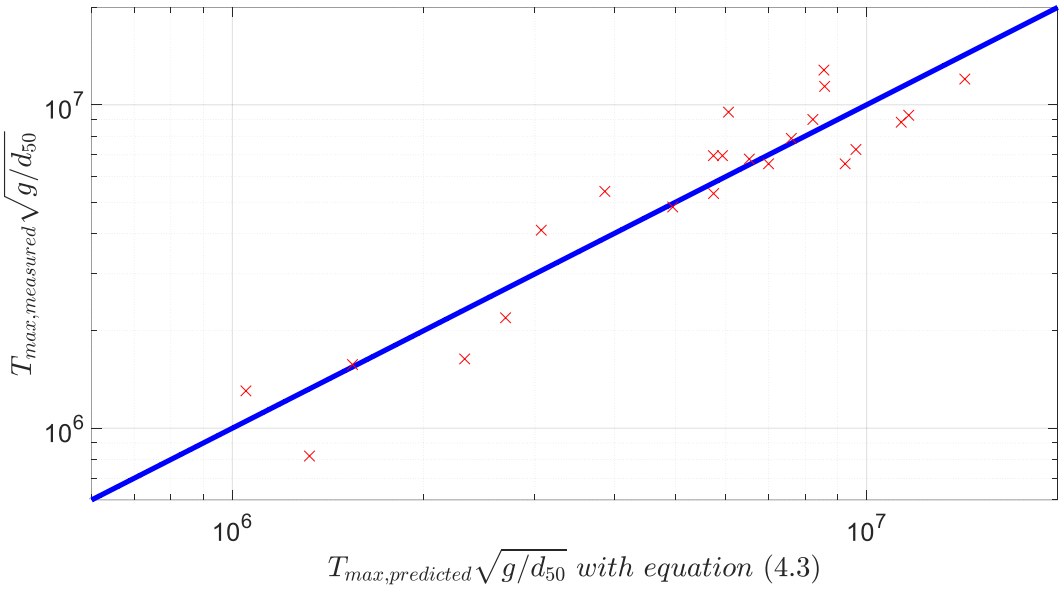

Figure 4.24. Measured and predicted results of the time needed to observe maximum scour depth

CHAPTER 5

DISCUSSION

First of all, when the morphological changes behind the rubble mound revetment were obtained, two-dimensional scanning was performed instead of three-dimensional scanning because the backfill profiles in the scour tests were close to the two-dimensional profile. When the changes were obtained, seven lines (Figure 3.10) were measured. The obtained maximum and minimum values of the maximum scour depth (S) from the seven lines corresponding to each scour test were compared by taking the ratio of their relative differences. The ratio of their relative differences was calculated as $((S_{max,measured} - S_{min,measured})/S_{max,measured})$, which $S_{max,measured}$ and $S_{min,measured}$ are the obtained maximum and minimum values of the maximum scour depth (S), respectively. The mean of the ratios was found as 0.234. However, in some tests (S-Test-1, S-Test-16, and S-Test-25) having small dimensionless mean overtopping discharge (0.076, 0.076, and 0.004, respectively), the difference was found higher (0.537, 0.456, and 0.644, respectively). Especially in S-Test-25, the measured maximum scour depth (S) was 17 mm, and the median grain size of the backfill material (d_{50}) was 3.35 mm. In this test, the measured maximum scour depth (S) was slightly more than five times the median grain size of the backfill material (d_{50}). The higher differences between the obtained maximum and minimum values of the maximum scour depth (S) from the seven lines corresponding to each scour test resulted from the relatively weaker flows by considering the flow-backfill material interactions. Therefore, the morphological changes at the rear side of the structure were less uniform. However, when all conducted scour experiments were considered, the backfill profile representation as two-dimensional was agreeable.

Another significant matter was to provide a similar hydrodynamic phase of sediment transport between the model and the prototype of the rubble mound revetment and its rear side. For sediment transport similarity requirements, Kamphuis (1985 and 1991) defines five dimensionless properties: grain size Reynolds number (R_*), the densimetric Froude number (F_*), the relative density of the sediment (S_s), relative length (l_s), and the relative fall velocity (V_w). For a perfectly modeled study, these properties must be equal in both model and prototype. Unfortunately, providing all these equalities is not possible (Hughes, 1993). These dimensionless properties are presented in equation 5.1

$$\prod_S' = g'\left(\begin{matrix} R_* = \frac{v_* d_{50}}{\vartheta}, F_* = \frac{\rho_w v_*^2}{g(\rho_s/\rho_w - 1)d_{50}}, \\ S_s = \frac{\rho_s}{\rho_w}, l_s = \frac{a_m}{d_{50}}, V_w = \frac{w_s}{v_*} \end{matrix}\right) \tag{5.1}$$

in which $v_* = \sqrt{\tau/\rho_w}$ is the bed shear velocity (m/s), τ is the bed shear stress on the backfill surface (Pa), ρ_w is the density of the water (kg/m^3), d_{50} is the median grain size of the backfill material (m), g is the gravitational acceleration, ρ_s is the density of the sediment (kg/m^3), a_m is the average wave amplitude (m), w_s is the fall velocity of the backfill material (m/s).

In this study, the densimetric Froude number (F_*) and the relative density of the sediment (S_s) were kept the same in both model and prototype. Grain size Reynolds number (R_*) is not similar in both prototype and model. When the grain size Reynolds number (R_*) similarity is not provided, viscous forces affect the sediment transport processes. However, Kamphuis (1975 and 1985) pointed out that models with the densimetric Froude number (F_*) and relative density criterion (S_s) are affected minimally by the viscous forces. For the relative length criterion (l_s), considering the wave runup height and the distance the overtopping discharge takes to hit the rear side should be equal in both model and prototype. However, in EurOtop (2018), it was stated that the small-scale model tests with the small overtopping discharge could be affected by the wind and viscosity forces (surface roughness of the armor units). Therefore, the field measurements and laboratory experiments

could show different wave run-up and overtopping discharges. For the viscosity impact, a critical wave Reynolds number ($Re_{w,cr} = ch/\vartheta = 1000$), in which c is the wave celerity, h is the water depth, and ϑ is the kinematic viscosity, was defined in EurOtop (2018). This critical number was given for all the wave processes: propagation, breaking, run-up, and overtopping. In all conducted experiments, the wave Reynolds number (Re_w) was higher than the critical wave Reynolds number. Thus, the relative length criterion (l_s) was provided in the model. The backfill material was modeled in the conducted scour tests by using the length scale ($d_{50,m} = d_{50,p} * \lambda_L$, in which λ_L is the length scale of the model). The subindexes m and p represent model and prototype, respectively. The corresponding fall velocities (w_s) was calculated by using the equations (5.2 and 5.3) given by Soulsby (1998) was used.

$$w_s = \frac{\vartheta}{d_{50}}\left[(10.36^2 + 1.049D_*^3)^{1/2} - 10.36\right] \tag{5.2}$$

$$D_* = \left[\frac{g(\rho_s/\rho_w - 1)}{\vartheta^2}\right]^{1/3} d_{50} \tag{5.3}$$

In the equations (5.2 and 5.3), ϑ is the kinematic viscosity of the water (m^2/s) and D_* is the dimensionless grain size. The equation (5.2) is valid for all dimensionless grain size (D_*).

When the fall velocities of the backfill materials both in model and prototype were calculated for $d_{50,m} = 0.21, 0.66$, and $3.35\ mm$ and $d_{50,p} = 7.6, 23.8$, and $120.6\ mm$, $w_{s,m} = 0.028, 0.092$, and $0.228\ m/s$ and , $w_{s,p} = 0.357, 0.637$, and $1.387\ m/s$ was calculated. The ratio of fall velocities of the model and prototype is equal to $w_{s,m}/w_{s,p} = \lambda_T = 0.167$, in which λ_T is the time scale of the model, if the model satisfies the relative fall velocity criterion (V_w). The ratios were calculated as $w_{s,m}/w_{s,p} = 0.079, 0.144$ and 0.165. From the ratios, it can be said that the relative fall velocity similarity criterion was not satisfied in the experiments conducted with $d_{50,m} = 0.21, 0.66\ mm$ while the coarser backfill material $d_{50,m} = 3.35\ mm$ satisfied. The majority of the scour tests (24 out of 27) were performed with the backfill material having the median grain size of 0.21 mm and 0.66 mm. These

materials represent gravel in the prototype. Another backfill material having a median grain size of 3.35 mm represents small boulders in the prototype. Since the backfill materials used in the experiments $d_{50,m} = 0.21, 0.66\ mm$ had smaller fall velocities, suspended sediment transport was more effective in the experiments. Therefore, it can be assumed that lower sediment transport would occur in the prototype compared to the model. Thus, smaller scour properties such as maximum scour depth (S) are expected to occur in the prototype.

Another significant property of the wave series used in the analysis was mean overtopping discharge (q_{mean}). Due to the difficulties of measuring the overtopping discharge, time series of the overtopping discharge was not obtained, and mean overtopping discharge was used in the analyses. In the scope of this study, how the individual overtopping discharges change the rear of the structure was not studied.

A practical application of this study will be discussed. In Figure 3.1, the typical cross-section of a rubble mound revetment is given. Considering the coasts of Turkey, a design wave height of $H_{m0i} = 6.00\ m$, and spectral wave height, $T_{m-10,i} = 9.80$, (wave steepness, 0.040) in front of the structure could be assumed. The rear side of the revetments is generally considered for recreational areas. Therefore, the crest height of the revetments is not designed too high. In this case, the crest height, $R_c = 5.00\ m$ is selected. In equation 4.1, the prediction of mean overtopping discharge per width is shown. By using this equation, the mean overtopping discharge per width is found $q_{mean} = 0.050\ m^3/s/m$. It is assumed that the cross-section was designed to be statically safe by considering the given storm as a design wave. For the rear side design, assume that the backfill height is selected as $h_c = 2\ m$ and the stones used to fill the rear side of the structures had 0-100 kg. However, the storm could hit the area before the construction phase was completed. For construction purposes, the rear side of the structure could be filled with coarse gravel to provide working space and prevent problems such as mud. In this case, the storm will be expected to create morphological changes rear side of the revetment. Assuming the median grain size of the backfill material (d_{50}) as 0.020 m,

the dimensionless overtopping discharge ($q_{mean}^2/[\Delta g d_{50}^3]$) is calculated as 19.4495 (the studied range 0.00254 to 21342.737). Since the structure was assumed to be in the construction phase, the backfill height would not be at the designed level as $h_c = 2\ m$. Therefore, it could be much higher, and for this example, it was taken as $h_c = 4\ m$. The conducted experiments are in the range of 26.567 to 704.762 dimensionless significant incident wave height (H_{m0i}/d_{50}) and 26.866 to 428.571 dimensionless crest height (R_c/d_{50}). This case had a dimensionless significant incident wave height of 300 and dimensionless crest height of 200. When the generated equation 4.3 was used by considering the defined conditions, the expected maximum scour depth (S) was calculated as 4.057 m. Also, the width of the scour hole (L_S) was predicted as 40.431 m. The time scale of the scour (T^*) in this case, was predicted as almost 18 hours. Also, the time required to observe maximum scour depth (T_{max}) was calculated approximately 99 hours. Considering the average storm duration observed on the coasts of Turkey, which are 10 to 12 hours, an equilibrium state may not be observed. However, a significant could occur. By using the equation (3.4) given by Sumer and Fredsøe (2002), the scour depth (S_t) is found 1.905 m (47 % of the maximum scour). These calculations can be extended into a case where the construction phase of the revetment was completed, and the defined storm hit the area. However, in the scope of this study, the primary focus of the study is to investigate structures, which are in the construction process or their rear side was filled with noncohesive erodible backfill materials. Thus, predicting the morphological changes in the rear side of a revetment whose rear side was filled with coarse materials such as boulders requires more experiments with coarser materials.

Another issue is that although three different backfill materials were used in the physical model experiments, the number of conducted tests corresponding to each backfill material was not the same. In order to provide data homogeneity, the experiments performed with the same backfill height (h_c) and crest height (R_c) were used (a total number of 17 scour tests), and a new maximum scour depth formula was obtained depending on mean overtopping discharge (q_{mean}) only. Then, a total number of 9 experiments (each backfill material was used in 3 of the tests) having

the same backfill height (h_c) and crest height (R_c) were used, and another maximum scour depth formula was generated. The format of the generated equations is given in equation (5.4) below.

$$\frac{S}{d_{50}} = A\left(\frac{q_{mean}^2}{\Delta g d_{50}^3}\right)^B \tag{5.4}$$

For the equation generated with 17 tests, A and B were 65.497 and 0.244, respectively. Also, the other equation obtained with 9 tests has A as 40.165 and B as 0.275. When the maximum scour depth (S) was calculated by using equation (5.4), obtained by 17 and 9 tests, for the case defined in this chapter, it was found 2.702 and 1.817 m, respectively. Comparing these results to the maximum scour depth obtained by equation (4.3) could not be accurate because the impact of backfill height was not included in equation (5.4). However, for the homogeneity issue, comparing them to each other would be more sensible. The ratio of these maximum scour depth predictions is $1.817/2.702 = 0.672$. When previously discussed relative fall velocity criterion is taken into account, it can be said that the generated equations (4.3) for the scour and accretion properties could give higher results due to the majority of the conducted experiments performed with small size backfill materials.

CHAPTER 6

CONCLUSION

In this chapter, the main findings of the study are presented. First, one of the primary research questions of this study is to find out if there is an equilibrium state of the scour depth. It was found that when the storm duration increases for a particular experimental condition (same overtopping discharge), an equilibrium scour depth occurs. In addition, under the same rear side conditions (median grain size of the sediment and backfill height), the equilibrium scour depth takes place deeper as the mean overtopping discharge increases. Also, changing the backfill height considerably influences the morphological changes (scour and accretion), creating deeper scour holes and accretion heights, under the same flow condition.

When the whole scour profiles are investigated, it was found that a single large scour hole can be accepted as the first type of scour profile. This profile occurs in weaker flows. When the overtopping discharge, which is the governing parameter for the scouring process, increases, the trend of the scour hole profile turns into a double peak scour hole. In the second type of scour profile, maximum scour depth is observed at the first peak. As the overtopping discharge in the experiments increases, the third type of scour profile, having the maximum scour depth at the second peak, was observed. The final form of the scour profile observed in the experiments which have relatively stronger flows. The profile is a single narrow scour hole having ripple formations beyond the maximum scour depth location. Also, a mean scour profile was presented.

Investigation of the relations between the dependent and independent parameters was executed. IBM SPSS Statistics software was used during the investigation. Each of these independent parameters significance on the dependent parameters was determined (β coefficient). It was found that the overtopping discharge and backfill

height are the most significant parameters. Using these parameters, dimensionless relations were given for the geometrical features of the scour and accretion. Also, the time required to observe maximum scour depth was obtained with the same procedure. However, the time scale of the scour was acquired by using only the backfill height because the β coefficient belonging to the overtopping discharge was found negative value, which represents that the impact of the overtopping discharge value on the time scale of the scour is insignificant.

Three different irregular wave series sharing the same incident spectral significant wave height and period were tested. These three series created three different mean overtopping discharges. When they were used in the scour tests, it was found that three different scour profiles occurred because each series created different amounts of overtopping discharges.

The approach given by Sumer and Fredøe (2002) to define scour development in time was compared to the obtained experimental, and it was found that equation (3.5) represents the scour development very well.

In the planned experiments, the geometrical features of the revetment remained the same. Therefore, in future studies, the impact of the front slope of the structure, crest height, and width can be studied. Also, increasing the number of different backfill materials, especially coarse ones, can raise the assessment. Also, the influence of the grain size distribution of the sediment used in the backfill area should be examined. In addition, the porosity impact (both backfill sediment and structure) can be investigated.

Another future study could be investigating the previously discussed individual overtopping discharge impacts on the evolution of the rear side change. Also, using different wave series creating the same amount of overtopping discharge (q_{mean}) could be tested in the scour experiments having the same geometrical properties (such as the same crest height, backfill height, and backfill materials).

REFERENCES

Bomers, A., Aguilar Lopez, J. P., Warmink, J. J., & Hulscher, S. J. M. H. (2018). Modelling effects of an asphalt road at a dike crest on dike cover erosion onset during wave overtopping. *Natural Hazards*, *93*(1), 1–30. https://doi.org/10.1007/s11069-018-3287-y

Bormann, N. E., & Julien, P. Y. (1991). Scour downstream of grade-control structures. *Journal of Hydraulic Engineering*, *117*(5), 579–594. https://doi.org/10.1061/(ASCE)0733-9429(1991)117:5(579)

Bricker, J. D., Francis, M., & Nakayama, A. (2012). Scour depths near coastal structures due to the 2011 Tohoku Tsunami. *Journal of Hydraulic Research*, *50*(6), 637–641. https://doi.org/10.1080/00221686.2012.721015

Burcharth, H.F., Liu, Z. , Troch, P. (1999). *"Scaling of core material in rubble mound breakwater model tests",COPEDEC V*. Cape Town, South Africa.

Chatterjee, S. S., Ghosh, S. N., & Chatterjee, M. (1994). Local scour due to submerged horizontal jet. *Journal of Hydraulic Engineering*, *120*(8), 973–992. https://doi.org/10.1061/(ASCE)0733-9429(1994)120:8(973)

Chen, Z., Shao, X., & Zhang, J. (2005). Experimental study on the upstream water level rise and downstream scour length of a submerged dam. *Journal of Hydraulic Research*, *43*(6), 703–709. https://doi.org/10.1080/00221680509500390

Dehghani, A. A., Bashiri, H., & Shahmirzadi, M. E. M. (2010). Local scouring due to flow jet at downstream of rectangular sharp-crested weirs. *Proceedings of the 5th Iasme/Wseas Int Conf on Water Resources, Hydraulics & Hydrology/Proceedings of the 4th Iasme/Wseas Int Conf on Geology and Seismology*, 127–131.

Dey, S., & Raikar, R. V. (2007). Scour below a high vertical drop. *Journal of Hydraulic Engineering*, *133*(5), 564–568. https://doi.org/10.1061/(asce)0733-9429(2007)133:5(564)

Emiroglu, M. E., & Tuna, M. C. (2011). The effect of tailwater depth on the local scour downstream of stepped-chutes. *KSCE Journal of Civil Engineering*, *15*(5), 907–915. https://doi.org/10.1007/s12205-011-0921-6

EurOtop. 2018. *Manual on wave overtopping of sea defences and related structures. An overtopping manual largely based on European research, but worldwide application. 2nd ed*. http://www.overtopping-manual.com.

Farhoudi, J., & Smith, K. V. H. (1985). Local scour profiles downstream of a hydraulic jump. *Journal of Hydraulic Research*, *23*(4), 343–358. https://doi.org/10.1080/00221688509499344

Fuhrman, D. R., Baykal, C., Mutlu Sumer, B., Jacobsen, N. G., & Fredsøe, J. (2014). Numerical simulation of wave-induced scour and backfilling processes beneath submarine pipelines. *Coastal Engineering*, *94*, 10–22. https://doi.org/10.1016/j.coastaleng.2014.08.009

Ghodsian, M., Melville, B., & Coleman, S. (2012). Local scour due to sediment-carrying free-overfall water jet. *Proceedings of the Institution of Civil Engineers - Water Management*, *165*(1), 21–29. https://doi.org/10.1680/wama.2012.165.1.21

Guan, D., Melville, B., & Friedrich, H. (2016). Local scour at submerged weirs in sand-bed channels. *Journal of Hydraulic Research*, *54*(2), 172–184. https://doi.org/10.1080/00221686.2015.1132275

Hudson, R. Y., Hermann, F. A., Sager, R. A., Whalin, R. W., Keulegan, G. H., Chatnam, C. E., & Hales, L. Z. (1979). Coastal hydraulic models. Special Report No: 5 *US Army Engineer Waterways Experiment Station, Vicksburg, Missisippi.*

Hughes, S. A. (1993). *Physical Models and Laboratory Techniques in Coastal Engineering*. https://doi.org/10.1142/2154

Jayaratne, M. P. R., Premaratne, B., Adewale, A., Mikami, T., Matsuba, S., Shibayama, T., Esteban, M., Nistor, I. (2016). Failure mechanisms and local scour at coastal structures induced by Tsunami. *Coastal Engineering Journal*, *58*(4), 3–4. https://doi.org/10.1142/S0578563416400179

Jayaratne, R., Abimola, A., Mikami, T., Matsuba, S., Esteban, M., & Shibayama, T. (2014). Predictive model for scour depth of coastal structure failures due to tsunamis. *Coastal Engineering Proceedings*, *1*(34), 56. https://doi.org/10.9753/icce.v34.structures.56

Kamphuis, J. W. (1975). Coastal mobile bed model- Does it work?. *Proceedings of the 2nd Symposium* on *Modeling* Techniques, American Society of Civil, *2*, 993–1009.

Kamphuis, J. W. (1985). On understanding scale effect in coastal mobile bed models. *Physical Modelling in Coastal Engineering*. Rotterdam, The Netherlands, 141-162.

Kamphuis, J. W. (1991). Physical Modeling. *Handbook of Coastal and Ocean Engineering*, J. B. Herbich, ed., Gulf Publishing, Houston, Texas, USA, 1049–1066.

Mansard, E. P. D., & Funke, E. R. (1980). The measurement of incident and reflected spectra using a least squares method. *Coastal Engineering 1980*, 154–172. https://doi.org/10.1061/9780872622647.008

McGovern, D. J., Todd, D., Rossetto, T., Whitehouse, R. J. S., Monaghan, J., & Gomes, E. (2019). Experimental observations of tsunami induced scour at onshore structures. *Coastal Engineering*, *152*(January), 103505. https://doi.org/10.1016/j.coastaleng.2019.103505

Nik Hassan, N. M. K., & Narayanan, R. (1985). Local scour downstream of an apron. *Journal of Hydraulic Engineering*, *111*(11), 1371–1384. https://doi.org/10.1061/(ASCE)0733-9429(1985)111:11(1371)

Oumeraci, H., D'ELISO, C., & Kortenhaus, A. (2005). Breaching of coastal dikes: state of the art. *FLOODsite*, (910). Retrieved from http://repository.tudelft.nl/view/hydro/uuid:e569363f-587a-4378-99dc-72fb35098fbc/

Rajaratnam, N. (1981). Erosion by plane turbulent jets. *Journal of Hydraulic Research*, *19*(6), 277–305. https://doi.org/10.1080/00221688109499508

Sarkar, A., & Dey, S. (2005). Scour downstream of aprons caused by sluices. *Proceedings of the Institution of Civil Engineers: Water Management*, *158*(2), 55–64. https://doi.org/10.1680/wama.2005.158.2.55

Schmocker, L., & Hager, W. H. (2010). Overtopping and breaching of dikes – Breach profile and breach flow. *Intl. Conf. River Flow*, (3), 515–522. Retrieved from https://izw.baw.de/e-medien/river-flow-2010/PDF/A4/A4_01.pdf

Si, J.-H., Lim, S.-Y., & Wang, X.-K. (2018). Flow Structures in Evolving Scour Holes Caused by a Plunging Jet Downstream of a Weir. *Journal of Hydraulic Engineering*, *144*(6), 04018018. https://doi.org/10.1061/(asce)hy.1943-7900.0001452

Soulsby, R. (1998). *Dynamics of Marine Sands (HR Wallingford Titles): A Manual for Practical Applications*.

Stanczak, G. (2008). *Breaching of sea dikes initiated from the seaside by breaking wave impacts . PhD-Thesis, Technische Universität Braunschweig, Germany and Uni-versita degli Studi di Firenze, Florence, Italy, 143pp* (Universtiy of Florence, Florence). Retrieved from http://www.digibib.tu-bs.de/?docid=0002388

Steendam, G. J., Van Hoven, A., Van der Meer, J., & Hoffmans, G. (2014). Wave overtopping simulator tests on transitions and obstacles at grass covered slopes of dikes. *Coastal Engineering Proceedings*, *1*(34), 79. https://doi.org/10.9753/icce.v34.structures.79

Stein, O. R., Julien, P. Y., & Alonso, C. V. (1993). Mechanics of jet scour downstream of a headcut. *Journal of Hydraulic Research*, *31*(6), 723–738. https://doi.org/10.1080/00221689309498814

Sumer, B. M., & Fredsøe, J. (2002). *The Mechanics of Scour in the Marine Environment*. https://doi.org/10.1142/4942

Tsujimoto, G., Mineura, R., Yamada, F., Kakinoki, T., & Uno, K. (2014). Scouring mechanism behind seawall from tsunami overflow and optimum conditions to reduce tsunami energy with an artificial trench. *Coastal Engineering Proceedings*, *1*(34), 38. https://doi.org/10.9753/icce.v34.structures.38

Wang, L., Melville, B. W., & Guan, D. (2018a). Effects of upstream weir slope on local scour at submerged weirs. *Journal of Hydraulic Engineering*, *144*(3), 04018002. https://doi.org/10.1061/(asce)hy.1943-7900.0001431

Wang, L., Melville, B. W., Guan, D., & Whittaker, C. N. (2018b). Local scour at downstream sloped submerged weirs. *Journal of Hydraulic Engineering*, *144*(8), 04018044. https://doi.org/10.1061/(asce)hy.1943-7900.0001492

Wang, L., Melville, B. W., Whittaker, C. N., & Guan, D. (2019). Scour estimation downstream of submerged weirs. *Journal of Hydraulic Engineering*, *145*(12), 06019016. https://doi.org/10.1061/(asce)hy.1943-7900.0001654

Warmink, J. J., Van Bergeijk, V. M., Chen, W., Van Gent, M. R. A., & Hulscher, S. J. M. H. (2018). Modelling wave overtopping for grass covers and transitions in dike revetments. *Coastal Engineering Proceedings*, (36), 53. https://doi.org/10.9753/icce.v36.papers.53

APPENDICES

A. Scour Formations and Development Curves for Tests with $d_{50} = 0.21$ mm

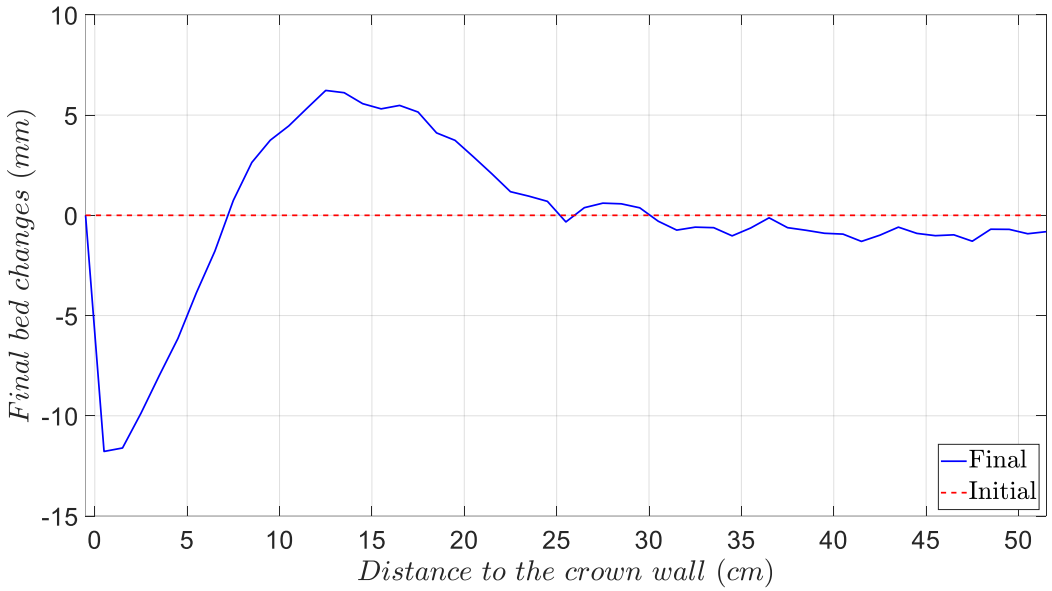

Figure 0.1. Final morphological changes for S-Test-1

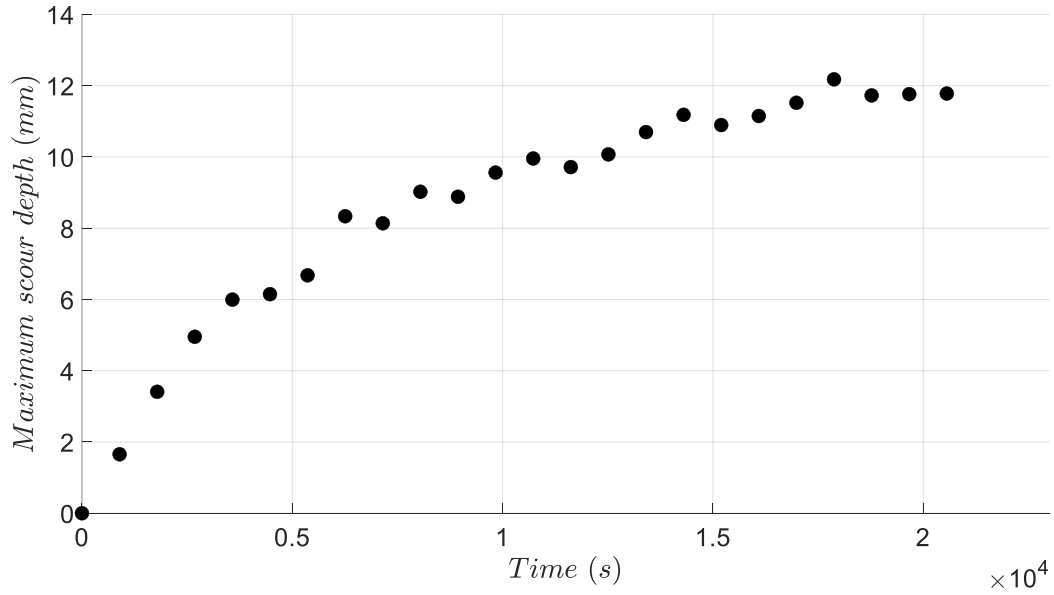

Figure 0.2. Scour development in time for S-Test-1

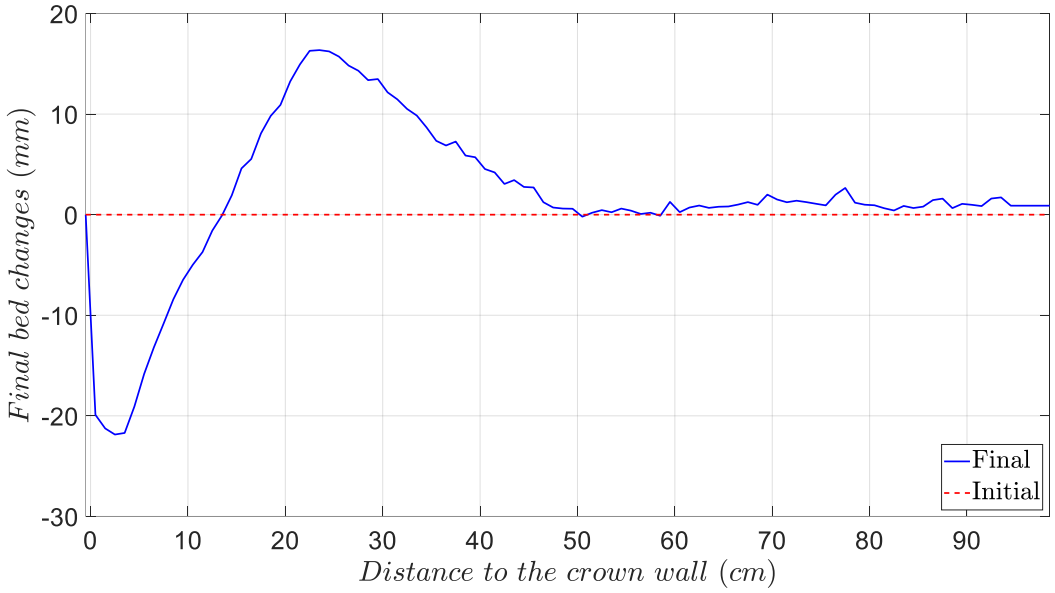

Figure 0.3. Final morphological changes for S-Test-2

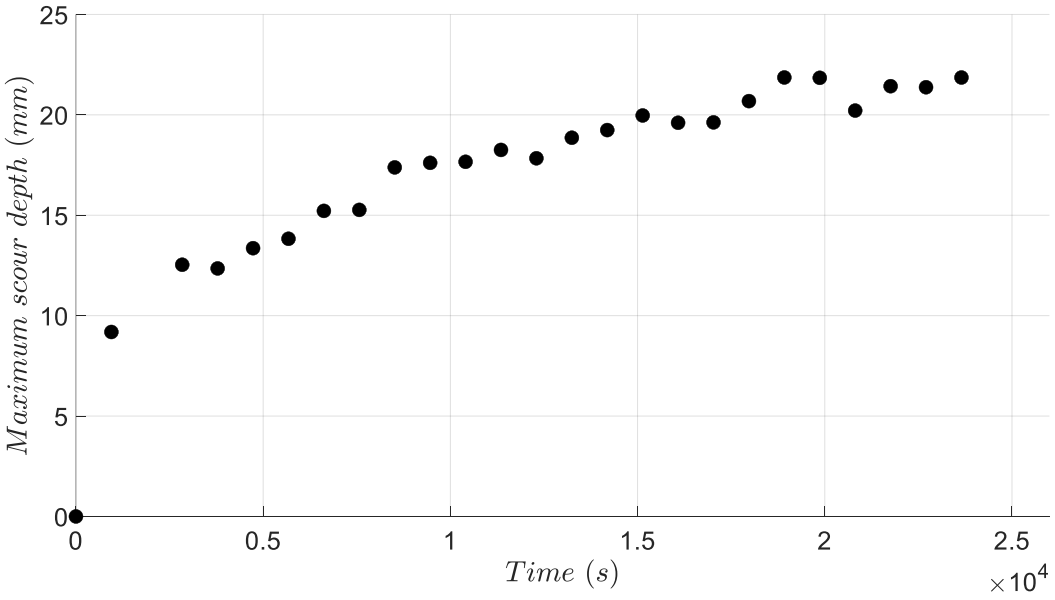

Figure 0.4. Scour development in time for S-Test-2

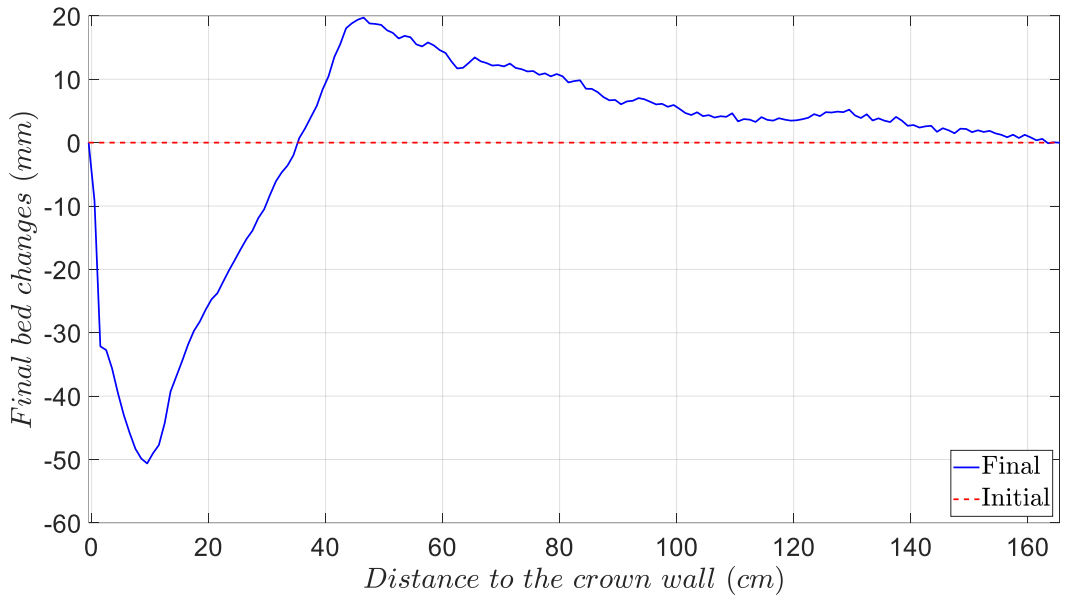

Figure 0.5. Final morphological changes for S-Test-3

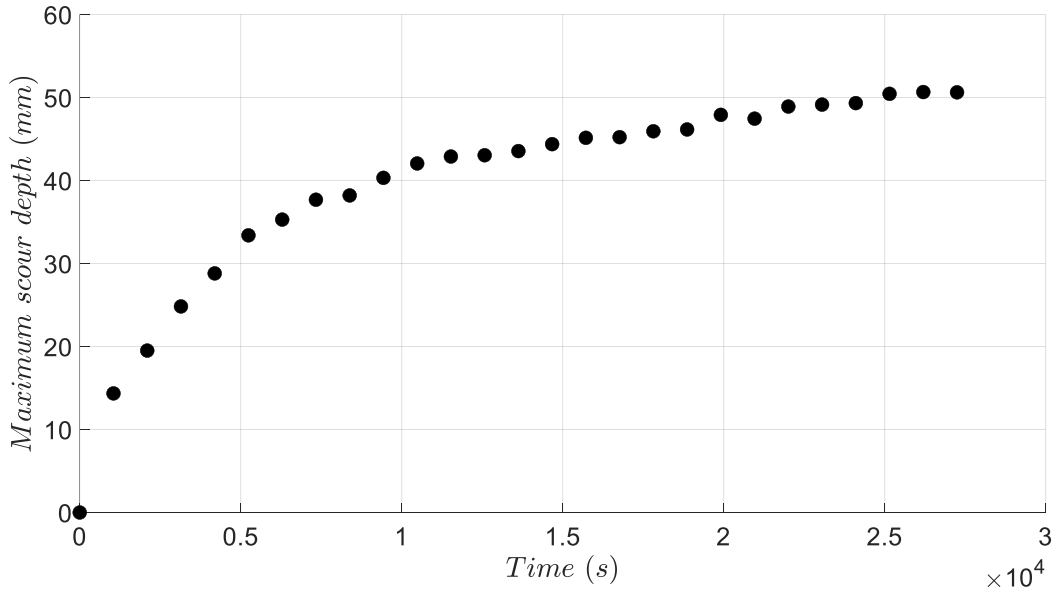

Figure 0.6. Scour development in time for S-Test-3

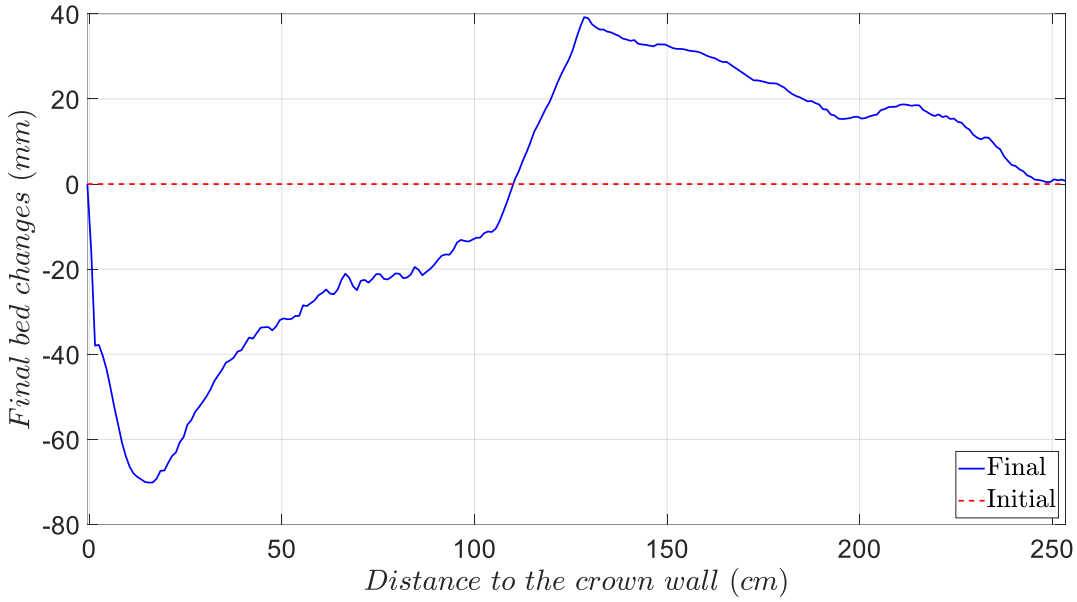

Figure 0.7. Final morphological changes for S-Test-4

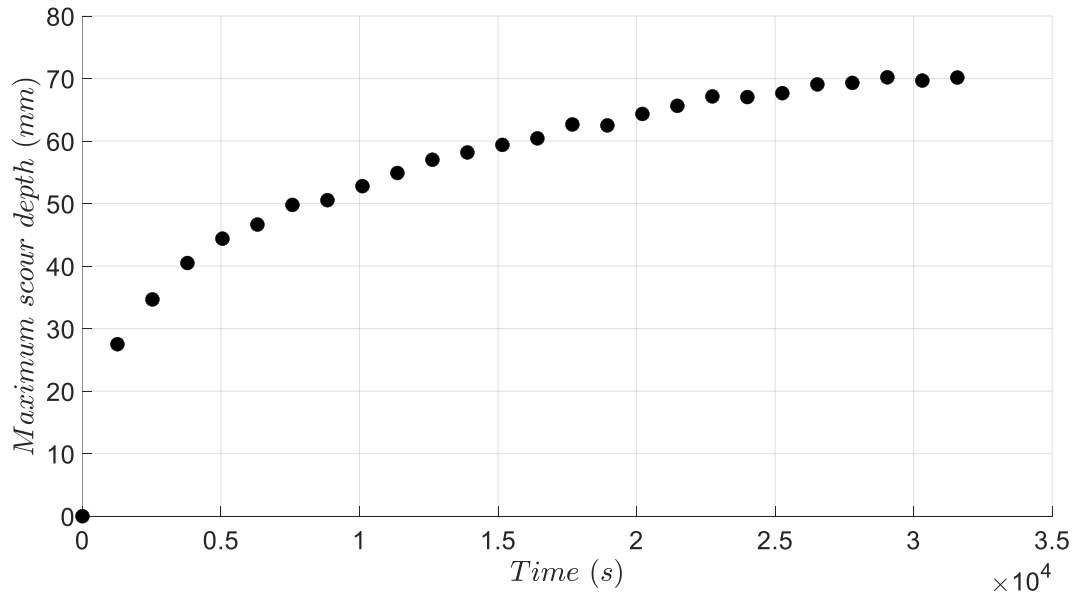

Figure 0.8. Scour development in time for S-Test-4

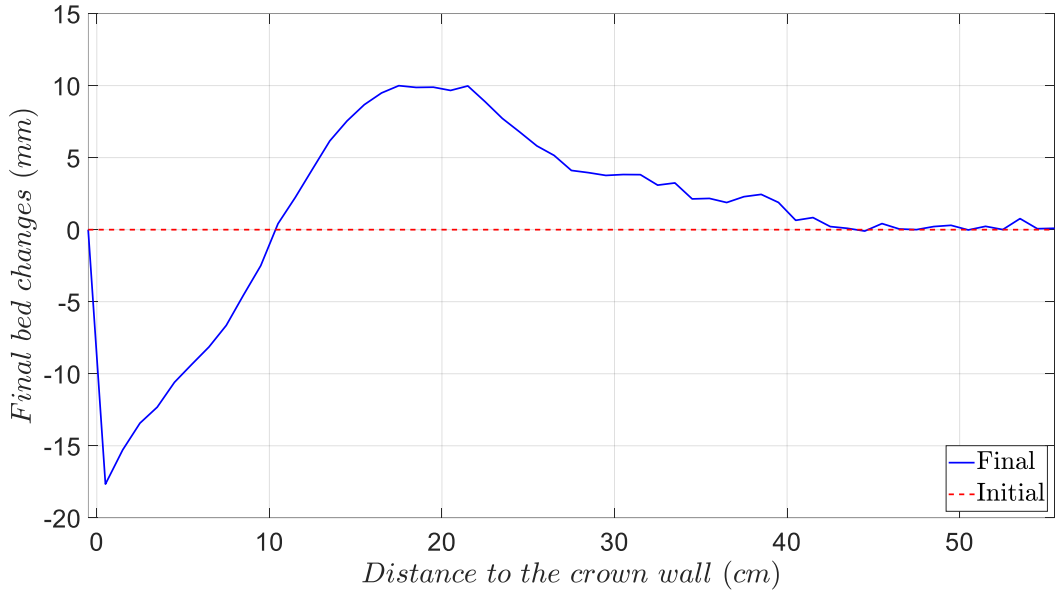

Figure 0.9. Final morphological changes for S-Test-5

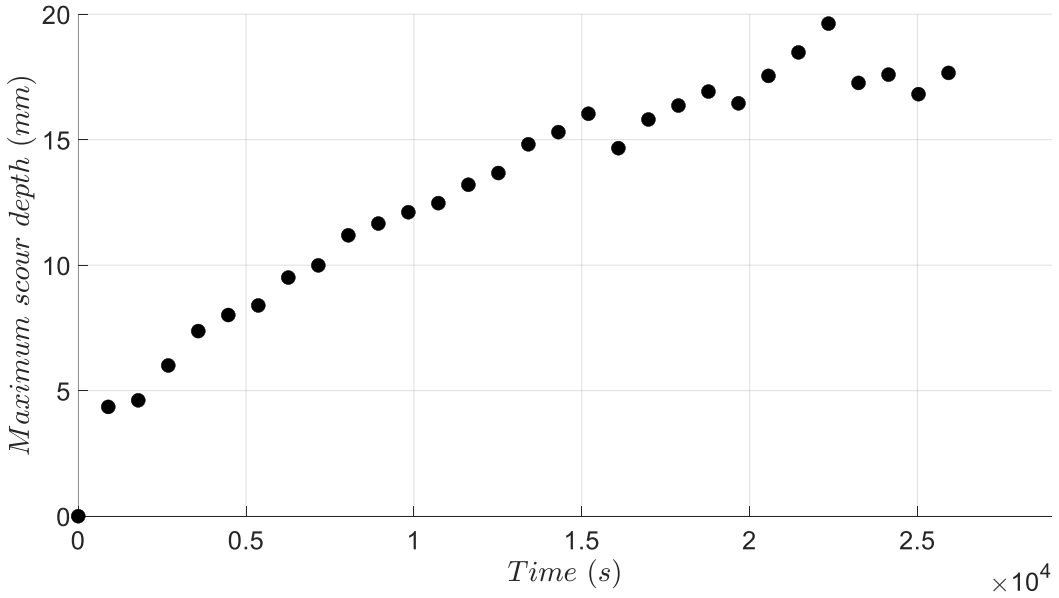

Figure 0.10. Scour development in time for S-Test-5

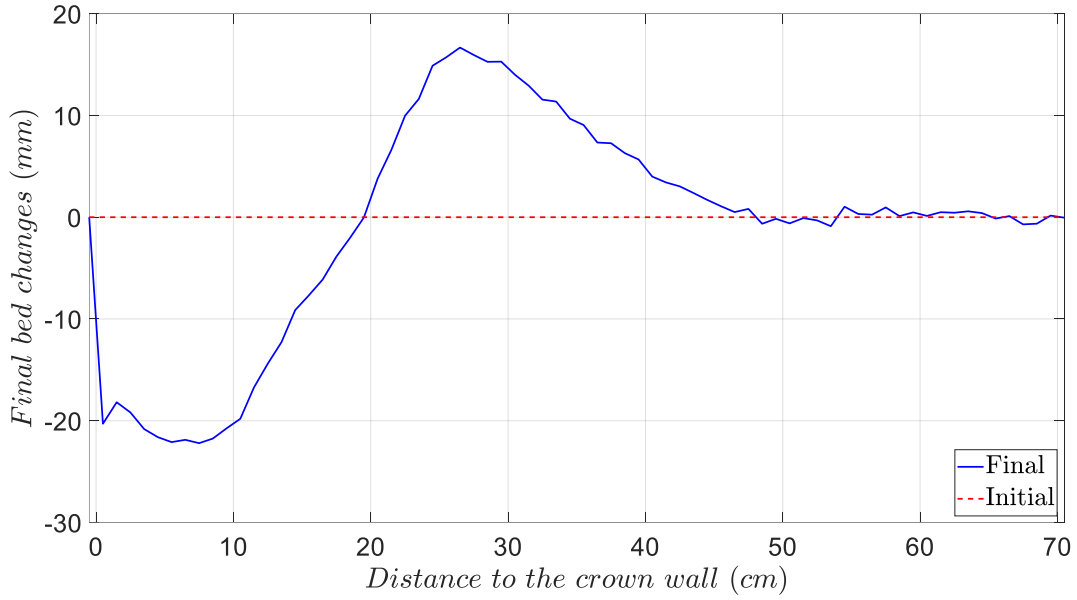

Figure 0.11. Final morphological changes for S-Test-6

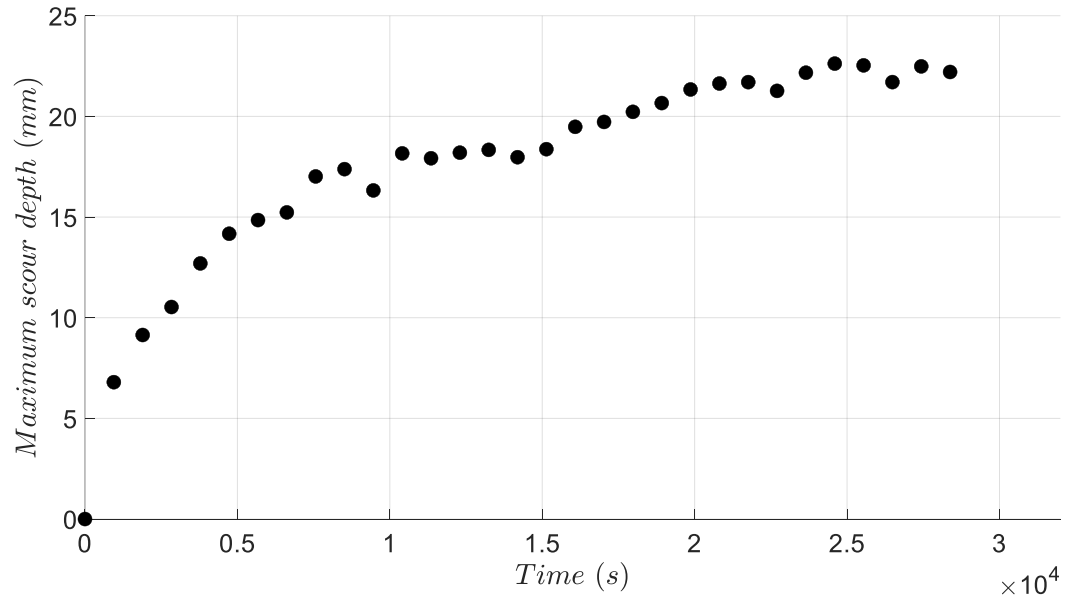

Figure 0.12. Scour development in time for S-Test-6

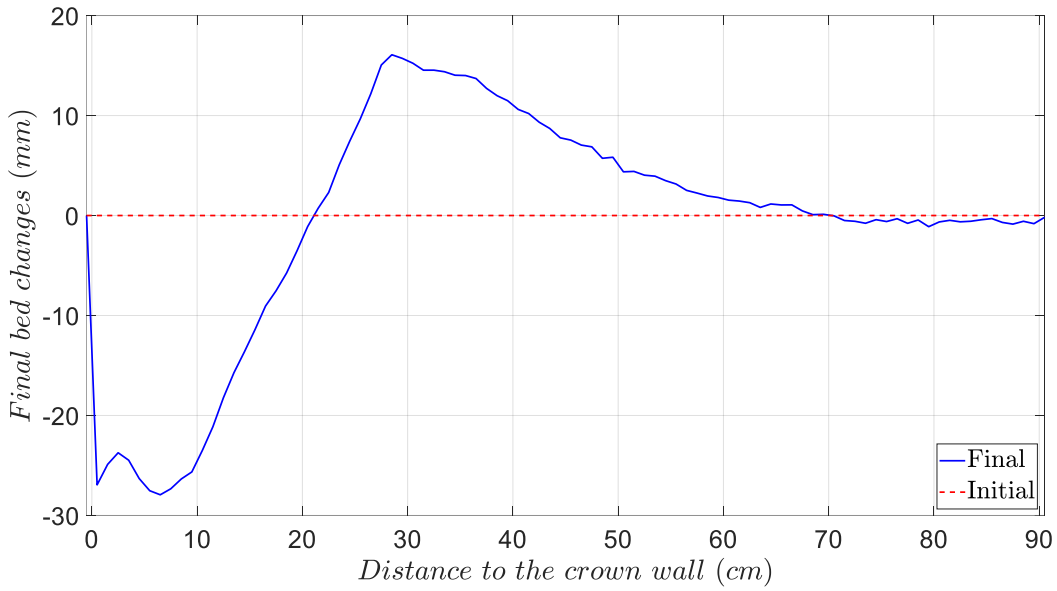

Figure 0.13. Final morphological changes for S-Test-7

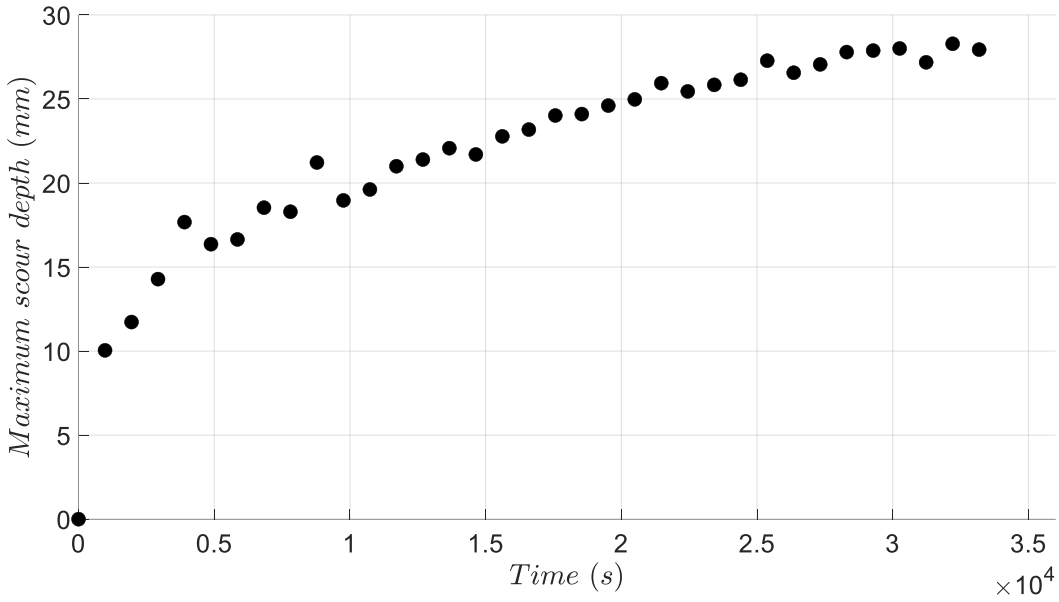

Figure 0.14. Scour development in time for S-Test-7

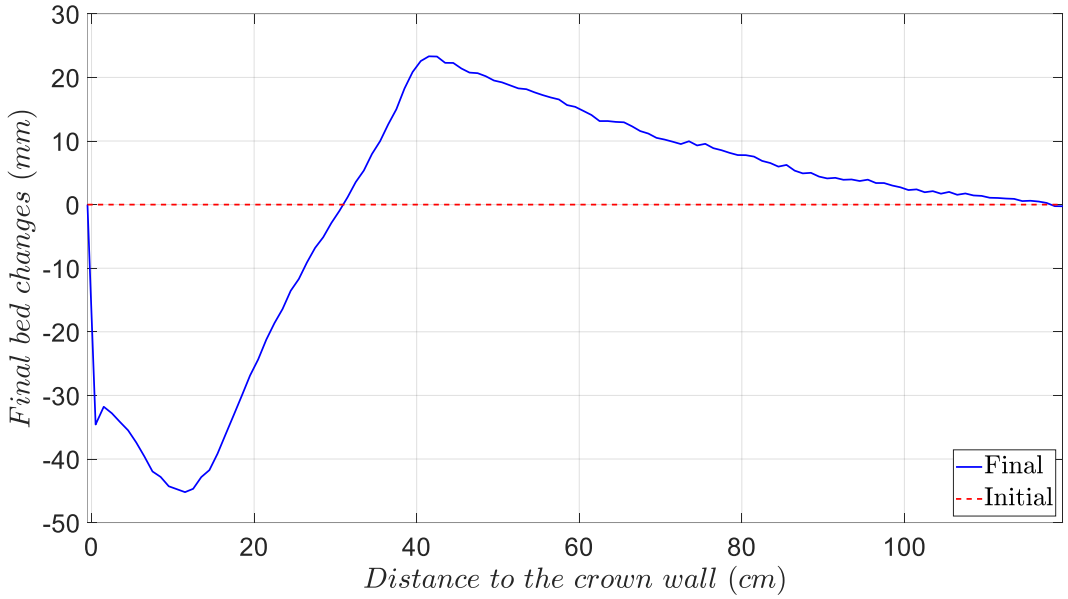

Figure 0.15. Final morphological changes for S-Test-8

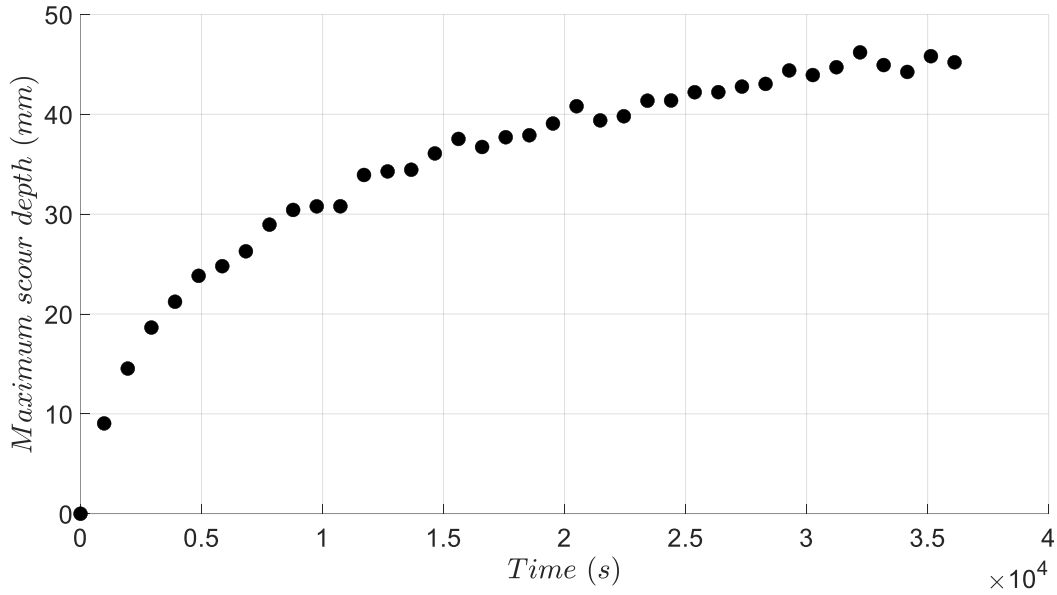

Figure 0.16. Scour development in time for S-Test-8

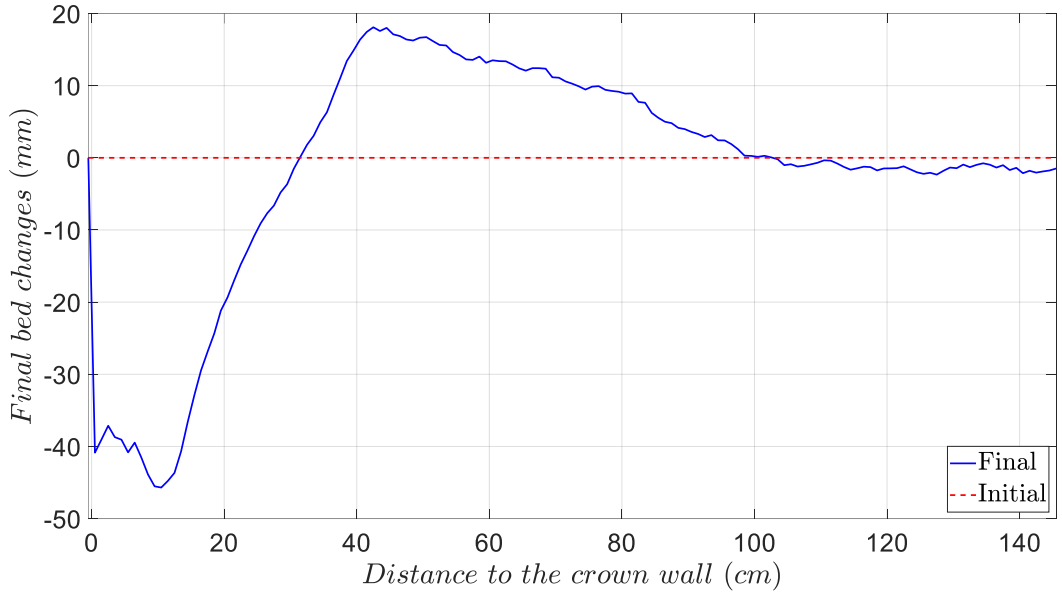

Figure 0.17. Final morphological changes for S-Test-9

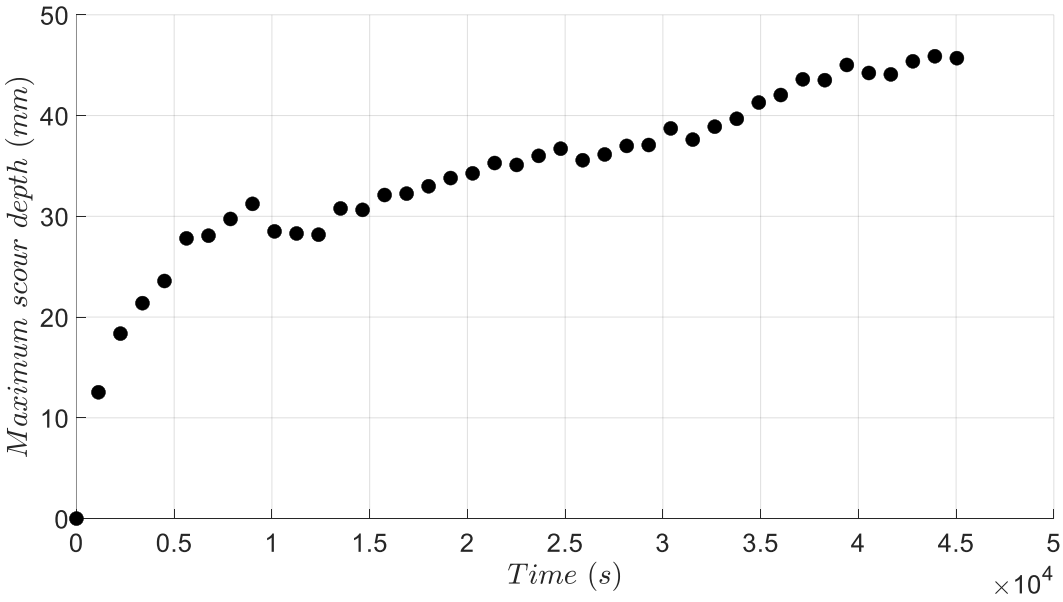

Figure 0.18. Scour development in time for S-Test-9

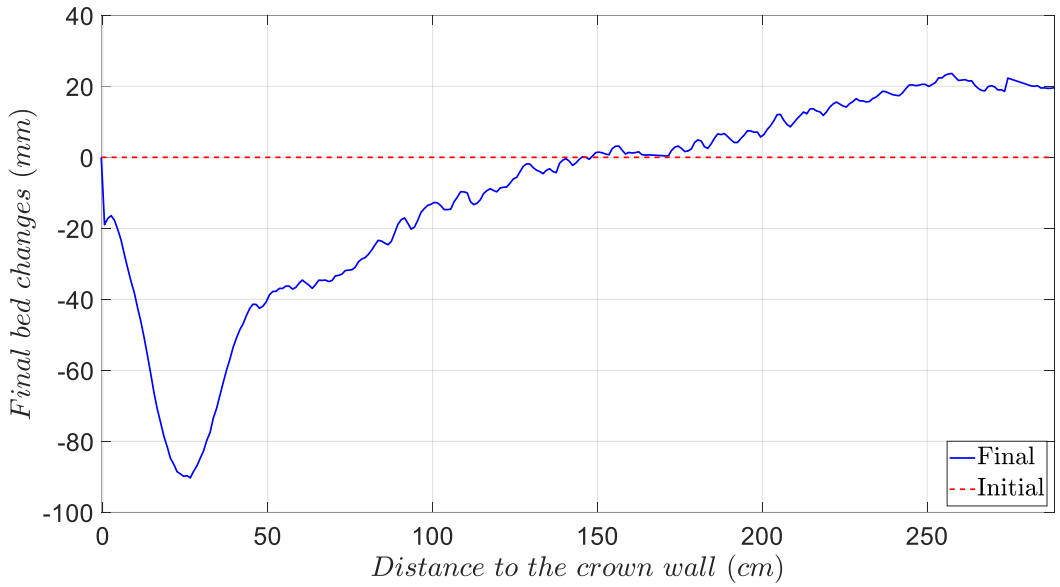

Figure 0.19. Final morphological changes for S-Test-10

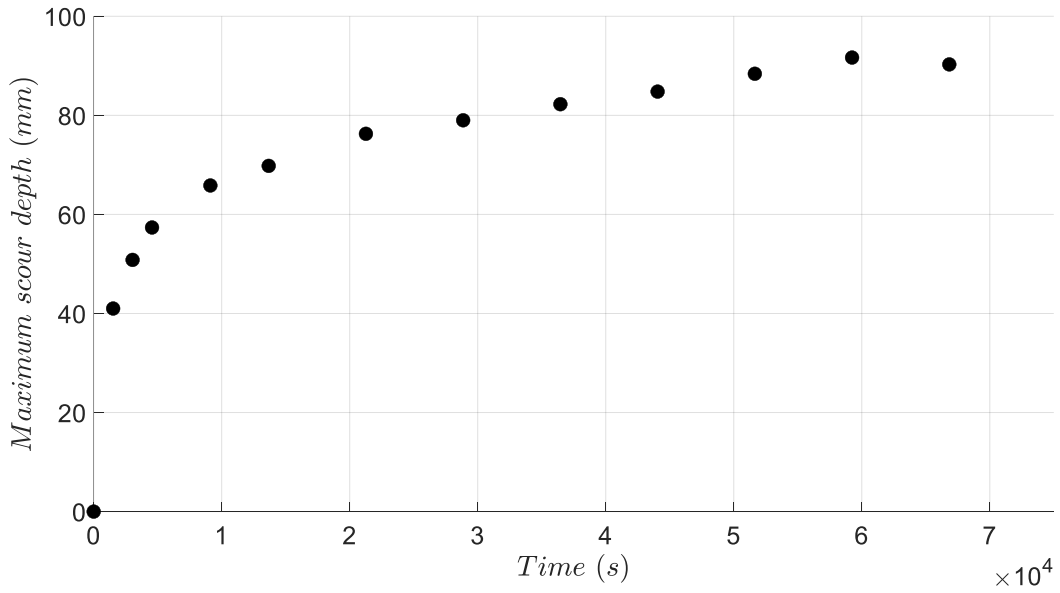

Figure 0.20. Scour development in time for S-Test-10

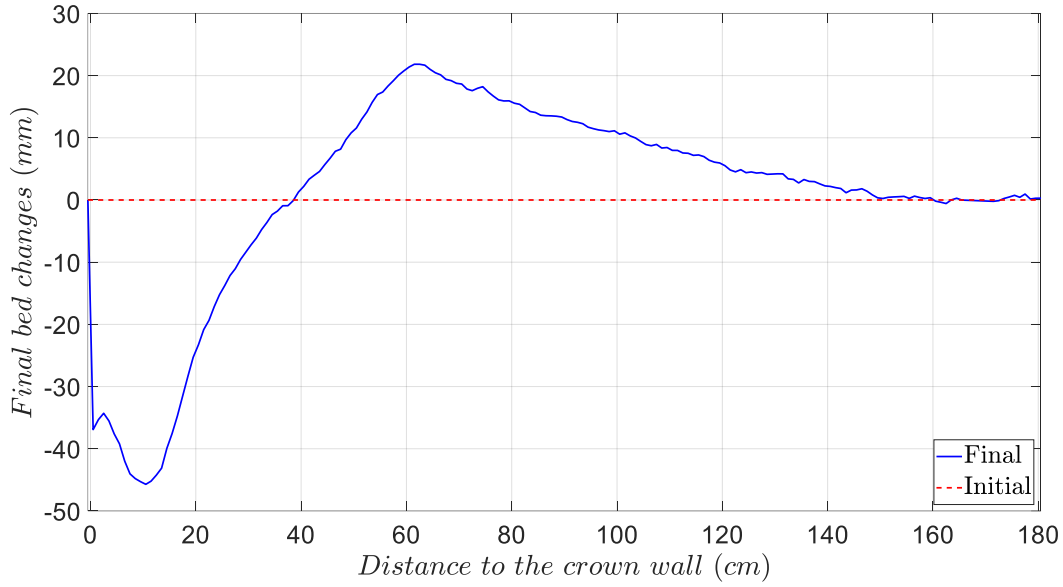

Figure 0.21. Final morphological changes for S-Test-11

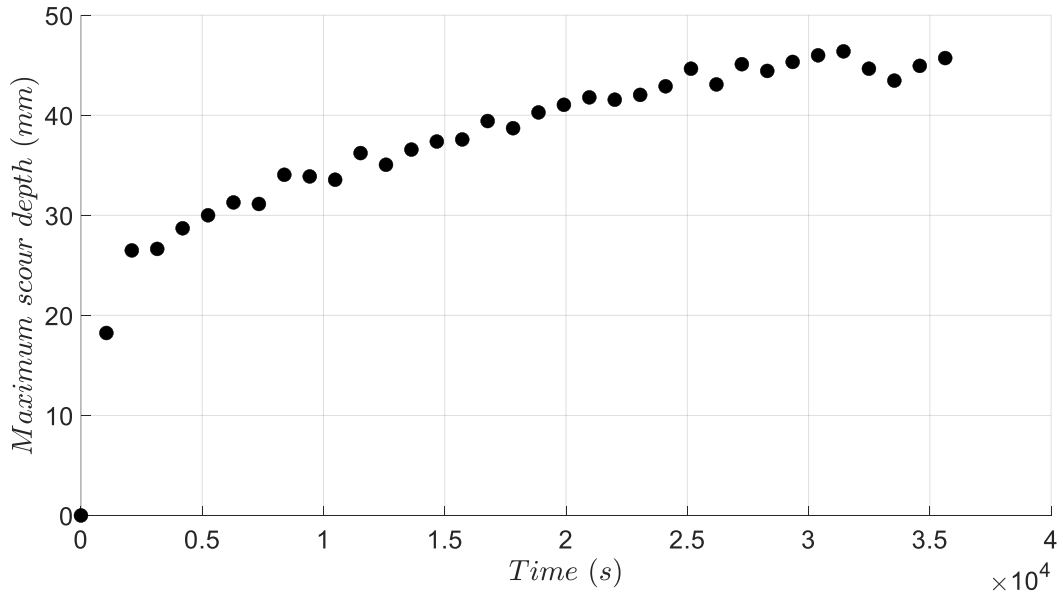

Figure 0.22. Scour development in time for S-Test-11

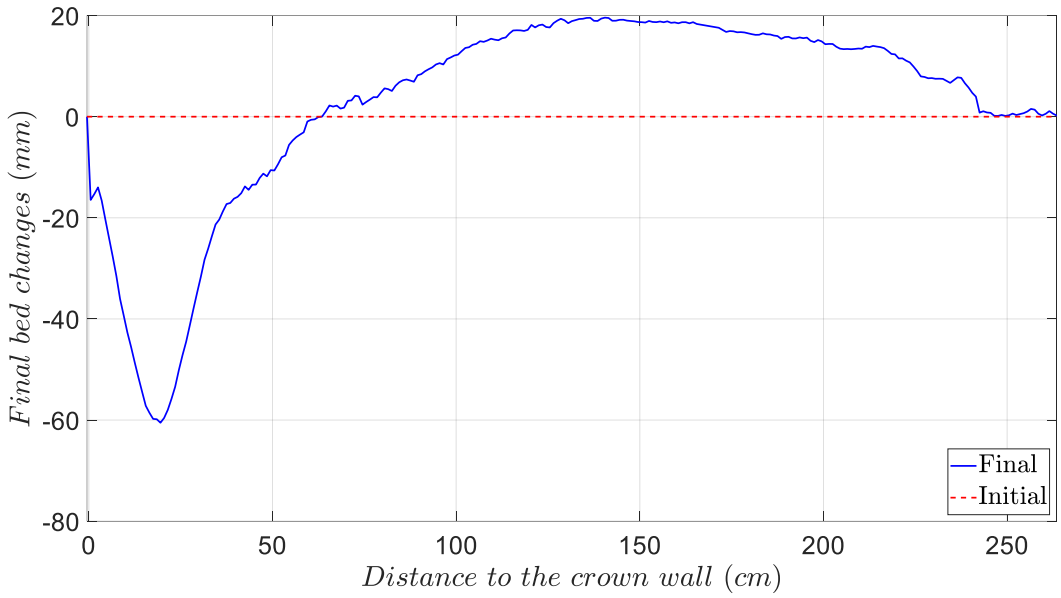

Figure 0.23. Final morphological changes for S-Test-12

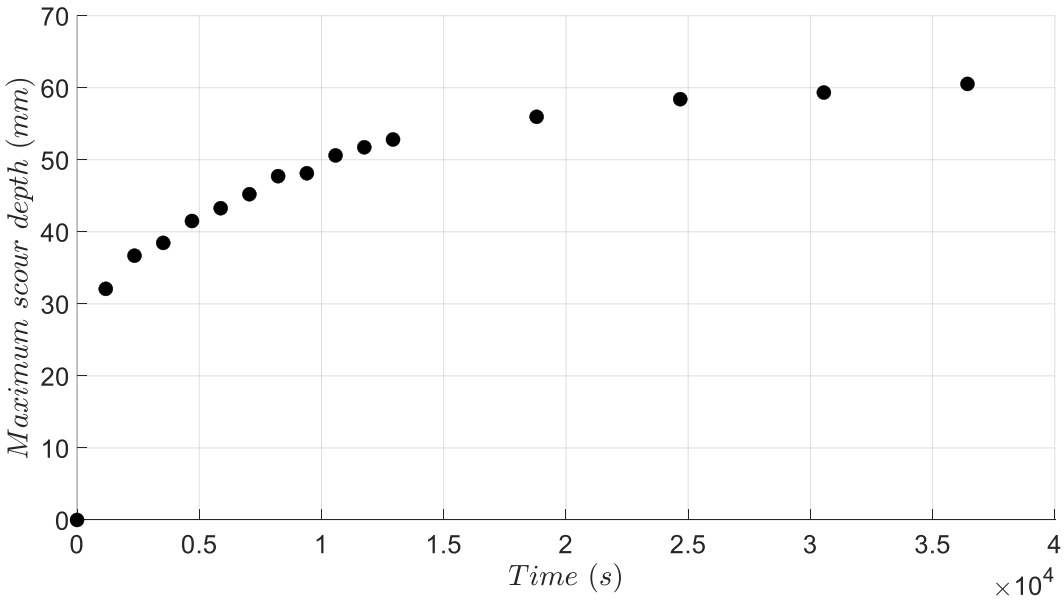

Figure 0.24. Scour development in time for S-Test-12

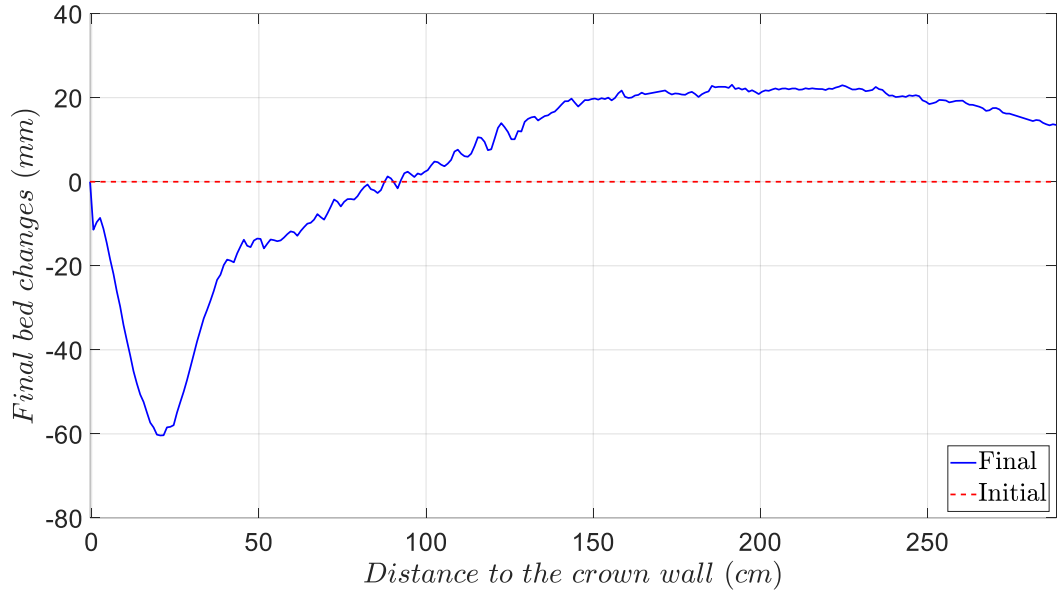

Figure 0.25. Final morphological changes for S-Test-13

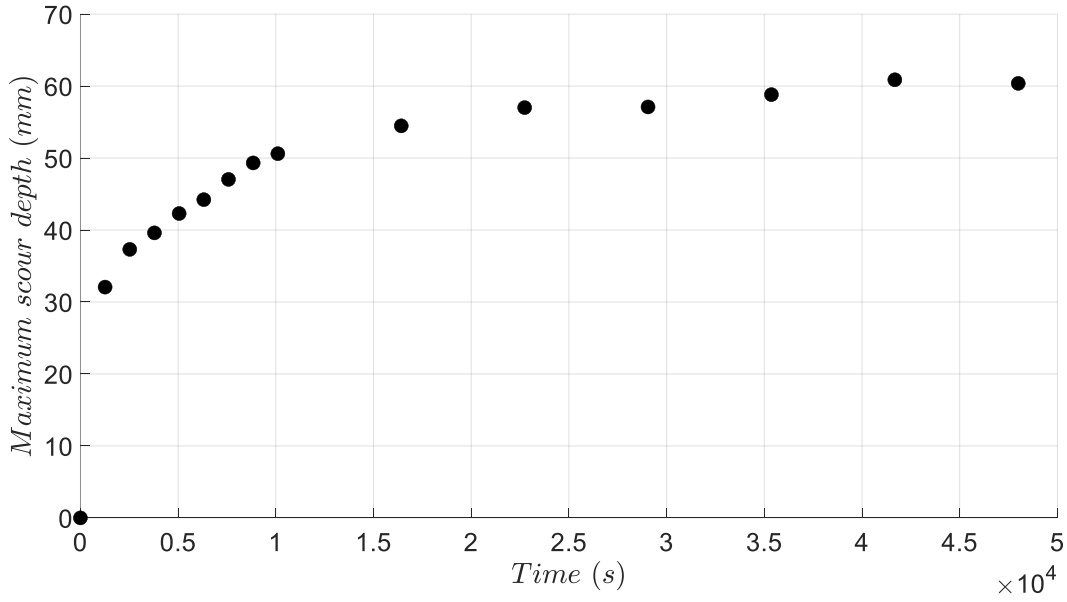

Figure 0.26. Scour development in time for S-Test-13

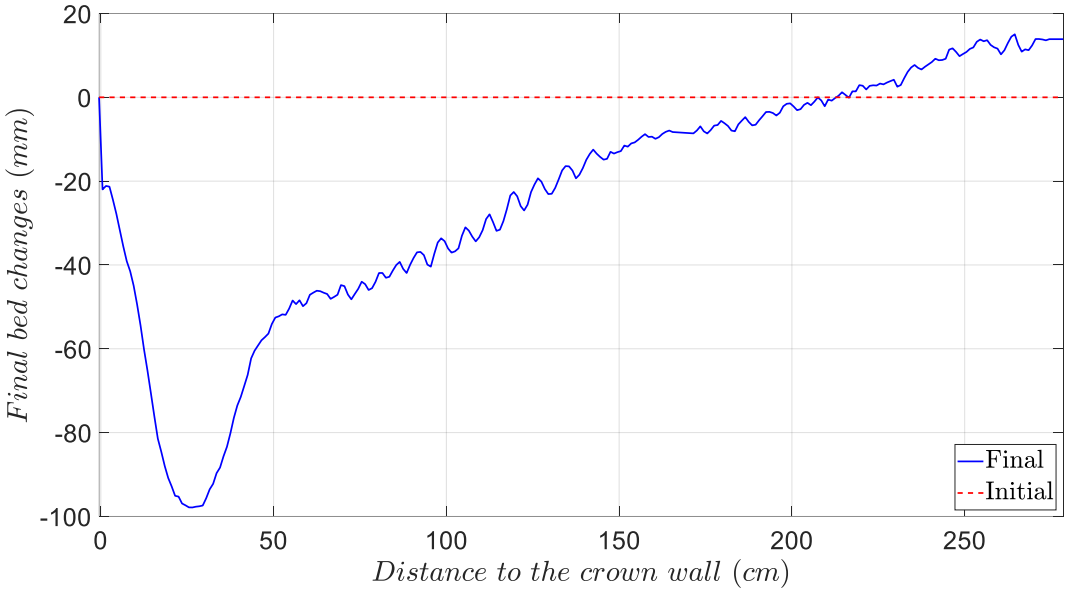

Figure 0.27. Final morphological changes for S-Test-14

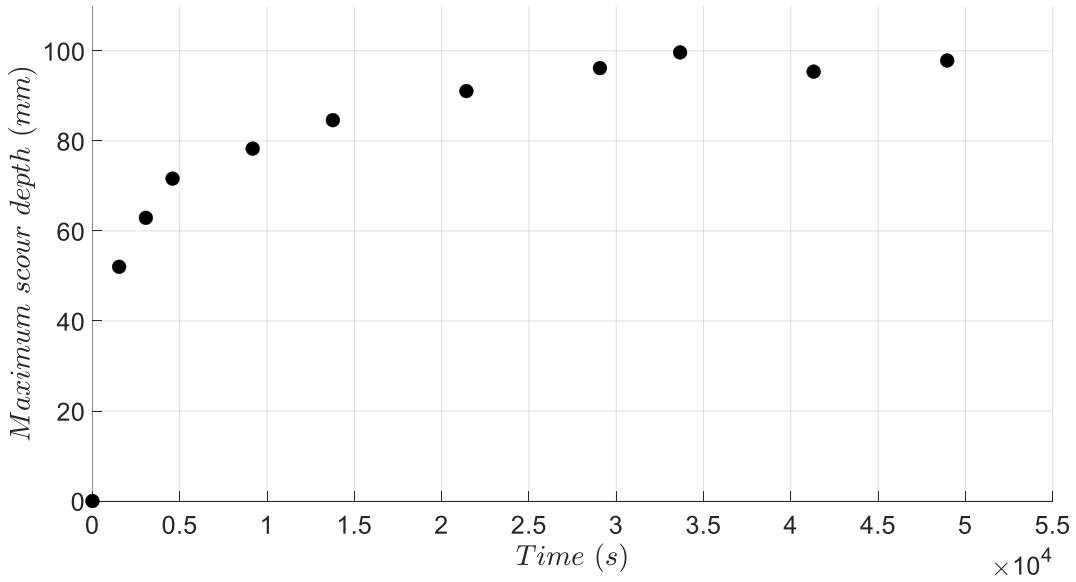

Figure 0.28. Scour development in time for S-Test-14

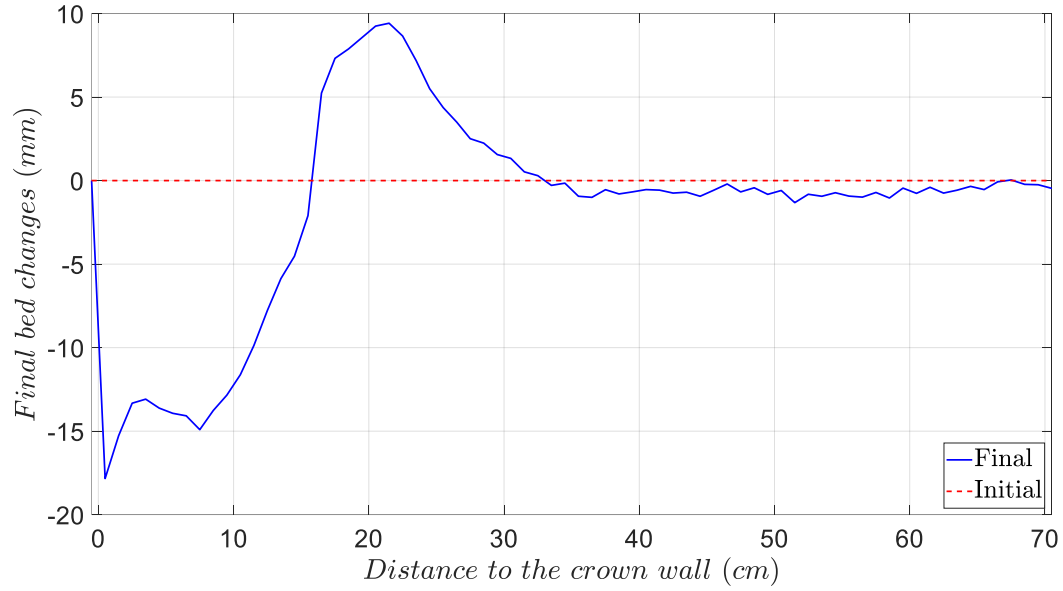

Figure 0.29. Final morphological changes for S-Test-15

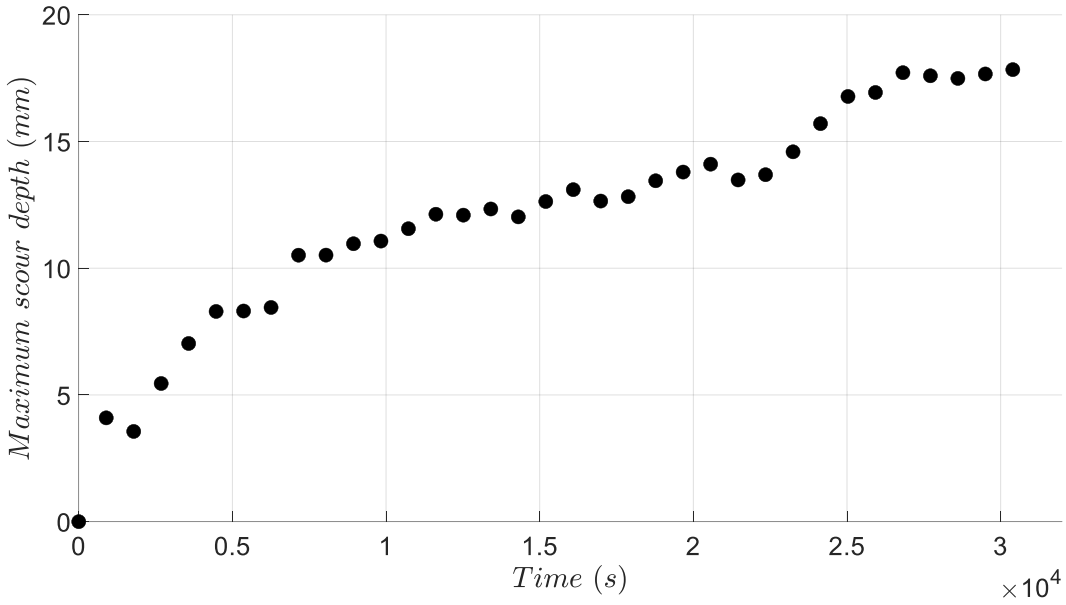

Figure 0.30. Scour development in time for S-Test-15

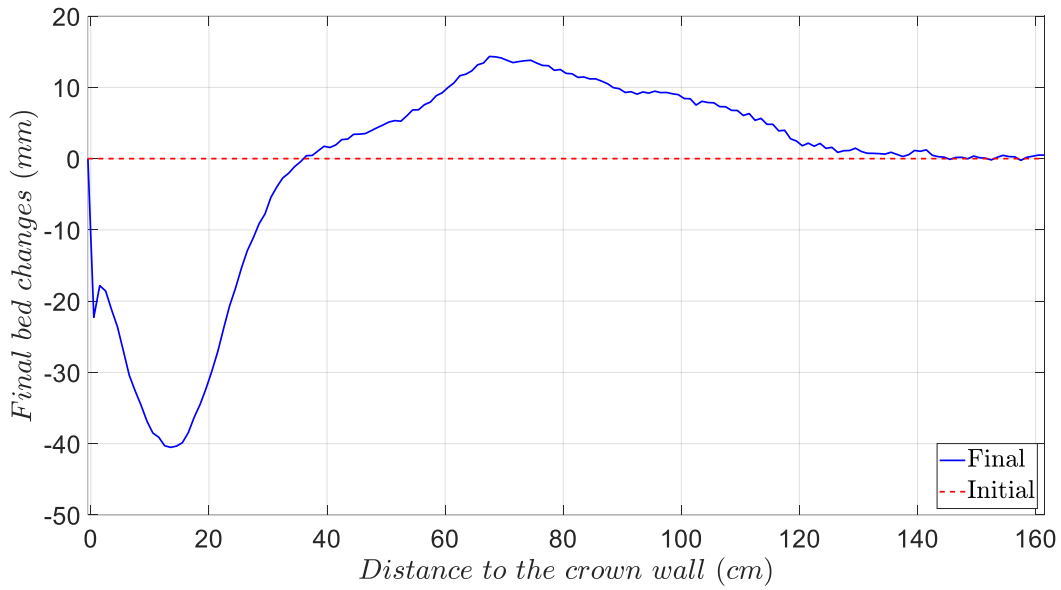

Figure 0.31. Final morphological changes for S-Test-16

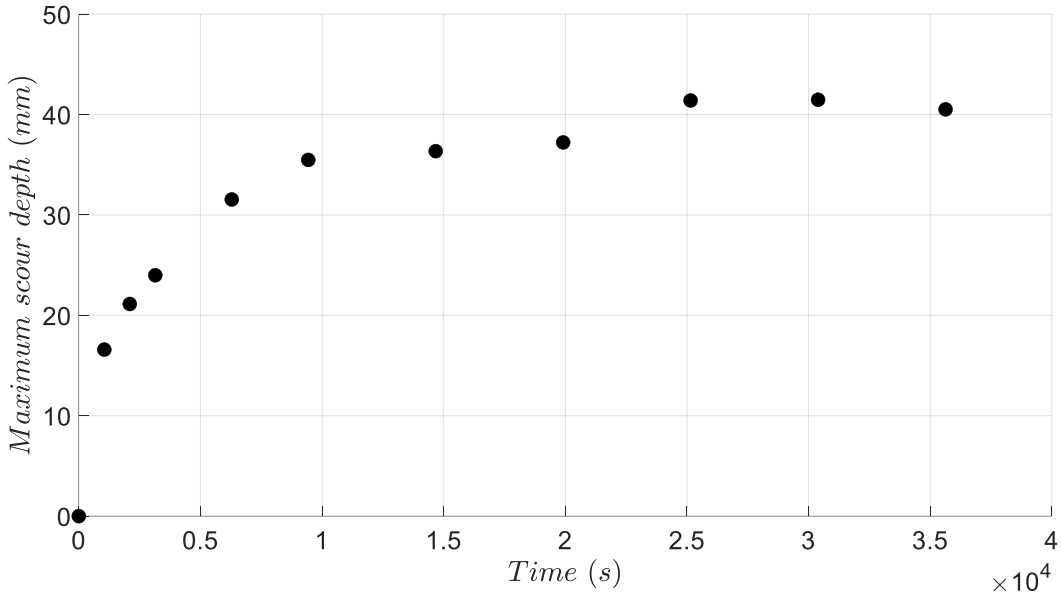

Figure 0.32. Scour development in time for S-Test-16

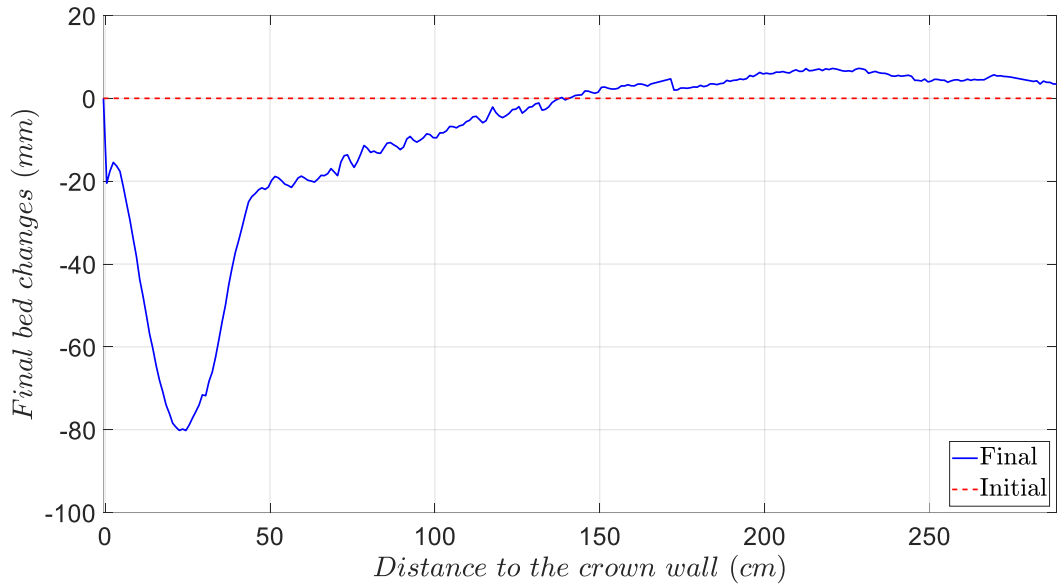

Figure 0.33. Final morphological changes for S-Test-17

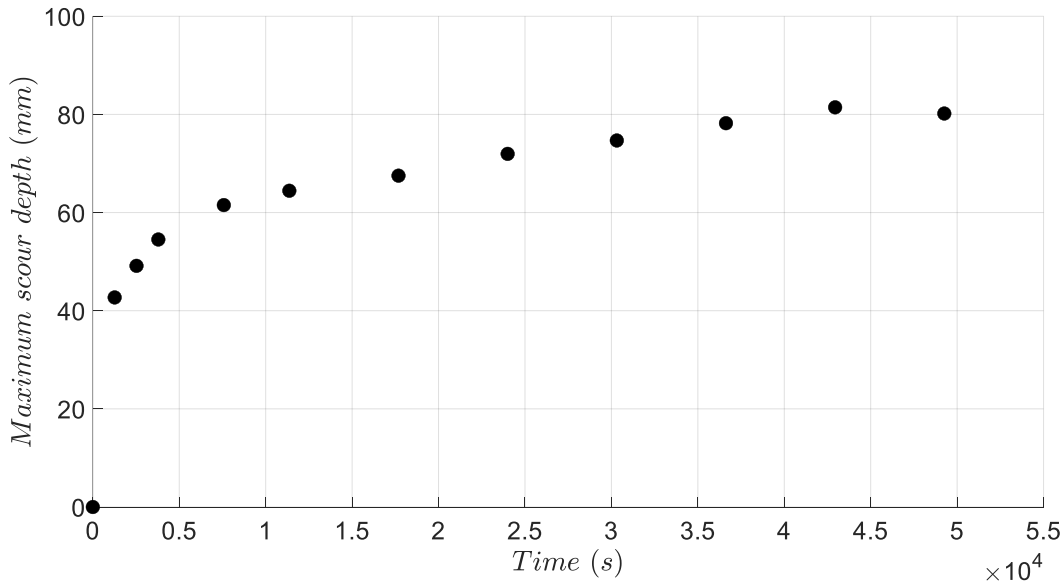

Figure 0.34. Scour development in time for S-Test-17

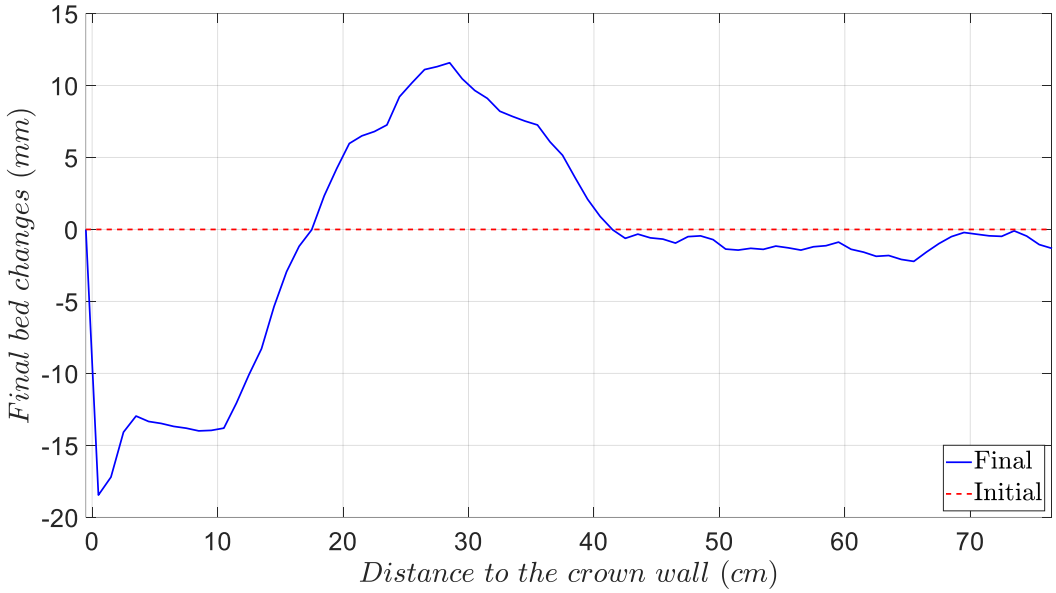

Figure 0.35. Final morphological changes for S-Test-18

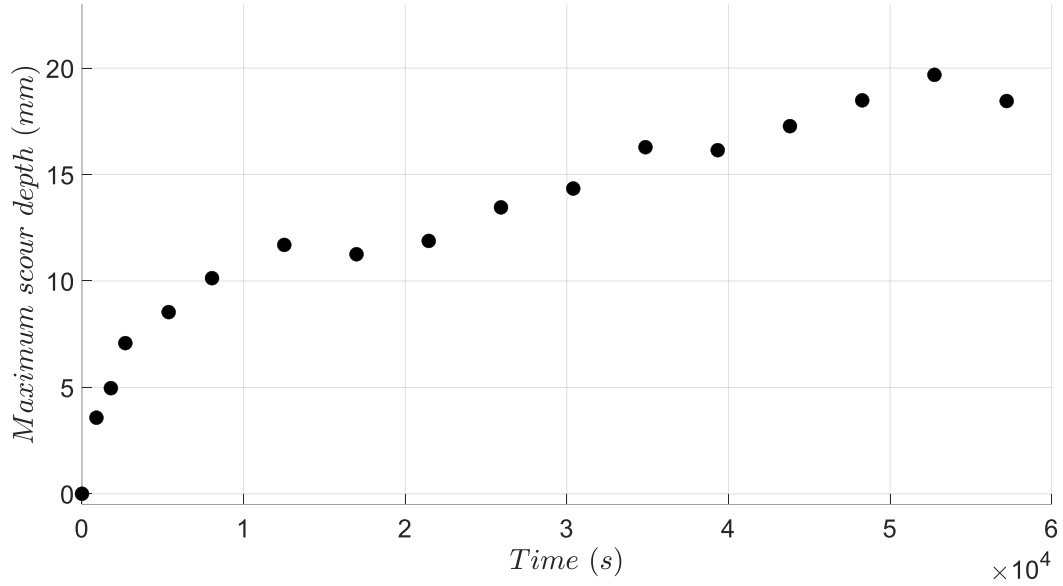

Figure 0.36. Scour development in time for S-Test-18

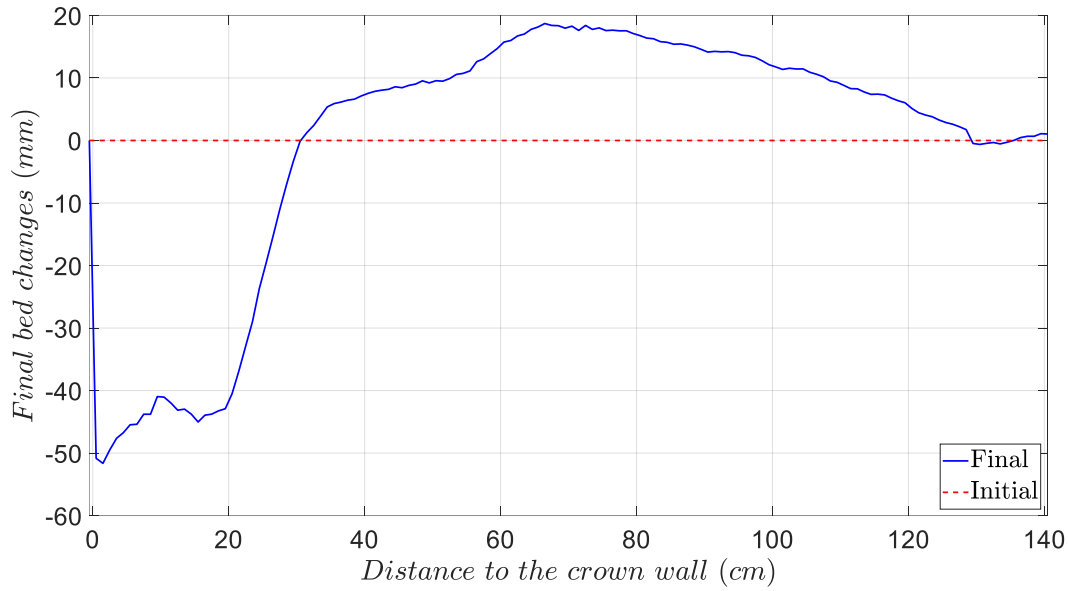

Figure 0.37. Final morphological changes for S-Test-19

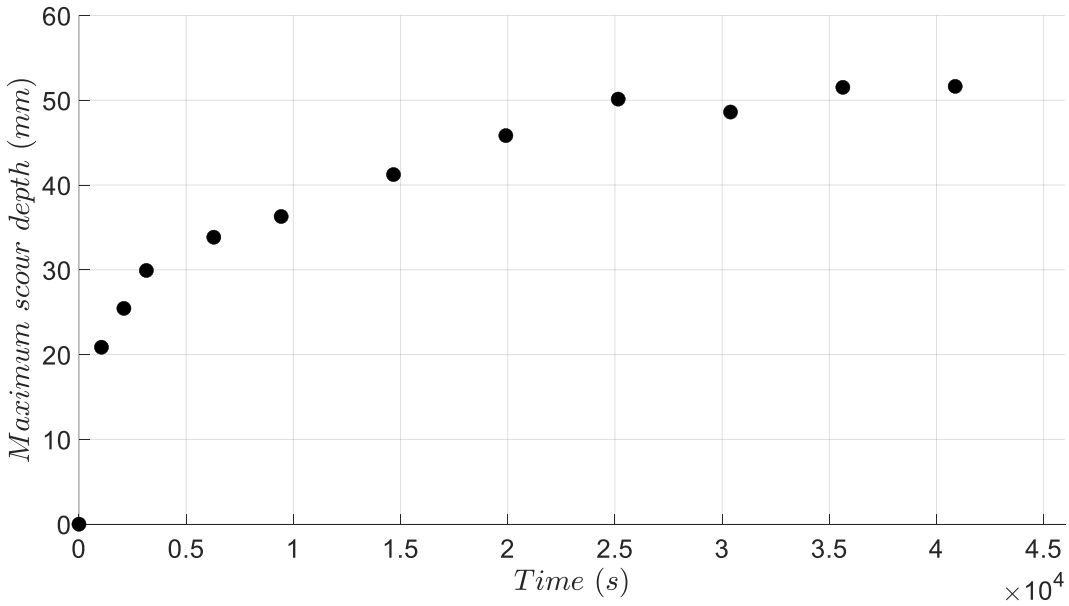

Figure 0.38. Scour development in time for S-Test-19

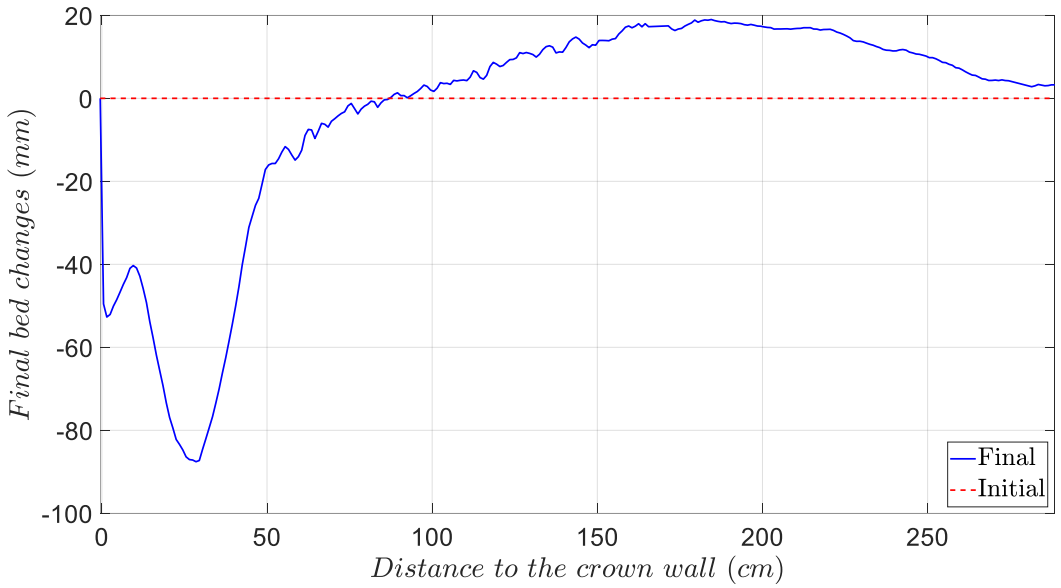

Figure 0.39. Final morphological changes for S-Test-20

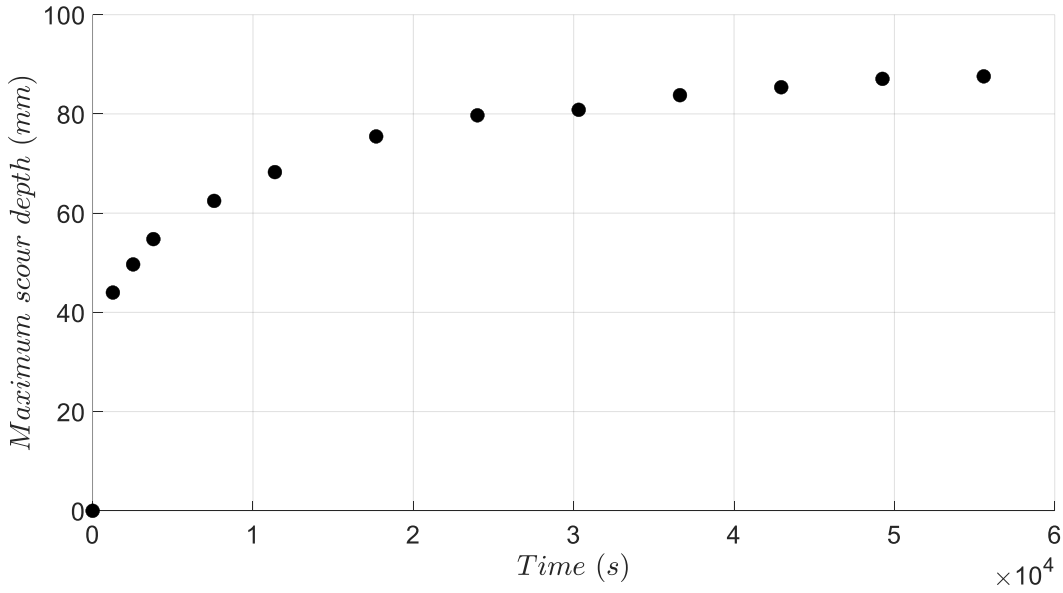

Figure 0.40. Scour development in time for S-Test-20

B. Scour Formations and Development Curves for Tests with $d_{50} = 0.66$ mm

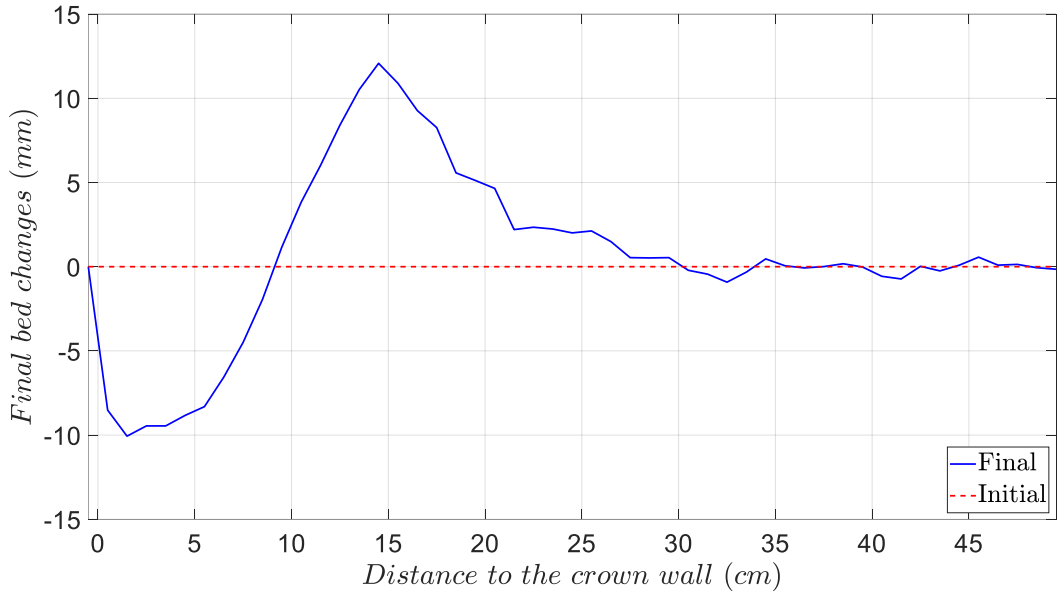

Figure 0.41. Final morphological changes for S-Test-21

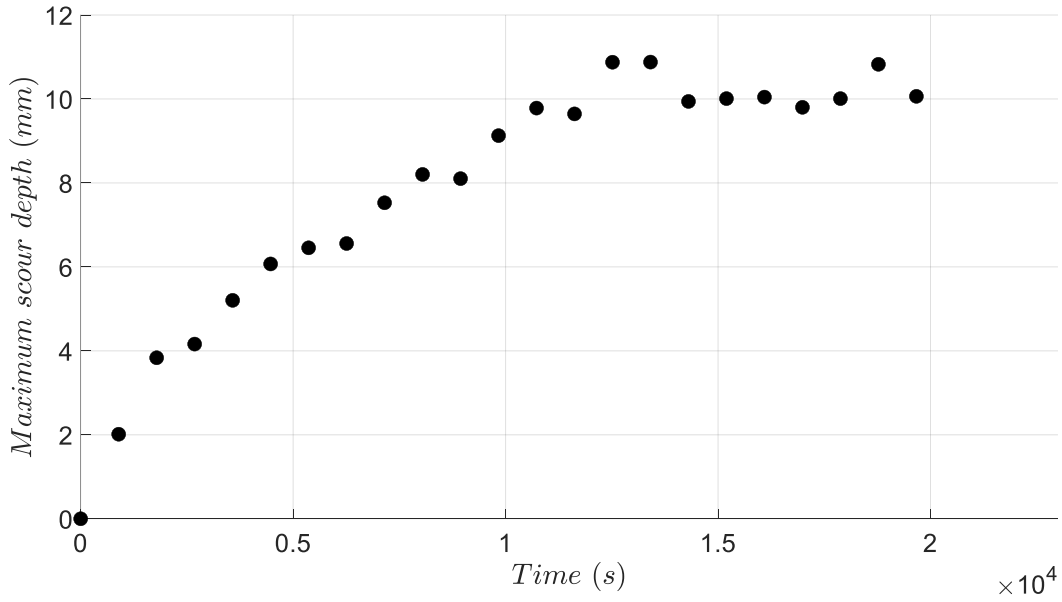

Figure 0.42. Scour development in time for S-Test-21

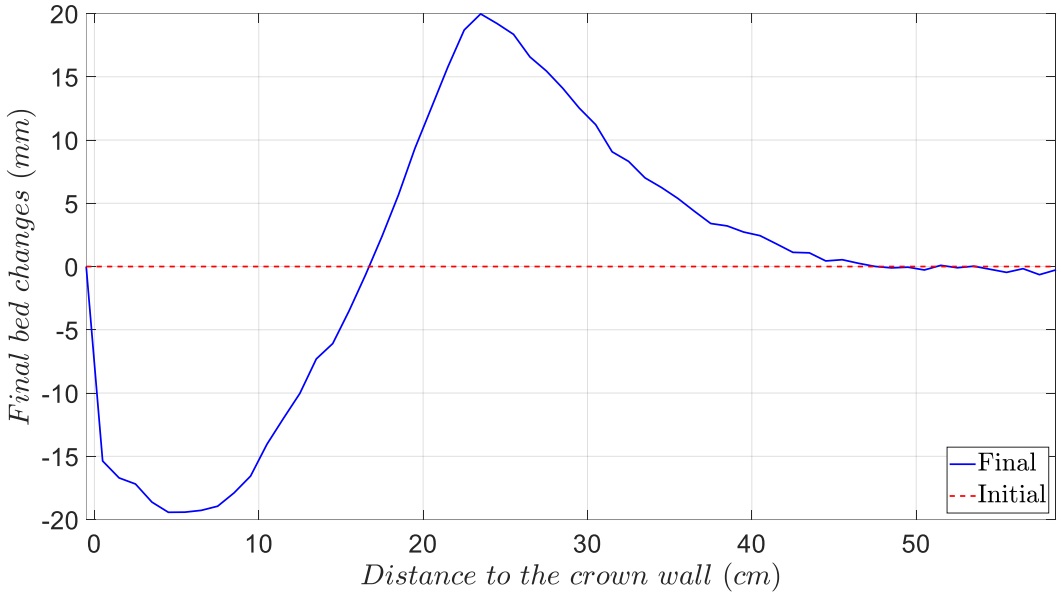

Figure 0.43. Final morphological changes for S-Test-22

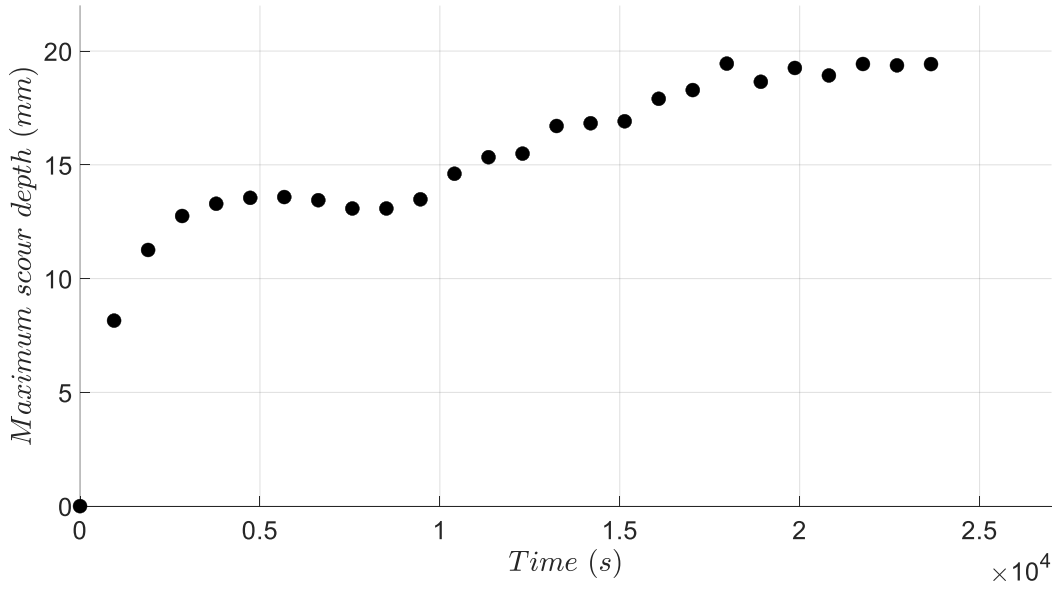

Figure 0.44. Scour development in time for S-Test-22

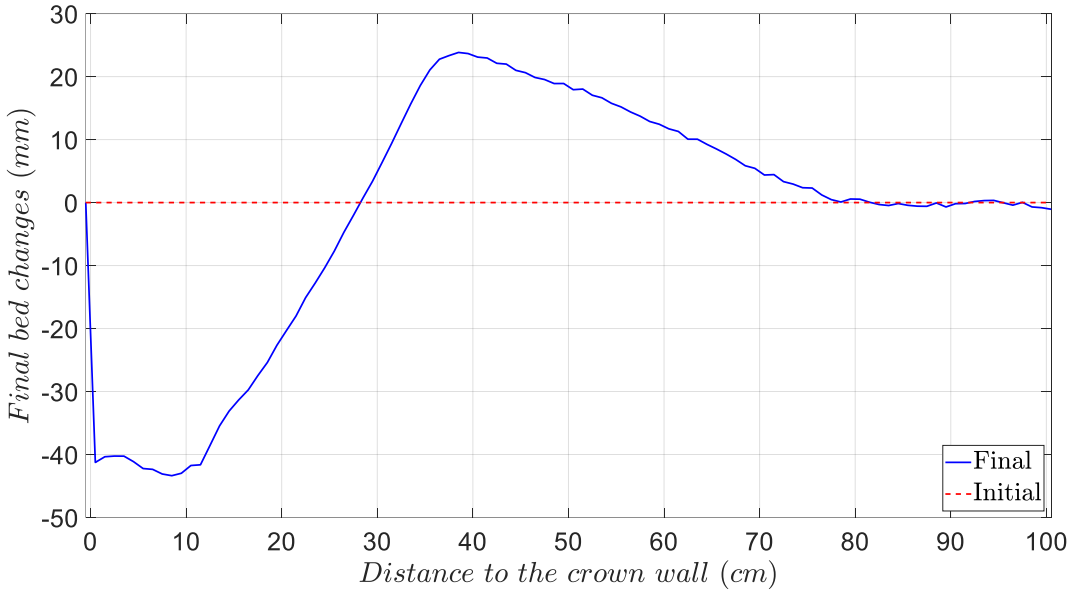

Figure 0.45. Final morphological changes for S-Test-23

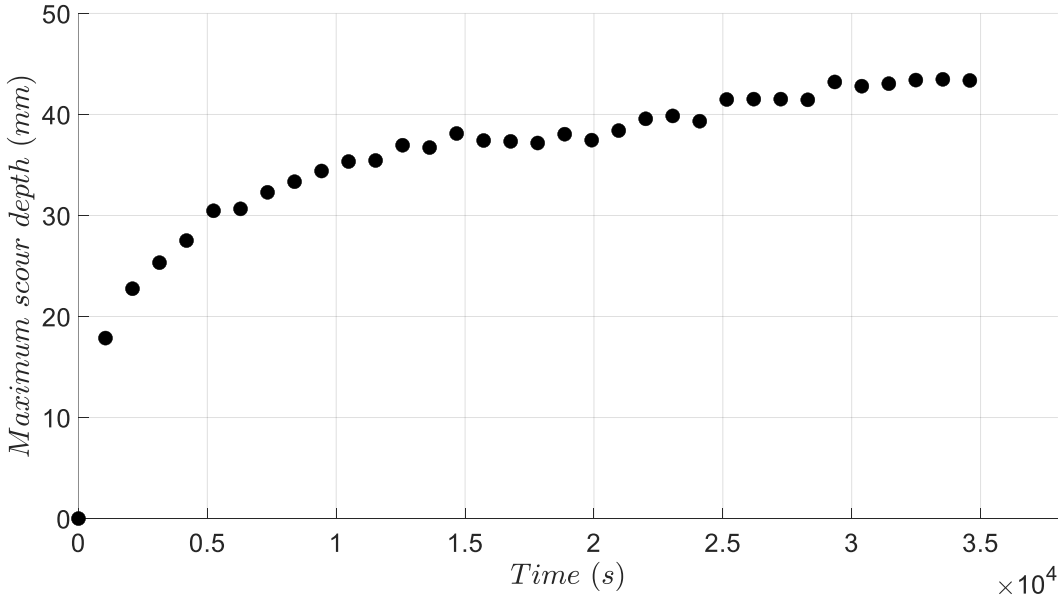

Figure 0.46. Scour development in time for S-Test-23

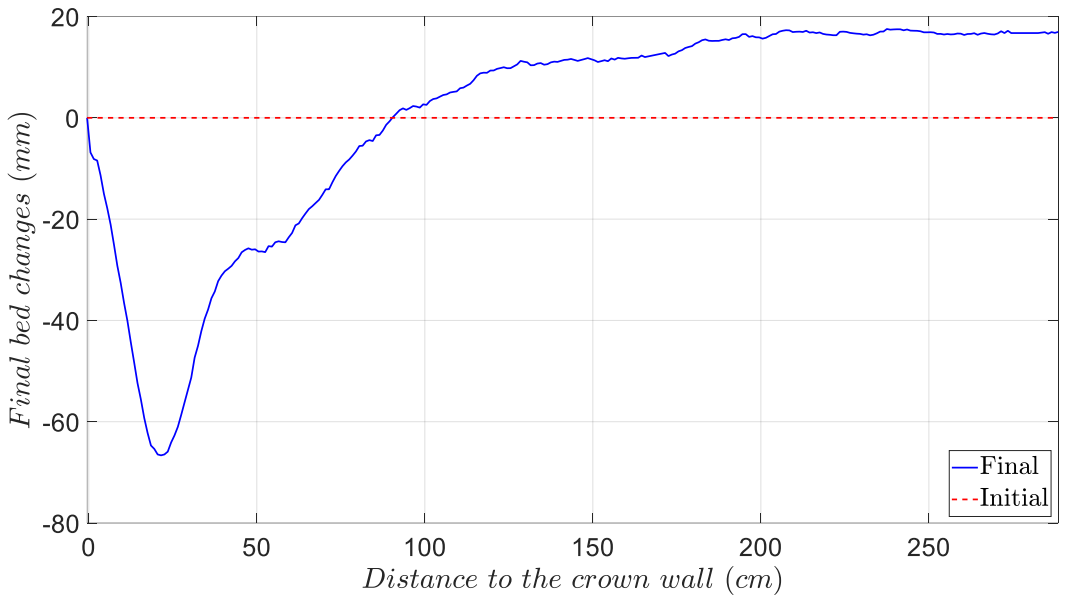

Figure 0.47. Final morphological changes for S-Test-24

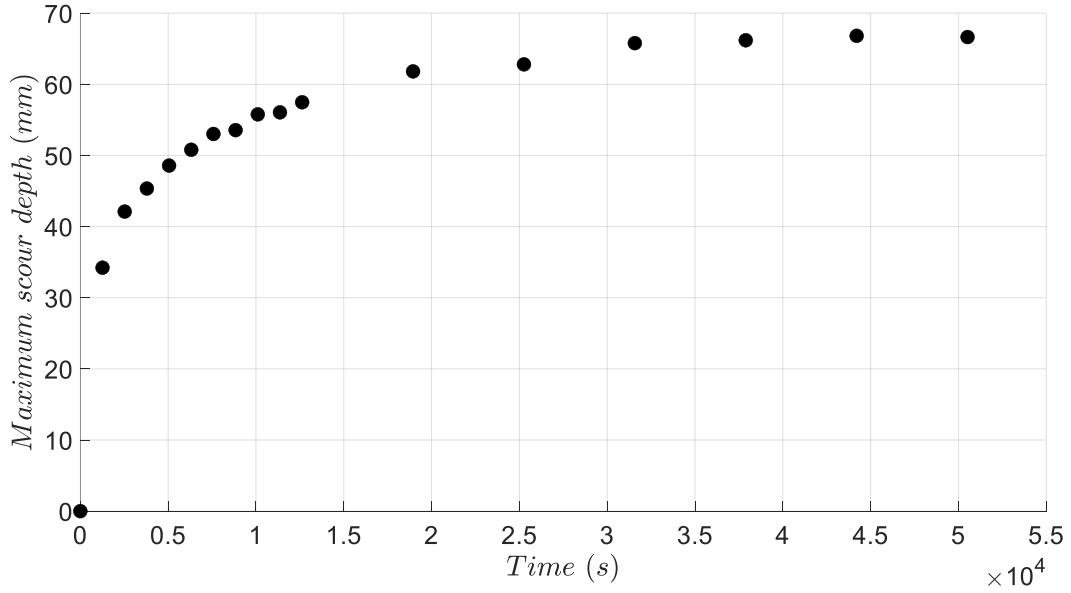

Figure 0.48. Scour development in time for S-Test-24

C. Scour Formations and Development Curves for Tests with $d_{50} = 3.35$ mm

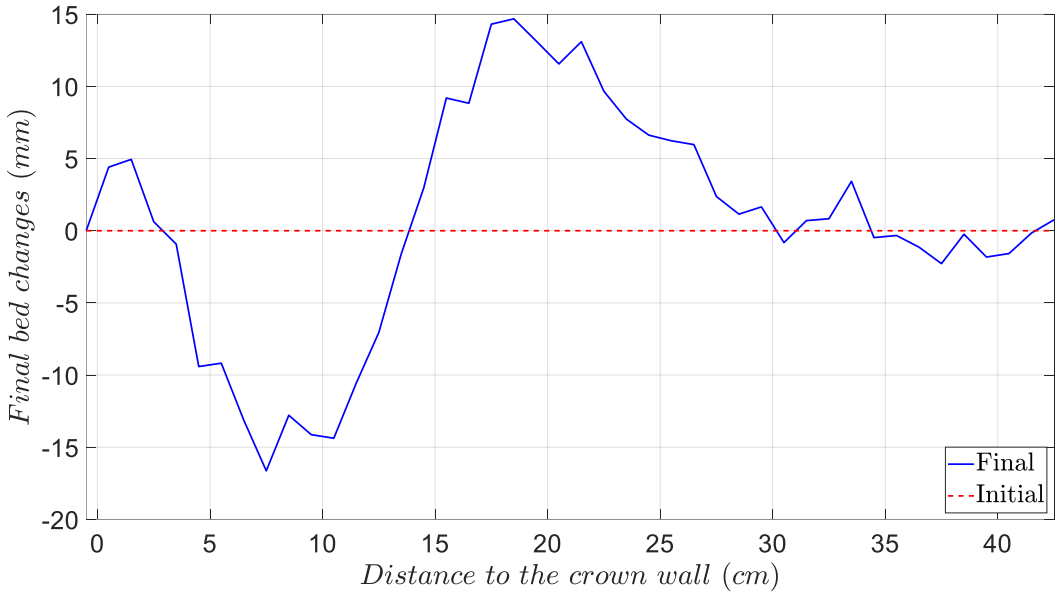

Figure 0.49. Final morphological changes for S-Test-25

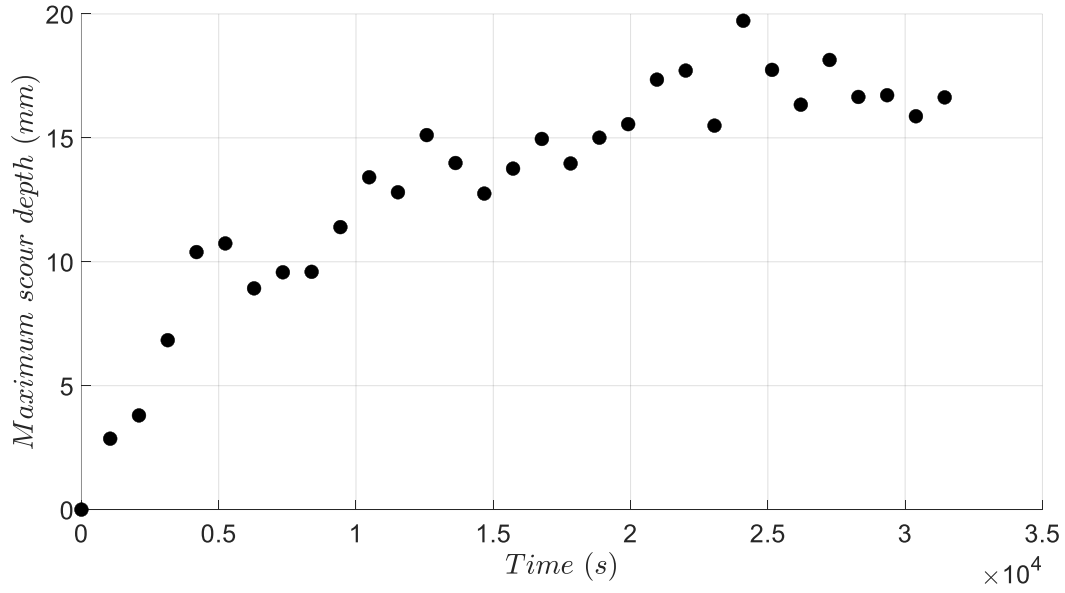

Figure 0.50. Scour development in time for S-Test-25

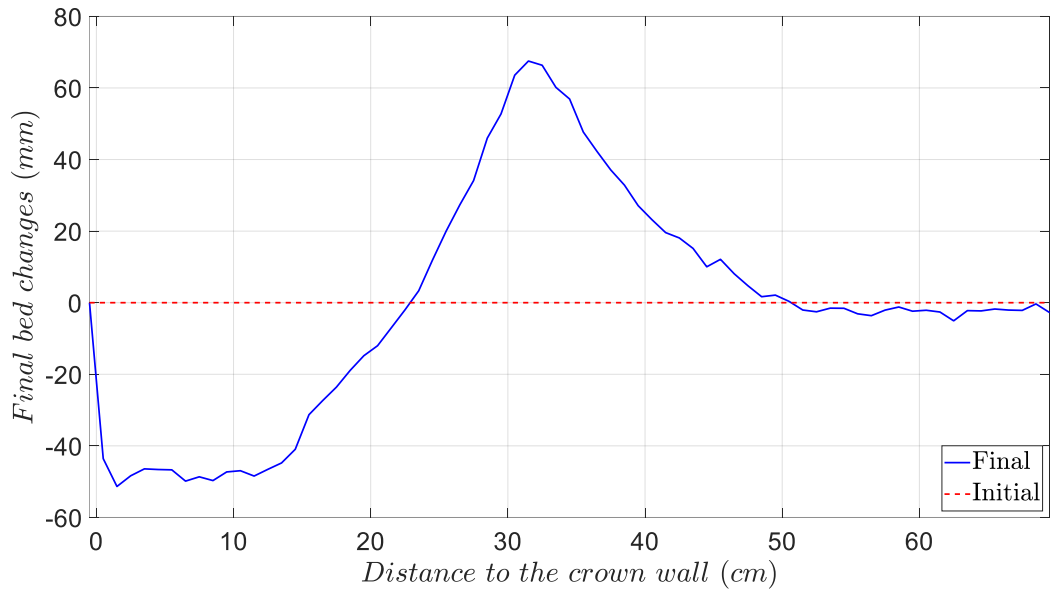

Figure 0.51. Final morphological changes for S-Test-26

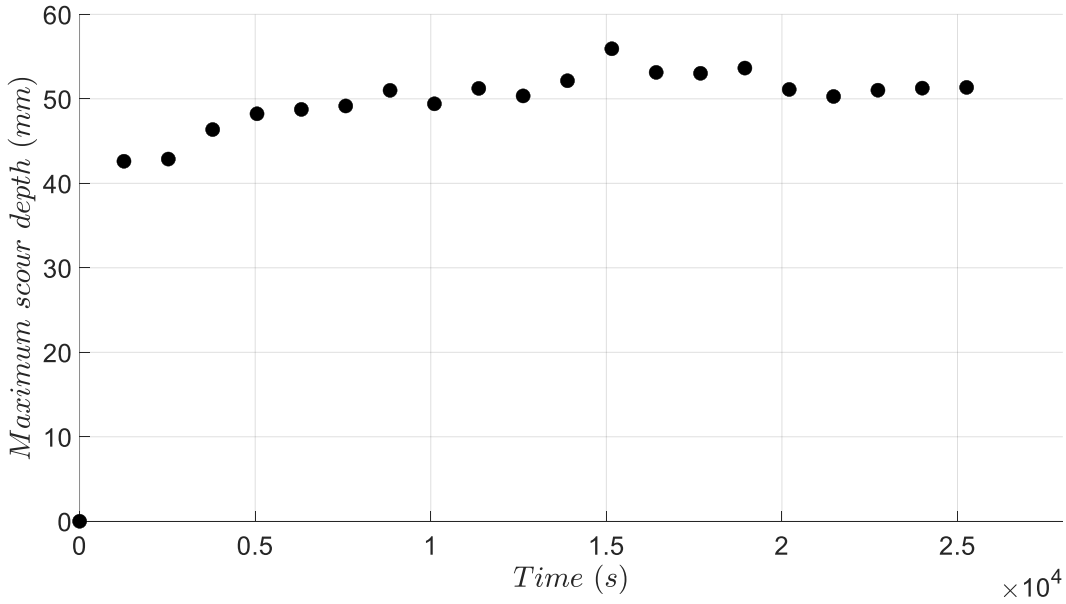

Figure 0.52. Scour development in time for S-Test-26

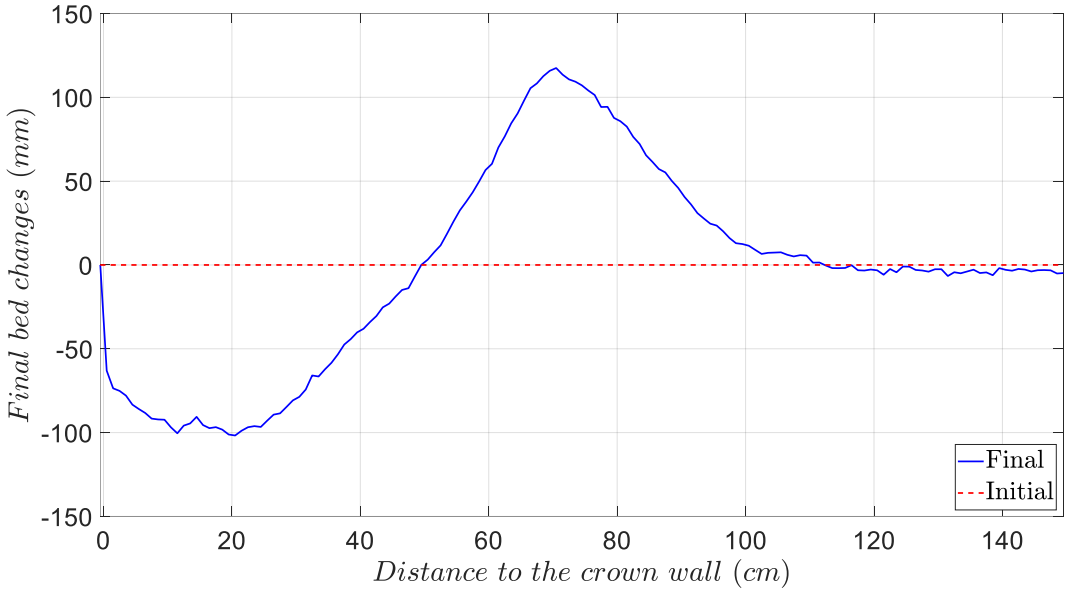

Figure 0.53. Final morphological changes for S-Test-27

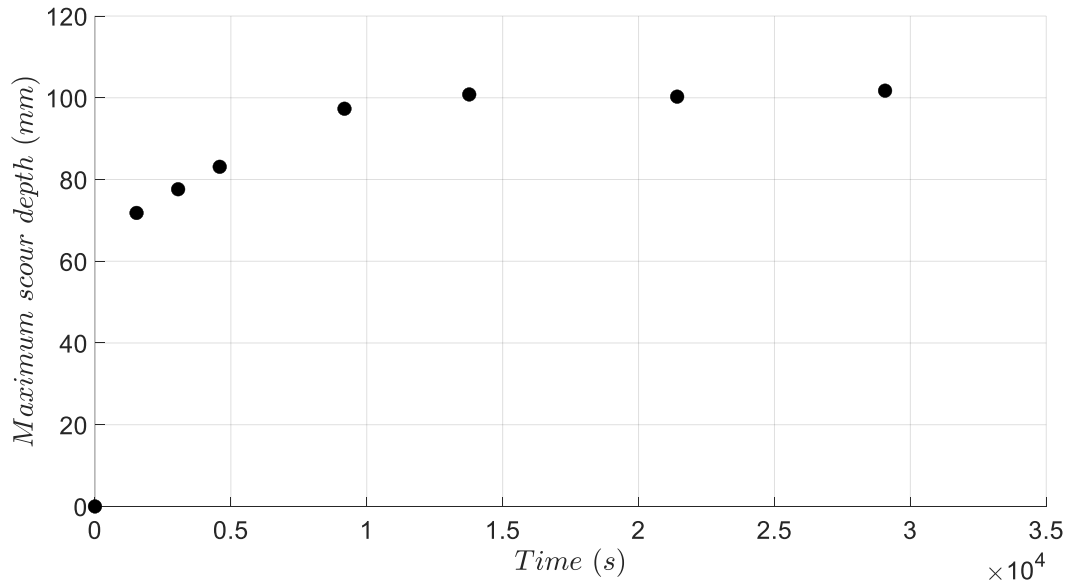

Figure 0.54. Scour development in time for S-Test-27

D. Regular Measurements and Scour Formations for S-Test-6

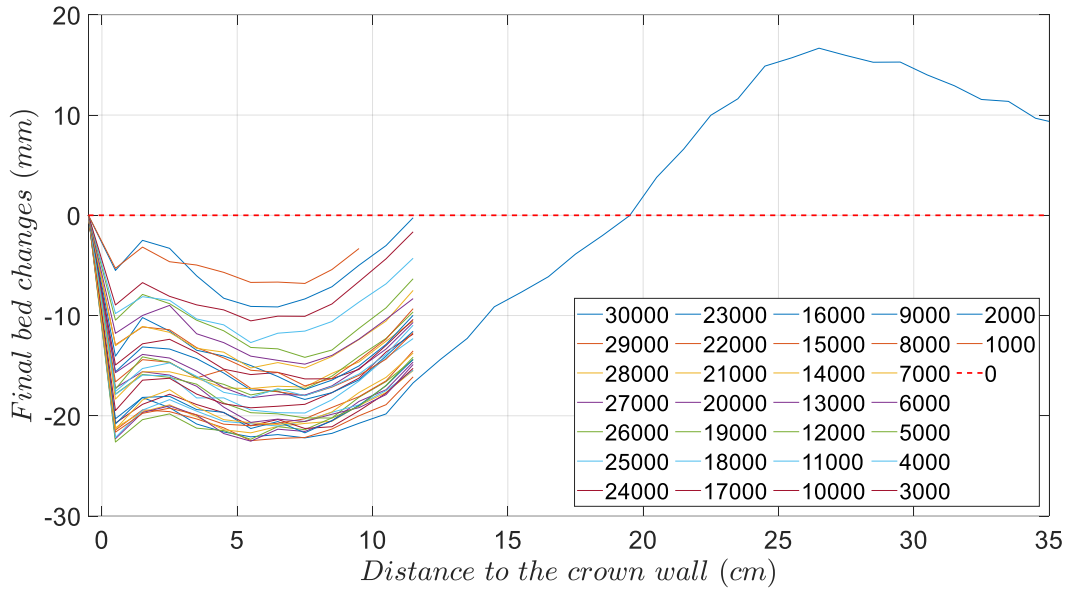

Figure 0.55. Regular measurements for S-Test-27

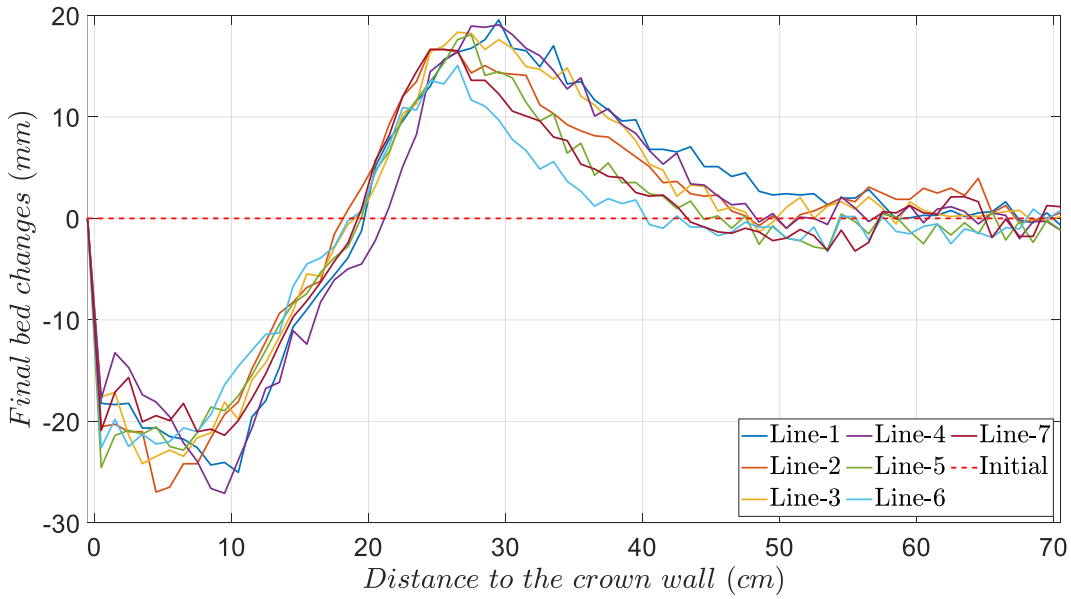

Figure 0.56. Final morphological changes with seven individual lines for S-Test-27